JOURNAL OF PETROLOGY | VOLUME 46 | NUMBER 1 | PAGES 33–78 | 2005 | doi:10.1093/petrology/egh061

Potassic Magmatism in Western Sichuan and Yunnan Provinces, SE Tibet, China: Petrological and Geochemical Constraints on Petrogenesis

ZHENGFU GUO[1,2]*, JAN HERTOGEN[3], JIAQI LIU[1], PAUL PASTEELS[4], ARIEL BOVEN[4], LEA PUNZALAN[4], HUAIYU HE[1,4], XIANGJUN LUO[1,4] AND WENHUA ZHANG[1,4]

[1]INSTITUTE OF GEOLOGY AND GEOPHYSICS, CHINESE ACADEMY OF SCIENCES, PO BOX 9825, BEIJING 100029, CHINA

[2]SCHOOL OF EARTH SCIENCES, LEEDS UNIVERSITY, LEEDS LS2 9JT, UK

[3]AFDELING FYSICO-CHEMISCHE GEOLOGIE, KATHOLIEKE UNIVERSITEIT LEUVEN, CELESTIJNENLAAN 200C, B-3001 LEUVEN, BELGIUM

[4]LABORATORY OF GEOCHRONOLOGY, VRIJE UNIVERSITEIT BRUSSELS, B-1050 BRUSSELS, BELGIUM

RECEIVED NOVEMBER 7, 2003; ACCEPTED JULY 21, 2004
ADVANCE ACCESS PUBLICATION OCTOBER 1, 2004

Potassic volcanism in the western Sichuan and Yunnan Provinces, SE Tibet, forms part of an extensive magmatic province in the eastern Indo-Asian collision zone during the Paleogene (40–24 Ma). The dominant rock types are phlogopite-, clinopyroxene- and olivine-phyric calc-alkaline (shoshonitic) lamprophyres. They are relatively depleted in Na_2O, Fe_2O_3, and Al_2O_3 compared with the late Permian–early Triassic Emeishan continental flood basalts in the western part of the Yangtze craton, and have very high and variable abundances of incompatible trace elements. Primitive mantle-normalized incompatible element patterns have marked negative Nb, Ta and Ti anomalies similar to those of K-rich subduction-related magmas, although the geodynamic setting is clearly post-collisional. Spatially, some incompatible trace element abundances, together with inferred depths of melt segregation based on the Mg-15 normalized compositions of the samples, display progressive zonation trends from SW to NE with increasing distance from the western boundary of the Yangtze craton. Systematic variations in major and trace element abundances and Sr–Nd–Pb isotope compositions appear to have petrogenetic significance. The systematic increases in incompatible trace element abundances from the western margin to the interior of the Yangtze craton can be explained by progressively decreasing extents of partial melting, whereas steady changes in some incompatible trace element ratios can be attributed to changes in the amount of subduction-derived fluid added to the lithospheric mantle of the Yangtze craton. The mantle source region of the lamprophyres is considered to be a relatively refractory phlogopite-bearing spinel peridotite, heterogeneously enriched by fluids derived from earlier phases of late Proterozoic and Palaeozoic subduction beneath the western part of the Yangtze craton. Calculations based on a non-modal batch melting model show that the degree of partial melting ranges from 0·6% to 15% and the proportion of subduction-derived fluid added from ~0·1% to ~0·7% (higher-Ba fluid) or from 5% to 25% (lower-Ba fluid) from the interior to the western margin of the Yangtze craton. Some pre-existing lithospheric faults might have been reactivated in the area neighbouring the Ailao Shan–Red River (ASRR) strike-slip belt, accompanying collision-induced extrusion of the Indo-China block and left-lateral strike-slip along the ASRR shear zone. This, in turn, could have triggered decompression melting of the previously enriched mantle lithosphere, resulting in calc-alkaline lamprophyric magmatism in the western part of the Yangtze craton.

KEY WORDS: *Tibet; potassic magmatism; lithospheric mantle; metasomatism*

INTRODUCTION

Cenozoic igneous activity in the western Sichuan and Yunnan Provinces (WSYP) of SE Tibet, SW China, forms a part of a semi-continuous potassium-rich

*Corresponding author. Present address (until December 2004): School of Earth Sciences, Leeds University, Leeds LS2 9JT, UK. Telephone: +44 113 343 5234. Fax: +44 113 343 5259.
E-mail: Zhengfu@earth.leeds.ac.uk

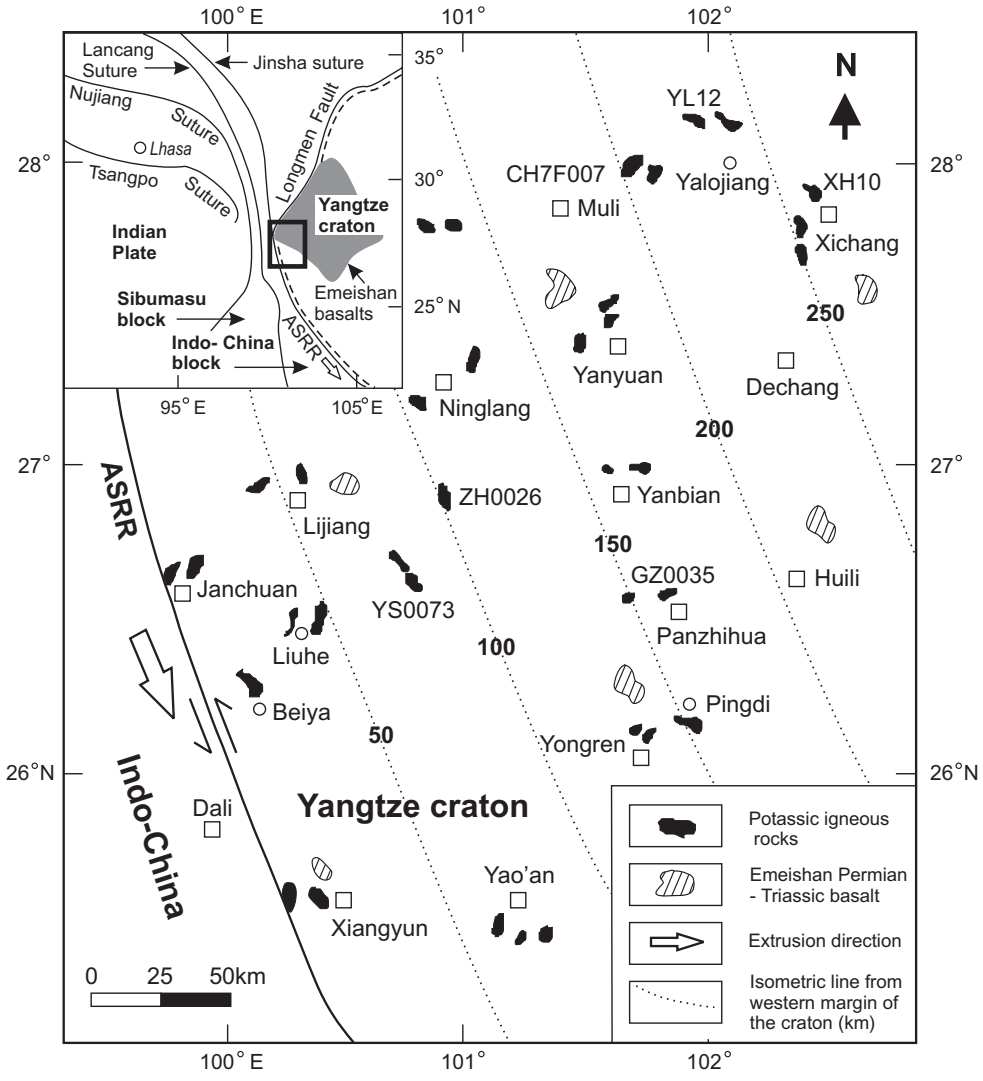

Fig. 1. Simplified map of the distribution of Cenozoic potassic igneous rocks in the western margin of the Yangtze craton (modified from YBGMR, 1990; SBGMR, 1991; Xu *et al.*, 2001*b*). The traverse is a broad zone about 300 km wide rather than a narrow linear traverse, extending from the Janchuan volcanic field in the SW of the traverse, through the Lijiang, Ninglang, Yanyuan, Muli and Yalojiang volcanic fields, to the Xichang field at the NE end. In addition, we also studied the volcanic fields located to the south of the traverse, including Liuhe, Xiangyun, Yao'an, Yongren, Panzhihua, and Yanbian. □, cities; ○, villages. A rectangle drawn with bold continuous lines in the inset shows the position of the study area. The dashed line in the inset represents the northwestern, western and southwestern edges of the Yangtze craton.

magmatic province in the eastern Indo-Asian collision zone (Chung *et al.*, 1998*b*; Liu, 1999; Wang *et al.*, 2001; Fig. 1). Despite many studies, the petrogenesis of the rocks remains controversial and has been variously attributed to the collision of India and Asia (Liu, 1999, 2000), intraplate deformation (Deng *et al.*, 1998*a*, 1998*b*; Zhong *et al.*, 2000), rift magmatism (Zhu *et al.*, 1992; Xie & Zhang, 1995; Xie *et al.*, 1999; Zhang *et al.*, 2000), convective removal of the mantle lithosphere (Chung *et al.*, 1998*b*), and subducted slab break-off (Flower *et al.*, 1998).

The tectonic–magmatic activity in the eastern Indo-Asian collision zone has been divided into two episodes: an earlier phase, localized along the Ailao Shan–Red River (ASRR) shear zone, which marks the western boundary of the Yangtze craton (Fig. 1), is thought to have been generated as a consequence of synchronous continental lithosphere transpression (42–24 Ma); the later phase (16–0 Ma) is thought to be related to east–west extension (Wang *et al.*, 2001). However, the lack of detailed field sampling, and petrological and geochemical data has precluded further constraints on the petrogenesis of the magmas, including their tectonic setting and relationship to the geodynamic evolution of the eastern Indo-Asian collision zone.

This study focuses on a SW–NE-trending, 270 km long, traverse perpendicular to the western margin of the

Yangtze craton (Fig. 1). It extends from the Janchuan volcanic field in the SW of the traverse (closest to the western margin of the Yangtze craton), through the Lijiang, Ninglang, Yanyuan and Muli volcanic fields to the Xichang field at the NE end (Fig. 1). In addition, we also studied some other volcanic fields located to the south of the traverse, including Liuhe, Xiangyun, Yao'an, Yongren, Panzhihua, and Yanbian (Fig. 1). The traverse thus represents a broad zone, about 300 km wide, rather than a narrow linear traverse.

The magmatic rocks are mainly Eocene–Oligocene, small volume, mafic potassic dykes, sills and hypabyssal intrusions. Whole-rock major and trace element and Sr–Nd–Pb isotope data are used to define compositional changes along the SW–NE traverse and adjacent areas (Fig. 1). These data are complementary to previous studies that predominantly focused on either the petrogenesis of individual volcanic fields (Zhu *et al.*, 1992; Huang *et al.*, 1997; Deng *et al.*, 1998*a*, 1998*b*; Xie *et al.*, 1999) or the compositional variations of igneous rocks mainly along the ASRR shear zone (i.e. along the western margin of the Yangtze craton) in the eastern Indo-Asian collision zone (Chung *et al.*, 1998*b*; Zhang & Scharer, 1999; Zhang *et al.*, 2000; Wang *et al.*, 2001). In addition, this study, for the first time, recognizes a compositional zonation of trace element abundances and ratios from the western margin (at the SW end of the traverse) to the interior (at the NE end of the traverse) of the Yangtze craton.

Although there have been many studies of regional compositional changes in subduction-related magmatic rocks, most of these have focused on the geochemical zonation across island arcs (e.g. Dickinson & Hatherton, 1975; Leeman *et al.*, 1990; Ishikawa & Nakamura, 1994; Barragan *et al.*, 1998; Hochstaedter *et al.*, 2000; Walker *et al.*, 2000; Elburg *et al.*, 2002). The nature of the compositional zonation of post-collision potassic magmatic rocks across palaeo-subduction zones is poorly understood, probably because crustal contamination and magma differentiation have obscured these zonation characteristics. The near-primitive nature of the WSYP magmatic rocks makes it possible to reveal the regional compositional zonation of post-collision potassic magmatic rocks in SE Tibet.

GEOLOGICAL SETTING

The studied potassic igneous rocks are located along the western margin of the Yangtze craton (Fig. 1). The basement of the Yangtze craton consists of Archaean high-grade metamorphic rocks and early–middle Proterozoic metasedimentary rocks [Zhai & Yang, 1986; Wu & Cong, 1988; Yunnan Bureau of Geology and Mineral Resources (YBGMR), 1990; Sichuan Bureau of Geology and Mineral Resources (SBGMR), 1991; Gao *et al.*, 1999; Qiu *et al.*, 2000]; the cover sequences comprise Phanerozoic clastics and carbonates. Previous geological studies (YBGMR, 1990) indicate that the WSYP volcanic rocks are located within Proterozoic mobile belts in the western part of the Archaean Yangtze craton in regions that underwent lithospheric accretionary events associated with Proterozoic oceanic subduction beneath the western Yangtze craton. The Kangding granitoid body crops out within the western mobile belts of the Yangtze craton (Cong, 1988; SBGMR, 1991; Xu *et al.*, 1995). This granitoid body extends from Kangding, which is ~260 km north of Xichang (Fig. 1), to Yuanmou, which is ~120 km south of Huili (Fig. 1) (Xu *et al.*, 1995). The Kangding granitoid body is oriented approximately north–south and is associated with contemporaneous intermediate–acidic arc volcanic rocks (He & Chen, 1988; Feng *et al.*, 1990). Two $^{40}Ar/^{39}Ar$ ages of amphibole from the granitoid body are 740 Ma and 763·6 Ma (Wang *et al.*, 1987), whereas 64 zircon U–Pb ages range from 548 Ma to 1095 Ma, most of which are within the range 700–800 Ma (Xu *et al.*, 1995). A recent study showed that the age of the Kangding granitoid is 706 ± 36 Ma on the basis of a Sm–Nd whole-rock isochron of five samples (Chen *et al.*, 2001). The granitoid and volcanics are calc-alkaline (Cong, 1988; Wu & Zhang, 1990; YBGMR, 1990; SBGMR, 1991; Xu *et al.*, 1995) and their presence suggests that there was oceanic subduction beneath the western margin of the Yangtze craton during the late Proterozoic (Xu *et al.*, 1995).

The Palaeo-Tethys ocean basin opened when the Indo-China block and the Yangtze craton rifted and separated from the northern margin of Gondwanaland in the Devonian (Wang *et al.*, 2000). The main branch of Palaeo-Tethys was the Lancang ocean, now indicated by the Lancang suture between the Indo-China block and the Sibumasu block (inset in Fig. 1) (YBGMR, 1990; Mo *et al.*, 1991, 1993; Yang, 1998; Wang *et al.*, 2000). The suture is marked by dismembered Devonian–Carboniferous ophiolitic assemblages (serpentinite, harzburgite, gabbro, diabase and mafic lavas) and Permo-Triassic arc volcanic belts (Mo *et al.*, 1991, 1993; Yang, 1998; Wang *et al.*, 2000). The dismembered ophiolitic sequences are believed to have been emplaced mainly into Carboniferous marine sediments (YBGMR, 1990; Mo *et al.*, 1993; Yang, 1998). The Permo-Triassic arc volcanic rocks are well exposed to the east of the Lancang suture zone (Yang, 1998); these include tholeiitic, calc-alkalic and shoshonitic series. There is a geochemical polarity, which displays an increase in potassium and other incompatible trace elements (e.g. Rb and Ba) towards the east within the volcanic belt (Mo *et al.*, 1993; Yang, 1998). This indicates a mature volcanic arc and suggests that the oceanic crust subducted towards the east.

A recent study has demonstrated that the Indo-China block was connected with the western Yangtze

craton forming an integrated continental block during the initial stage of Lancang ocean subduction, and that subduction occurred beneath the present-day western margin of the Yangtze craton (Wang *et al.*, 2000). Following initial sea-floor spreading in the early Devonian, deposition of middle–late Devonian oceanic ribbon-bedded cherts (Liu *et al.*, 1991, 1993) occurred. Subduction of the Lancang oceanic crust beneath the integrated Indo-China block and the western margin of the Yangtze craton in the Middle–Late Devonian to earliest Carboniferous eventually led to back-arc extension and rifting between the Indo-China block and the western Yangtze craton (see Wang *et al.*, 2000, fig. 10). The occurrence of Devonian–Carboniferous graptolite-bearing deep-water clastics along the western margin of the Yangtze craton has been considered to be the result of this back-arc extension and rifting (Wang *et al.*, 2000). This phase of extension is considered to be a precursor of the Jinsha ocean, now represented by the Jinsha suture zone (YBGMR, 1990; Mo *et al.*, 1991, 1993; Yang, 1998; Wang *et al.*, 2000), which lies between the Indo-China block and the Yangtze craton (inset in Fig. 1). The exact age and geodynamic setting of the Jinsha suture zone remain controversial (Mo *et al.*, 1991, 1993; Yang, 1998; Wang *et al.*, 2000, and references therein). It is marked by mélanges containing ultramafic blocks, ophiolitic assemblages, pillow lavas and pelagic sediments (Mo *et al.*, 1991, 1993; Yang, 1998). Plagiogranite is widely found within the mélanges, which is thought to be a typical oceanic granitoid (Wang *et al.*, 2000); the plagiogranites occur in tectonic contact with the ultramafic blocks. Two zircon U–Pb ages of 340 Ma and 362 Ma for the Shusong and Shuanggou plagiogranites suggest that the Jinsha oceanic lithosphere between the Yangtze craton and the Indo-China block was generated in late Devonian to early Carboniferous times. Moreover, early Carboniferous radiolarians and conodonts have been reported from chert and siliceous limestone interbeds within pillow basalts from the mélange (Wu, 1993; Feng *et al.*, 1997). This indicates the presence of Jinsha oceanic sediments of early Carboniferous age in this area.

The collision between the Indo-China block and the Yangtze craton, and between the Indo-China and Sibumasu blocks (inset in Fig. 1), occurred in middle–late Triassic times as a consequence of the closure of the Palaeo-Tethys oceans (i.e. Lancang and Jinsha oceans) between these continental blocks (also see Wang *et al.*, 2000, fig. 10). These continent–continent collisions led to structural deformation, regional metamorphism of varying degrees and disruption of the ophiolitic mélanges. Latest Permian–middle Triassic synorogenic (or syn-collision) granitoids, such as the Xumai (238 Ma) and Zhongmu (255–227 Ma) granitoids, are distributed along the collisional orogenic belt (Wang *et al.*, 2000). Late Triassic molasse unconformably overlies early Palaeozoic metamorphic rocks in the suture zone and marks the cessation of tectonic activity.

The western part of the Yangtze craton has experienced intracontinental deformation since the middle–late Triassic, but no further oceanic plate subduction has occurred beneath the western part of the craton (Yang, 1998; Wang *et al.*, 2000). This strong intracontinental deformation makes it difficult to determine the subduction direction of the Palaeo-Tethys ocean lithosphere merely based on the position of arc volcanics and opholitic belts.

During late Permian to early Triassic times a sequence of flood basalts, the Emeishan basalts, considered to be the consequence of mantle plume activity (Chung & Jahn, 1995; Chung *et al.*, 1998*a*; Xu *et al.*, 2001*a*), were erupted, covering the western part of the Yangtze craton (inset of Fig. 1). Previous studies (e.g. Chung *et al.*, 1998*a*) suggested that the plume centre (or head) was to the east of the study area. The exposed area of this large igneous province is around 250 000 km^2; basaltic rocks distributed in Sichuan and Yunnan Provinces constitute the western part of the Emeishan flood basalts (Chung *et al.*, 1998*a*; Xu *et al.*, 2001*a*).

The 55–50 Ma collision of India and Asia in south Tibet (inset of Fig. 1) led to the formation of the ASRR shear zone in SE Tibet, reactivating the Devonian–Carboniferous suture separating the Yangtze craton and the Indo-China block, which was driven to the SE as a consequence of tectonic escape (Tapponnier *et al.*, 1990; Scharer *et al.*, 1994; Leloup *et al.*, 1995; Zhang & Zhong, 1996; Zhang & Scharer, 1999; Fig. 1). More than 300 km of Tertiary left-lateral strike-slip movement has occurred along the ASRR shear zone (Tapponnier *et al.*, 1990; Scharer *et al.*, 1994; Leloup *et al.*, 1995). This tectonic activity has intensely modified the ophiolitic sequences and the geometry of this suture and overwhelmed (even erased) many of the signatures of the earlier volcanic arc. Coincident with movement along the ASRR shear zone and associated fracture systems, a progressive rise of isotherms resulted in greenschist- to amphibolite-facies regional metamorphism and associated magmatic activity in Eocene–Oligocene times in the western part of the Yangtze craton (YBGMR, 1990; Liu, 1999; Qian, 1999). Numerous Paleogene dykes, sills, and small hypabyssal bodies were emplaced within Cenozoic pull-apart basins (YBGMR, 1990; SBGMR, 1991; Liu, 1999; Qian, 1999), predominantly located at the intersection zones of several different directions of faults in the eastern Indo-Asian collision zone. These basins are typically bounded by high-angle normal faults or strike-slip faults (YBGMR, 1990; SBGMR, 1991; Tan, 1999).

This paper presents detailed geochemical and Sr–Nd–Pb isotopic analyses of magmatic rocks collected from these volcanic–sedimentary basins along a 270 km long traverse extending from 99°50′E, 26°35′N to 102°18′E,

Table 1: $^{40}Ar/^{39}Ar$ ages for the WSYP volcanic rocks

Number	Locality	Rock name	Mineral	Plateau age (Ma)	Isochron age (Ma)	$(^{40}Ar/^{36}Ar)^{\circ}$	MSWD
CH7F002	Beiya	minette	phlogopite	34·88 ± 0·11	34·75 ± 0·05	298·03 ± 1·31	4·75
EX08	Yanyuan	minette	sanidine	32·98 ± 0·13	32·76 ± 0·06	298·50 ± 1·53	4·24

$(^{40}Ar/^{36}Ar)^{\circ}$ is the initially trapped $^{40}Ar/^{36}Ar$ ratio.

27°51′N (Fig. 1). Most of the samples are Eocene–Oligocene in age, ranging from 24 to 40 Ma based on 44 K–Ar ages and 21 ^{40}Ar–^{39}Ar ages (YBGMR, 1990; SBGMR, 1991; Zhu *et al.*, 1992; Zhang & Xie, 1997; Chung *et al.*, 1998*b*; Deng *et al.*, 1998*a*; Liu, 1999; Wang *et al.*, 2001). Two new ^{40}Ar–^{39}Ar ages obtained for lamprophyres as part of this study are consistent with this age range (Table 1 and Electronic Appendix; the latter can be downloaded from the *Journal of Petrology* website at http://www.petrology.oupjournals.org).

PETROGRAPHIC CHARACTERISTICS

The igneous rocks studied display many of the typical petrographic characteristics of shoshonitic (calc-alkaline) lamprophyres (Rock, 1984; Rock *et al.*, 1991): (1) porphyritic textures with panidiomorphic phenocrysts and microcrystalline groundmass; (2) presence of castellated phlogopite phenocrysts and the absence of orthopyroxene, quartz and feldspar phenocrysts; (3) presence of globular felsic structures consisting dominantly of feldspars. The studied samples do not contain titanian richterite or groundmass tetraferriphlogopite, or accessory priderite, wadeite and perovskite (Xie & Zhang, 1995; Deng *et al.*, 1998*b*; Lu & Qian, 1999; Qian, 1999), indicating that they are not typical lamproites (Mitchell & Bergman, 1991; Sheppard & Taylor, 1992), and have variable mineralogical and textural characteristics. The more mafic rocks have more olivine (1–4%) and phlogopite (2–5%) phenocrysts, and relatively less clinopyroxene (0–3%) set in a microcrystalline matrix. The more evolved samples have more clinopyroxene (1–5%) phenocrysts and relatively less olivine (0–2%) and phlogopite (1–3%) phenocrysts in an augite and feldspar groundmass (Table 2).

ANALYTICAL TECHNIQUES

All of the analysed samples are petrographically fresh and show no evidence of significant hydrothermal alteration. $^{40}Ar/^{39}Ar$ dating (Table 1) was performed at the Laboratory of Geochronology, Vrije Universiteit Brussels. Argon step-heating analyses were performed on a MAP216 mass spectrometer operating in a static mode. Incremental heating was performed by induction heating (accuracy is ±10°C). Age calculations were made using the average of J-factors obtained from repeat measurements of the LP-6 biotite standard, with a reference age of 128·1 ± 0·2 Ma (relative to 162·9 Ma for SB-3 biotite; Baksi *et al.*, 1996). Errors were multiplied by the square root of the MSWD. The detailed procedures follow the description of Boven *et al.* (2002).

Samples 2–3 kg in weight were cut into thin slices. Several fresh slices were cleaned three times using deionized water, dried, and then crushed and powered in an agate mill for major and trace element analyses. For samples CH9716, CH9722, CH9723, CH7F002, CH7F007, CH9783, CH9786, CH9803 and CH9854 (Table 3), the major element and trace element concentrations were analysed at the Department of Afdeling Fysico-chemische Geologie, Katholieke Universiteit Leuven (KUL). Major elements (Si, Ti, Al, Fe, Mg, Ca and P) were determined by atomic absorption spectrometry (AAS), whereas Na, K and Mn were analysed by atomic emission spectrometry (AES). The analytical precisions of both AAS and AES were ≤2%. Loss on ignition (LOI) was determined after ignition at 1000°C for 10 h on 2 g samples. The trace elements Rb, Sr, Nb, Y, Pb, and Zr were analysed on pressed-powder discs by X-ray fluorescence (XRF) spectroscopy using a Kevex 0700. Other trace element concentrations [Sc, Cr, Co, Ba, rare earth elements (REE), Hf, Ta, Th and U] were determined by instrumental neutron activation analysis (INAA). The analytical precisions of the XRF and INAA data are ≤5%. The analytical procedures follow those of Hertogen *et al.* (1985) and Mulder *et al.* (1986). For the remaining samples (SH14, SH15, EX08, EX06, GZ0049, YD0089, YN0015, WH79, WH76, YS0073, NL0031, WH91, XH10, YL12, GZ0014, GZ0024, GZ0064, GZ0029, GZ0035, GZ0046, ZH0026, HD92, JH22, JH21, LH14 and LH15), the major element and trace element compositions were analysed at the Institute of Geology and Geophysics (IGG), Chinese Academy of Sciences, Beijing. Whole-rock major element oxides were analysed with a Phillips PW1400 sequential X-ray fluorescence spectrometer. Fused glass discs were used

Table 2: Tertiary volcanic rocks from WSYP: sample description

Sample no.	Volcanic field	Rock type	Mg-no.	Phenocrysts*	Groundmass
SH14	Yanyuan	Tephrite	0·76	Ol (3) + Phlog (2) + Cpx (1)	Cpx + Phlog + Ol + Ti–Fe
CH9723	Yanyuan	Basalt	0·78	Ol (2) + Phlog (2) + Cpx (2)	Ol + Phlog + Ti–Fe + Ap
CH9722	Yanyaun	Trachybasalt	0·70	Cpx (2) + Phlog (2)	Phlog + San + Cpx + Ti–Fe
SH15	Yanyuan	Basaltic trachyandesite	0·70	Cpx (2) + Ol (1)	Phlog + San + Cpx + Opx
CH7F007	Muli	Trachyandesite	0·74	Phlog (3) + Ol (1) + Cpx (1)	Phlog + San + Cpx + Ol
EX08	Yanyuan	Trachyandesite	0·71	Cpx (2) + Ol (1)	Phlog + San + Cpx + Ti–Fe
CH9716	Yanyuan	Tephrite	0·74	Ol (4) + Phlog (2)	Ol + Phlog + Cpx + Pl + Ti–Fe
XH10	Xichang	Trachybasalt	0·73	Phlog (2) + Ol (1) + Cpx (3)	Phlog + Cpx
EX06	Yanyuan	Basaltic trachyandesite	0·71	Cpx (3) + Phlog (1)	Phlog + San + Cpx + Ol
YL12	Xichang	Basaltic trachyandesite	0·71	Cpx (5) + Phlog (1)	San + Cpx + Ti–Fe + Ap
GZ0014	Panzhihua	Trachybasalt	0·73	Phlog (2) + Ol (2) + Cpx (1)	Phlog + Cpx + Opx + Pl
GZ0024	Pingdi	Basaltic trachyandesite	0·70	Phlog (2) + Cpx (4)	San + Cpx + Ti–Fe + Phlog
GZ0064	Yanbian	Basaltic andesite	0·72	Ol (1) + Phlog (2) + Cpx (2)	Phlog + Cpx + Ap
GZ0029	Yanbian	Basalt	0·75	Ol (2) + Phlog (2)	Ol + Phlog + Cpx + Ap
GZ0035	Panzhihua	Basaltic trachyandesite	0·73	Cpx (1) + Ol (3)	Phlog + Ol + Ti–Fe
GZ0049	Muli	Basalt	0·75	Phlog (4) + Ol (2)	Phlog + Ol + Cpx + Ti–Fe
YD0089	Yao'an	Trachybasalt	0·75	Ol (2) + Phlog (3) + Cpx (1)	Phlog + Ol + Cpx + Pl
GZ0046	Yongren	Basaltic andesite	0·70	Cpx (2) + Phlog (2)	Cpx + Ol + San + Ti–Fe + Ap
YN0015	Ninglang	Trachybasalt	0·73	Cpx (1) + Phlog (3)	Phlog + Cpx + Opx + San + Ap
WH79	Yao'an	Basalt	0·73	Cpx (3) + Phlog (2)	San + Cpx + Pholg + Ap
WH76	Yao'an	Trachyandesite	0·69	Cpx (2) + Phlog (2)	Cpx + Phlog + Ol + Ti–Fe
YS0073	Lijiang	Basaltic trachyandesite	0·74	Phlog (4) + Ol (1)	Ol + Cpx + Phlog
NL0031	Ninglang	Basaltic trachyandesite	0·74	Cpx (3) + Phlog (2)	Ol + Phlog + Ti–Fe + San
ZH0026	Ninglang	Basaltic andesite	0·72	Cpx (2) + Phlog (3)	Ol + Ti–Fe + Cpx + San
CH7F002	Beiya	Basalt	0·70	Ol (2) + Phlog (3) + Cpx (1)	Cpx + Opx + San + Phlog
HD92	Xiangyun	Trachybasalt	0·73	Phlog (5)	Ol + Cpx + Phlog
WH91	Yao'an	Trachybasalt	0·72	Cpx (3) + Phlog (2)	San + Cpx + Ti–Fe
CH9786	Xiangyun	Basaltic trachyandesite	0·68	Cpx (2) + Phlog (2)	Pholg + Cpx + Ol + Opx
CH9854	Xiangyun	Basaltic trachyandesite	0·71	Cpx (5) + Phlog (1)	San + Cpx + Ti–Fe + Ap
CH9783	Xiangyun	Trachyandesite	0·66	Cpx (2) + Ol (1)	Cpx + Pl + Phlog + Ap
CH9803	Xiangyun	Trachyandesite	0·69	Cpx (3) + Ol (1)	Cpx + Phlog + San + pl
JH21	Janchuan	Basaltic andesite	0·71	Cpx (2) + Phlog (1)	Cpx + Phlog + Opx + Pl + Ap
LH14	Lijiang	Trachybasalt	0·73	Cpx (2) + Phlog (2)	Cpx + Phlog + Ti–Fe
LH15	Liuhe	Basaltic trachyandesite	0·72	Ol (2) + Phlog (1)	Pholg + Cpx + Ti–Fe
JH22	Janchuan	Basaltic trachyandesite	0·70	Cpx (1) + Phlog (2)	Pl + Cpx + Phlog + Ap

Ap, apatite; Cpx, clinopyroxene; Ol, olivine; Opx, orthopyroxene; Phlog, phlogopite; Pl, plagioclase; San, sanidine; Ti–Fe, Ti–Fe oxides. Mg-number = $Mg/(Mg + Fe^{2+})$.
*Proportions in percent of phenocrysts shown in parentheses (volume %).

and the analytical precision was better than 2% relative. The analytical procedures in detail follow those of Zhang *et al.* (2002).

For trace element analyses, whole-rock powders (100 mg) were weighed and then dissolved in distilled $HF–HNO_3$ in 15 ml Savillex Teflon screw-cap capsules at 100°C for 2 days, dried and then digested with 6 M HCl at 150°C for 4 days. Powders were spiked with Rh, In and Bi before dilution to 3% HNO_3. Dissolved samples were diluted to 100 ml before analysis. The trace element contents of the sample solutions were analysed by inductively coupled plasma mass spectrometry (ICP-MS). A blank solution was prepared and the total procedural blanks were <50 ng for all the trace elements reported in Table 3. Three replicates and two international standards (BEN, BHVO-1) were prepared using the same procedure to monitor the analytical reproducibility. The discrepancy, based on repeated analyses of

Table 3: Major and trace element analyses of the WSYP rocks

Sample no.:	SH14	CH9723	CH9722	SH15	CH7F007	EX08	CH9716	XH10	EX06	YL12	GZ0014	GZ0024
Locality:	Shuicaoba	Xanping	Xanping	Shuicaoba	Kubadian	Xanping	Shuicaoba	Xichang	Xanping	Yalojiang	Panzhihua	Pingdi
Field:	Yanyuan	Yanyuan	Yanyaun	Yanyuan	Muli	Yanyuan	Yanyuan	Xichang	Yanyuan	Xichang	Panzhihua	Pingdi
Latitude:	27°28·90′	27°37·04′	27°37·04′	27°28·9′	27°57·94′	27°37·04′	27°28·90′	27°51·31′	27°37·04′	28°16·22′	26°34·05′	26°12·91′
Longitude:	101°20·06′	101°22·09′	101°22·09′	101°20·06′	101°40·51′	101°22·09′	101°20·06′	102°18·32′	101°22·09′	101°45·99′	101°39·73′	101°53·08′
D (km):	180	194	188	180	215	185	180	268	192	243	153	148
SiO_2	43·73	45·72	49·80	53·67	59·39	56·68	42·69	47·43	55·23	50·59	48·65	54·07
TiO_2	1·63	2·15	1·51	1·08	1·58	1·10	1·47	1·82	1·40	1·70	1·16	1·53
Al_2O_3	9·64	9·50	12·85	13·21	10·57	12·48	9·88	11·02	12·15	11·85	12·12	12·92
$Fe_2O_3^*$	10·53	9·34	8·84	7·46	5·85	7·25	11·36	9·44	7·84	8·49	9·68	8·53
MnO	0·13	0·17	0·11	0·14	0·12	0·10	0·18	0·13	0·06	0·10	0·12	0·09
MgO	14·45	14·21	9·03	7·46	7·20	7·73	14·12	10·74	8·11	9·03	11·28	8·40
CaO	13·74	13·10	11·62	9·64	5·72	7·16	14·94	12·03	7·97	10·83	10·66	8·30
Na_2O	1·30	0·90	1·44	2·52	1·78	1·29	1·45	1·83	2·09	2·28	1·48	1·50
K_2O	3·58	3·76	3·56	3·57	6·92	5·05	2·68	4·28	4·01	4·11	3·64	3·88
P_2O_5	1·27	1·15	1·24	1·25	0·87	1·16	1·23	1·28	1·14	1·02	1·21	0·78
LOI	1·25	3·46	2·53	1·08	1·73	1·84	2·58	1·74	1·02	2·24	1·06	1·29
Mg-no.	0·76	0·78	0·70	0·70	0·74	0·71	0·74	0·73	0·71	0·71	0·73	0·70
Rb	234	244	206	247	288	247	187	240	224	237	178	219
Ba	5132	6143	4645	4824	6213	6031	4482	6590	5612	6390	3928	4254
Sr	3082	3283	2701	2380	1909	3070	3074	3501	2865	3348	1807	2019
Y	66·8	75·6	83·1	64·3	37·6	42·0	48·0	68·9	56·8	65·9	43·6	44·0
Zr	537	905	426	517	1558	514	464	789	643	732	378	407
Nb	29·3	39·8	18·7	20·7	36·7	19·8	24·2	30·9	21·6	23·9	15·9	18·0
Pb	42·8	39·2	41·2	68·5	90·7	64·6	45·4	95·1	66·3	84·9	41·1	49·6
Th	29·7	26·7	25·5	28·3	30·4	30·6	32·4	34·7	29·4	31·9	16·1	21·1
Ni	496	524	319	239	119	183	585	248	90	221	438	237
Sc	22·4	19·7	16·9	15·6	15·2	14·8	24·1	17·4	15·0	16·0	16·9	14·6
V	314	329	167	128	85	125	337	171	117	164	255	130
Cr	680	593	379	388	277	277	708	399	278	379	509	392
Co	48·3	46·5	37·0	25·4	26·5	29·5	50·5	37·0	26·2	36·3	36·8	31·1
La	190·4	189·9	148·6	158·5	160·7	192·9	191·8	256·7	178·2	220·7	113·9	120·9
Ce	411·4	421·4	307·7	324·0	330·6	385·2	405·4	537·1	368·2	478·9	208·6	238·0

Table 3: continued

Sample no.:	SH14	CH9723	CH9722	SH15	CH7F007	EX08	CH9716	XH10	EX06	YL12	GZ0014	GZ0024
Locality:	Shuicaoba	Xanping	Xanping	Shuicaoba	Kubadian	Xanping	Shuicaoba	Xichang	Xanping	Yalojiang	Panzhihua	Pingdi
Field:	Yanyuan	Yanyuan	Yanyaun	Yanyuan	Muli	Yanyuan	Yanyuan	Xichang	Yanyuan	Xichang	Panzhihua	Pingdi
Latitude:	27°28·90′	27°37·04′	27°37·04′	27°28·9′	27°57·94′	27°37·04′	27°28·90′	27°51·31′	27°37·04′	28°16·22′	26°34·05′	26°12·91′
Longitude:	101°20·06′	101°22·09′	101°22·09′	101°20·06′	101°40·51′	101°22·09′	101°20·06′	102°18·32′	101°22·09′	101°45·99′	101°39·73′	101°53·08′
D (km):	180	194	188	180	215	185	180	268	192	243	153	148
Nd	190·1	206·5	131·3	134·4	136·9	158·8	175·1	234·8	158·4	213·9	83·2	96·2
Sm	33·6	38·5	21·2	21·9	22·2	25·2	29·1	36·2	26·4	33·6	14·2	17·3
Eu	8·69	10·15	5·24	5·61	5·87	6·42	7·37	9·88	6·89	8·90	3·60	4·39
Tb	2·94	3·68	1·65	1·66	1·68	2·02	2·65	2·95	1·96	2·53	1·25	1·54
Yb	3·10	3·11	1·94	2·01	2·15	2·36	3·26	2·48	1·92	2·24	1·79	1·86
Lu	0·42	0·41	0·27	0·26	0·25	0·29	0·44	0·31	0·25	0·30	0·21	0·20
Hf	18·6	22·1	10·2	10·9	35·6	11·7	10·8	18·9	11·4	17·2	8·05	9·54
Ta	1·33	1·95	1·22	1·21	2·01	1·21	1·13	1·68	1·20	1·43	0·89	0·91
U	5·61	5·68	4·21	5·39	8·79	5·59	6·72	9·78	5·22	9·24	3·46	3·93

Sample no.:	GZ0064	GZ0029	GZ0035	GZ0049	YD0089	GZ0046	YN0015	WH79	WH76	YS0073	NL0031	ZH0026
Locality:	Yanbian	Yanbian	Panzhihua	Lugu lake	Laogaizi	Yongren	Ninglang	Wenhua	Wenhua	Yongsheng	Ninglang	Zhanhe
Field:	Yanbian	Yanbian	Panzhihua	Muli	Yao'an	Yongren	Ninglang	Yao'an	Yao'an	Lijiang	Ninglang	Ninglang
Latitude:	27°1·28′	27°1·37′	26°34·06′	27°49′	25°24·42′	26°08·31′	27°13·06′	25°23·12′	25°23·12′	26°40·32′	27°13·94′	26°51·52′
Longitude:	101°33·04′	101°33·04′	101°39·72′	100°46·54′	101°17·12′	101°36·41′	100°52·14′	101°15·16′	101°15·16′	100°42·42′	100°52·09′	100°56′
D (km):	164	168	157	126	70	133	108	65	62	73	106	98
SiO_2	54·96	50·54	52·82	46·95	46·18	53·94	47·58	50·87	55·89	52·94	51·34	55·15
TiO_2	1·50	0·78	0·95	0·96	0·87	1·30	0·94	1·09	0·94	0·84	1·04	1·03
Al_2O_3	11·94	11·25	12·60	9·80	11·78	12·92	12·04	12·31	12·08	12·14	11·28	12·96
$Fe_2O_3^*$	8·38	9·30	8·45	10·44	9·87	8·78	10·40	8·95	8·04	8·53	8·68	7·95
MnO	0·08	0·11	0·08	0·14	0·12	0·09	0·14	0·12	0·13	0·05	0·12	0·08
MgO	9·08	11·68	9·58	13·50	12·83	8·63	11·84	10·56	7·64	10·23	10·34	8·67
CaO	8·27	11·13	9·10	12·97	12·09	8·85	10·77	11·34	7·59	9·35	10·89	8·62
Na_2O	1·48	1·08	1·91	1·58	1·83	1·13	2·18	1·08	2·16	1·33	1·90	1·32
K_2O	3·50	2·94	3·68	2·50	3·40	3·60	3·36	2·79	4·90	3·81	3·64	3·47

Sample no.:	GZ0064	GZ0029	GZ0035	GZ0049	YD0089	GZ0046	YN0015	WH79	WH76	YS0073	NL0031	ZH0026
Locality:	Yanbian	Yanbian	Panzhihua	Lugu lake	Laogaizi	Yongren	Ninglang	Wenhua	Wenhua	Yongsheng	Ninglang	Zhanhe
Field:	Yanbian	Yanbian	Panzhihua	Muli	Yao'an	Yongren	Ninglang	Yao'an	Yao'an	Lijiang	Ninglang	Ninglang
Latitude:	27°1·28′	27°1·37′	26°34·06′	27°49′	25°24·42′	26°08·31′	27°13·06′	25°23·12′	25°23·12′	26°40·32′	27°13·94′	26°51·52′
Longitude:	101°33·04′	101°33·04′	101°39·72′	100°46·54′	101°17·12′	101°36·41′	100°52·14′	101°15·16′	101°15·16′	100°42·42′	100°52·09′	100°56′
D (km):	164	168	157	126	70	133	108	65	62	73	106	98
P_2O_5	0·81	1·19	0·83	1·16	1·03	0·76	0·75	0·89	0·63	0·78	0·77	0·75
LOI	0·82	1·32	2·02	0·73	0·84	1·92	0·69	1·32	0·85	0·72	0·56	1·88
Mg-no.	0·72	0·75	0·73	0·75	0·75	0·70	0·73	0·73	0·69	0·74	0·74	0·72
Rb	183	169	191	146	128	180	153	123	159	148	159	160
Ba	3904	3810	4209	3581	2579	3989	2731	2448	2896	2599	2884	2547
Sr	1985	1758	1859	1609	1421	1898	1498	1788	1591	1689	1597	1633
Y	43·6	38·5	40·0	44·1	28·1	38·2	21·9	26·4	33·2	25·0	26·3	30·7
Zr	400	364	381	356	236	414	257	276	196	236	254	245
Nb	17·0	14·0	15·0	15·1	10·0	11·2	11·2	12·5	8·1	10·6	11·0	11·0
Pb	49·8	42·4	44·2	40·5	36·2	42·0	35·3	36·2	34·2	36·0	35·1	36·3
Th	20·2	19·1	21·2	16·1	10·7	19·6	11·6	12·8	13·3	13·1	11·9	13·3
Ni	269	378	260	499	469	269	322	251	106	209	226	198
Sc	15·1	17·3	14·6	22·8	26·9	15·1	18·8	16·1	17·6	18·1	20·8	15·4
V	126	270	160	360	289	115	250	171	105	176	177	120
Cr	369	475	376	859	530	368	387	371	298	389	389	401
Co	30·3	46·0	25·2	48·3	40·6	26·0	31·1	27·6	22·5	30·8	30·4	32·9
La	118·3	105·3	117·6	95·5	60·2	128·9	64·9	62·1	64·9	62·0	70·4	72·2
Ce	241·0	199·3	210·3	184·8	129·2	253·5	120·8	126·3	138·1	129·2	130·6	133·5
Nd	102·1	87·0	90·8	80·2	48·9	100·3	56·2	60·2	65·2	61·0	57·9	60·2
Sm	16·9	15·3	14·9	13·8	9·8	18·1	10·6	11·1	11·1	10·6	11·1	10·2
Eu	4·61	4·29	4·10	3·69	2·59	4·73	2·80	2·82	2·85	2·81	2·79	2·74
Tb	1·68	1·51	1·46	1·39	1·00	1·50	0·99	1·10	1·11	1·11	1·09	1·09
Yb	1·90	1·98	2·06	1·82	1·71	1·95	1·85	1·70	1·69	1·69	1·80	1·65
Lu	0·19	0·23	0·23	0·20	0·25	0·22	0·24	0·23	0·23	0·23	0·21	0·22
Hf	9·41	7·52	8·52	7·46	3·85	7·33	3·66	6·25	4·66	3·76	6·38	3·65
Ta	0·91	0·82	0·86	0·87	0·56	0·89	0·60	0·79	0·46	0·65	0·62	0·64
U	3·87	3·72	3·79	3·49	2·95	3·90	2·96	3·09	3·90	3·49	3·07	3·47

Table 3: continued

Sample no.:	CH7F002	HD92	WH91	CH9786	CH9854	CH9783	CH9803	JH21	LH14	LH15	JH22
Locality:	Beiya	Haidong	Wenhua	Haidong	Xiangyun	Haidong	Xiangyun	Janchuan	Lijiang	Liuhe	Janchuan
Field:	Beiya	Xiangyun	Yao'an	Xiangyun	Xiangyun	Xiangyun	Xiangyun	Janchuan	Lijiang	Liuhe	Janchuan
Latitude:	26°10·21′	25°40·95′	25°23·12′	25°40·36′	25°32·01′	25°40·95′	25°32·01′	26°35·14′	26°54·52′	26°25·02′	26°35·07′
Longitude:	100°18′	100°21·41′	101°15·16′	100°20·61′	100°30·98′	100°21·41′	100°30·04′	99°50·18′	100°14·13′	100°20·07′	99°50·08′
D (km):	8	18	68	16	10	18	5	3	35	27	1
SiO_2	46·34	48·67	49·72	52·93	53·65	56·35	56·33	53·68	50·23	51·58	52·27
TiO_2	1·29	0·94	0·88	0·90	0·76	0·90	0·70	0·74	1·01	0·83	0·86
Al_2O_3	13·88	11·94	11·91	13·08	13·22	12·01	12·64	12·54	11·85	12·49	12·75
$Fe_2O_3^*$	11·09	10·05	9·54	7·95	7·79	7·99	7·71	8·64	9·03	8·38	8·97
MnO	0·14	0·06	0·12	0·13	0·12	0·11	0·10	0·12	0·11	0·13	0·08
MgO	11·34	11·47	10·67	7·33	8·16	6·54	7·53	8·91	10·36	9·35	9·03
CaO	10·25	10·95	10·54	10·17	9·81	7·22	6·22	9·68	11·61	11·00	10·27
Na_2O	1·52	1·77	2·30	2·66	2·54	2·09	2·60	1·46	1·17	1·70	1·64
K_2O	2·77	3·65	3·48	4·36	3·55	6·37	4·89	3·67	3·87	3·91	3·68
P_2O_5	1·38	0·50	0·84	0·49	0·40	0·42	1·28	0·56	0·76	0·63	0·45
LOI	2·16	0·75	1·06	2·11	1·04	2·04	0·66	1·08	0·60	0·87	0·59
Mg-no.	0·70	0·73	0·72	0·68	0·71	0·66	0·69	0·71	0·73	0·72	0·70
Rb	187	140	168	152	194	264	172	146	148	140	135
Ba	1830	1650	2590	1267	1565	2117	2512	1844	2256	2000	1794
Sr	1034	1048	1671	1026	1325	1374	1536	1259	1410	1269	1185
Y	29·4	25·3	26·9	22·3	24·8	27·2	28·0	24·7	26·8	25·1	23·5
Zr	172	160	260	145	139	183	195	139	159	167	155
Nb	8·55	6·44	9·93	5·25	5·00	8·25	7·20	5·56	7·03	6·52	5·35
Pb	30·6	30·7	36·9	31·9	39·2	43·6	74·0	30·9	32·5	31·0	30·0
Th	5·35	6·49	12·8	8·45	9·95	13·2	14·4	7·09	10·8	9·04	6·47
Ni	463	366	218	144	247	130	84	137	248	242	189
Sc	29·5	20·3	15·9	16·1	22·5	17·6	16·2	23·1	16·3	15·5	16·6
V	313	268	168	137	168	97	114	148	173	168	166
Cr	594	391	400	388	414	291	574	404	379	369	446
Co	45·3	29·3	31·2	31·4	26·5	23·2	39·2	25·9	27·0	26·2	27·6
La	32·1	33·1	59·0	27·0	32·4	38·8	47·3	35·1	52·5	43·0	33·4
Ce	64·6	66·4	119·2	56·5	68·8	80·9	95·2	74·4	110·1	87·4	68·8
Nd	31·7	29·8	58·0	28·1	32·1	39·3	43·5	32·2	49·8	38·8	29·7
Sm	7·07	6·05	11·0	5·96	6·77	8·20	8·99	6·82	9·41	7·84	6·03

Sample no.:	CH7F002	HD92	WH91	CH9786	CH9854	CH9783	CH9803	JH21	LH14	LH15	JH22
Locality:	Beiya	Haidong	Wenhua	Haidong	Xiangyun	Haidong	Xiangyun	Janchuan	Lijiang	Liuhe	Janchuan
Field:	Beiya	Xiangyun	Yao'an	Xiangyun	Xiangyun	Xiangyun	Xiangyun	Janchuan	Lijiang	Liuhe	Janchuan
Latitude:	26°10·21′	25°40·95′	25°23·12′	25°40·36′	25°32·01′	25°40·95′	25°32·01′	26°35·14′	26°54·52′	26°25·02′	26°35·07′
Longitude:	100°18′	100°21·41′	101°15·16′	100°20·61′	100°30·98′	100°21·41′	100°30·04′	99°50·18′	100°14·13′	100°20·07′	99°50·08′
D (km):	8	18	68	16	10	18	5	3	35	27	1
Eu	1·95	1·78	2·80	1·61	1·78	2·07	2·33	1·93	2·35	2·17	1·83
Tb	0·90	0·70	1·09	0·74	0·79	0·91	0·96	0·79	0·87	0·93	0·78
Yb	2·53	1·72	1·80	1·76	1·86	1·91	1·91	1·82	1·80	1·83	1·81
Lu	0·38	0·27	0·20	0·29	0·26	0·32	0·28	0·27	0·27	0·27	0·28
Hf	4·72	3·81	5·90	3·65	3·48	4·69	4·86	3·68	3·91	3·83	3·94
Ta	0·46	0·43	0·59	0·44	0·44	0·67	0·56	0·49	0·45	0·46	0·45
U	1·34	2·85	3·21	3·15	2·57	3·51	3·02	2·83	2·89	2·76	2·74

D is the distance from the western margin of the Yangtze craton. The names of the volcanic fields are as in Fig. 1. Mg-number = $Mg/(Mg + Fe^{2+})$, calculated assuming $Fe_2O_3/(FeO + Fe_2O_3) = 0.15$. Major element values are normalized to 100% on a volatile-free basis.
*Total Fe is given as Fe_2O_3.

samples and standards, is less than 5% for all the elements given in Table 3. Analyses of the international standards are in agreement with the recommended values (Govindaraju, 1994), which deviate less than 3% from published values. The detailed analytical procedures follow those of Jin & Zhu (2000) and Zhang *et al.* (2002). The major and trace element concentrations of the samples analysed at KUL were reanalysed using the above procedure; the results are within analytical error, except for the Rb concentrations of samples CH9716, CH9722, CH9723 and CH7F002 and the Ba content of sample CH7F002, which are outside analytical error (see Appendix A). It is possible that the samples that were sent to KUL from Beijing for analysis were too small, leading to unrepresentative analyses. For the four anomalous samples (i.e. the Rb concentrations of samples CH9716, CH9722, CH9723 and CH7F002 and the Ba content of sample CH7F002), we used the ICP-MS analyses instead.

Sr–Nd–Pb isotope compositions of selected samples were analysed at the Institute of Geology and Geophysics, Chinese Academy of Sciences, Beijing, China. For Rb–Sr and Sm–Nd isotope analyses, rock chips of less than 20 mesh size were used. Before being ground to 200 mesh in an agate rill mill, the chips were leached in purified 6N HCl for 24 h at room temperature to minimize the influence of surface alteration or weathering, especially for Sr isotopic ratios. Sample powders were spiked with mixed isotope tracers, then dissolved in Teflon capsules with HF + HNO_3. Sr and REE fractions were separated in solution using cationic ion-exchange resin columns. Nd was separated from REE fractions using cationic ion-exchange columns and P507 extraction and eluviation resin (Richard *et al.*, 1976; Zhang *et al.*, 2002; Fan *et al.*, 2003). The collected Sr and Nd fractions were evaporated and dissolved in 2% HNO_3 to give solutions for analysis by mass spectrometry. Isotopic measurement was performed on a VG-354 mass spectrometer. The mass fractionation corrections for Sr and Nd isotopic ratios were based on $^{86}Sr/^{88}Sr = 0{\cdot}1194$ and $^{146}Nd/^{144}Nd = 0{\cdot}7219$, respectively. The international standard La Jolla yielded $^{143}Nd/^{144}Nd = 0{\cdot}511863 \pm 10$ ($n = 16$) and international standard NBS987 gave $^{87}Sr/^{86}Sr = 0{\cdot}710242 \pm 11$ ($n = 14$). The whole procedure blank is less than 4×10^{-10} g for Sr and 8×10^{-11} g for Nd. Analytical errors for Sr and Nd isotopic ratios are given as 2σ. The $^{87}Rb/^{86}Sr$ and $^{147}Sm/^{144}Nd$ ratios were calculated using the Rb, Sr, Sm and Nd concentrations obtained by ICP-MS. The initial $^{87}Sr/^{86}Sr$ and $^{143}Nd/^{144}Nd$ ratios were calculated using a mean $^{40}Ar/^{39}Ar$ age of 35 Ma.

For Pb isotope measurements, to minimize the contamination from the atmosphere during the crushing process, <100 mesh powders of samples were used; 200 mg of powder was weighed into a Teflon cup, spiked and dissolved in concentrated HF at 800°C for 72 h. Pb was separated and purified by conventional anion-exchange techniques (AG1X8, 200–400 resin; Zhang *et al.*, 2002) with dilute HBr as eluant. The whole procedure blank is less than 0·4 ng. Pb isotopic ratios were measured with a VG-354 mass spectrometer. During the period of analysis, repeat analyses of international standard NBS981 yielded $^{206}Pb/^{204}Pb = 16{\cdot}9506 \pm 2$ ($n = 20$), $^{207}Pb/^{204}Pb = 15{\cdot}5072 \pm 6$ ($n = 20$), and $^{208}Pb/^{204}Pb = 36{\cdot}6786 \pm 4$ ($n = 22$). Each sample was measured at least twice to ensure reproducibility of the analyses and the results given are averages. The average 2σ uncertainty for measured ratios of $^{206}Pb/^{204}Pb$, $^{207}Pb/^{204}Pb$ and $^{208}Pb/^{204}Pb$ is 0·2‰, 0·8‰ and 0·6‰ per a.m.u. (atomic mass unit), respectively. Detailed sample preparation and analytical procedures for the Sr–Nd–Pb isotope measurements follow those of Zhang *et al.* (2002) and Fan *et al.* (2003). The results are presented in Tables 4 and 5.

GEOCHEMICAL CHARACTERISTICS

The geochemical data (Table 3) show that the WSYP lavas are potassic ($K_2O > Na_2O$) to ultrapotassic, with K_2O >3 wt %, MgO >3 wt % and K_2O/Na_2O ratios ranging from 2·1 to 4·2 (wt %), based on the criteria of Foley *et al.* (1987). The compositions of the WSYP rocks are plotted in a total-alkali vs silica classification diagram (Le Bas *et al.*, 1986; Le Maitre *et al.*, 1989) subdivided into groups based on their distance from the western margin of the Yangtze craton (Fig. 2a). Samples from different distances from the margin of the craton normally overlap and define a scattered trend (Fig. 2a) that lies almost totally within the basalt–trachybasalt–basaltic trachyandesite–trachyandesite fields. A plot of K_2O vs SiO_2 (Fig. 2b) shows that the samples plot in the shoshonitic series field, and also within the field for minettes as defined by Rock *et al.* (1991). Moreover, Ce/Yb vs Sm variations (Fig. 3) also indicate that most rocks plot in the field of calc-alkaline lamprophyres (Rock *et al.*, 1991).

The lavas are not peralkaline because the molar (K + Na)/Al ratios of the samples vary between 0·40 and 0·99. Mg-values [= molar Mg × 100/(Mg+Fe^{2+}) ratio, calculated assuming $Fe_2O_3/(FeO + Fe_2O_3) = 0{\cdot}15$] range from 66 to 78 (Table 3). SiO_2, Na_2O and Al_2O_3 increase, whereas CaO, Fe_2O_3, Ni, and Cr decrease, with decreasing MgO (Fig. 4 and Table 3). However, K_2O forms a near-horizontal trend when plotted against SiO_2 (Fig. 2b) and MgO (Fig. 4f). The abundances of the compatible elements (e.g. MgO, Fe_2O_3, CaO, Ni, Sc, Cr) in the WSYP igneous rocks from different distances from the western margin of the Yangtze craton display similar variation trends (Fig. 4). Compared with the Permo-Triassic Emeishan flood basalts in the western part of the Yangtze craton, which have been considered a consequence of mantle plume activity (Chung *et al.*, 1998*a*;

Table 4: Sr and Nd isotope data for WSYP rocks

Sample no.	$^{87}Rb/^{86}Sr$	$^{87}Sr/^{86}Sr \pm 2\sigma$	$(^{87}Sr/^{86}Sr)_i$	εSr(i)	$^{147}Sm/^{144}Nd$	$^{143}Nd/^{144}Nd \pm 2\sigma$	$(^{143}Nd/^{144}Nd)_i$	εNd(i)	T_{DM}Nd (Ga)
CH9716	0·1712	0·706516 ± 18	0·706431	28·0	0·1041	0·512602 ± 9	0·512578	−0·3	0·69
EX06	0·2195	0·706240 ± 16	0·706131	23·7	0·1044	0·512487 ± 8	0·512463	−2·5	0·84
SH14	0·2138	0·706614 ± 21	0·706508	29·1	0·1110	0·512457 ± 9	0·512432	−3·1	0·93
SH15	0·2913	0·707758 ± 25	0·707613	44·8	0·1022	0·512442 ± 11	0·512419	−3·4	0·88
CH9722	0·2148	0·706462 ± 17	0·706355	26·9	0·1015	0·512489 ± 7	0·512466	−2·5	0·82
CH9723	0·2088	0·706289 ± 16	0·706185	24·5	0·1172	0·512489 ± 12	0·512462	−2·6	0·93
GZ0029	0·2701	0·706126 ± 19	0·705992	21·8	0·1100	0·512579 ± 9	0·512554	−0·8	0·76
CH7F007	0·4242	0·707841 ± 18	0·707630	45·0	0·1019	0·512385 ± 11	0·512362	−4·5	0·95
WH79	0·1927	0·709274 ± 14	0·709178	67·0	0·1156	0·512017 ± 12	0·511991	−11·8	1·58
WH76	0·2814	0·709746 ± 12	0·709606	73·1	0·1068	0·512011 ± 10	0·511987	−11·8	1·47
WH91	0·2828	0·709781 ± 19	0·709640	73·6	0·1194	0·512038 ± 8	0·512011	−11·4	1·60
CH9783	0·5406	0·706603 ± 22	0·706334	26·6	0·1309	0·512440 ± 9	0·512410	−3·6	1·15
CH9786	0·4173	0·706349 ± 16	0·706142	23·9	0·1333	0·512534 ± 7	0·512503	−1·7	1·02
CH9803	0·3143	0·707113 ± 21	0·706957	35·5	0·1296	0·512387 ± 14	0·512357	−4·6	1·22
CH9854	0·4127	0·705053 ± 16	0·704848	5·5	0·1324	0·512823 ± 16	0·512793	3·9	0·54

Chondritic Uniform Reservoir (CHUR) at the present day [$(^{87}Rb/^{86}Sr)_{CHUR} = 0·0847$ (McCulloch & Black, 1984); $(^{87}Sr/^{86}Sr)_{CHUR} = 0·7045$ (DePaolo, 1988); $(^{147}Sm/^{144}Nd)_{CHUR} = 0·1967$ (Jacobsen & Wasserburg, 1980); $(^{143}Nd/^{144}Nd)_{CHUR} = 0·512638$ (Goldstein *et al.*, 1984)] were used for the calculations. Nd depleted mantle model ages (T_{DM}) were calculated using $(^{147}Sm/^{144}Nd)_{DM} = 0·225$ (McCulloch *et al.*, 1983) and $(^{143}Nd/^{144}Nd)_{DM} = 0·51315$ (Peucat *et al.*, 1988) at the present day. $\lambda_{Rb} = 1·42 \times 10^{-11}$ year^{-1} (Steiger & Jäger, 1977); $\lambda_{Sm} = 6·54 \times 10^{-12}$ year^{-1} (Lugmair & Marti, 1978). Both εSr(i) and εNd(i) were obtained by assuming 35 Ma for the age of the WSYP rocks (Table 1).

Table 5: Pb isotope data of the WSYP rocks

Sample no.	$^{206}Pb/^{204}Pb$	$^{207}Pb/^{204}Pb$	$^{208}Pb/^{204}Pb$	^{204}Pb%	$^{238}U/^{204}Pb$	$^{235}U/^{204}Pb$	$^{232}Th/^{204}Pb$	$(^{206}Pb/^{204}Pb)_i$	$(^{207}Pb/^{204}Pb)_i$	$(^{208}Pb/^{204}Pb)_i$	Δ7/4	Δ8/4
CH9716	18·571	15·609	38·715	1·353	9·470	0·070	47·231	18·520	15·607	38·634	10·8	61·6
EX06	18·037	15·512	38·310	1·373	4·957	0·036	28·812	18·010	15·510	38·260	6·7	85·9
SH14	18·097	15·484	38·094	1·376	8·228	0·060	44·970	18·052	15·482	38·016	3·4	56·4
SH15	18·462	15·551	38·453	1·361	4·999	0·037	27·161	18·435	15·549	38·406	6·0	49·0
CH9722	18·161	15·524	38·295	1·370	6·452	0·047	40·348	18·126	15·522	38·226	6·6	68·5
CH9723	18·421	15·655	38·720	1·355	9·243	0·068	44·899	18·370	15·653	38·642	17·1	80·6
GZ0029	18·104	15·502	38·093	1·376	5·520	0·040	29·272	18·074	15·501	38·042	5·1	56·4
CH7F007	18·019	15·520	38·016	1·378	6·078	0·045	21·758	17·986	15·519	37·978	7·8	60·6
WH79	17·849	15·453	38·376	1·376	5·368	0·039	22·891	17·820	15·452	38·336	2·9	116·5
WH76	17·716	15·451	38·313	1·380	7·134	0·052	25·142	17·677	15·449	38·270	4·2	127·1
WH91	17·860	15·516	38·498	1·372	5·480	0·040	22·634	17·830	15·515	38·459	9·1	127·6
CH9783	18·556	15·602	38·552	1·357	5·122	0·038	19·910	18·528	15·601	38·518	10·1	49·1
CH9786	18·534	15·565	38·468	1·359	6·287	0·046	17·438	18·500	15·563	38·437	6·7	44·4
CH9803	18·376	15·440	38·294	1·368	2·583	0·019	12·674	18·362	15·440	38·272	−4·2	44·5
CH9854	18·420	15·416	38·412	1·365	4·143	0·030	16·607	18·397	15·415	38·383	−7·0	51·4

$\lambda(^{238}U) = 0·155125 \times 10^{-9}$ year^{-1}, $\lambda(^{235}U) = 0·98485 \times 10^{-9}$ year^{-1} and $\lambda(^{232}Th) = 0·049475 \times 10^{-9}$ year^{-1} (Steiger & Jäger, 1977). $\Delta 7/4 = [(^{207}Pb/^{204}Pb)_i - (^{207}Pb/^{204}Pb)_{NHRL}] \times 100$; $\Delta 8/4 = [(^{208}Pb/^{204}Pb)_i - (^{208}Pb/^{204}Pb)_{NHRL}] \times 100$. $(^{207}Pb/^{204}Pb)_{NHRL} = 0·1084 \times (^{206}Pb/^{204}Pb)_i + 13·491$ (Hart, 1984); $(^{208}Pb/^{204}Pb)_{NHRL} = 1·209 \times (^{206}Pb/^{204}Pb)_i + 15·627$ (Hart, 1984). Initial Pb isotope ratios were obtained assuming an age of 35 Ma for the WSYP rocks (Table 1).

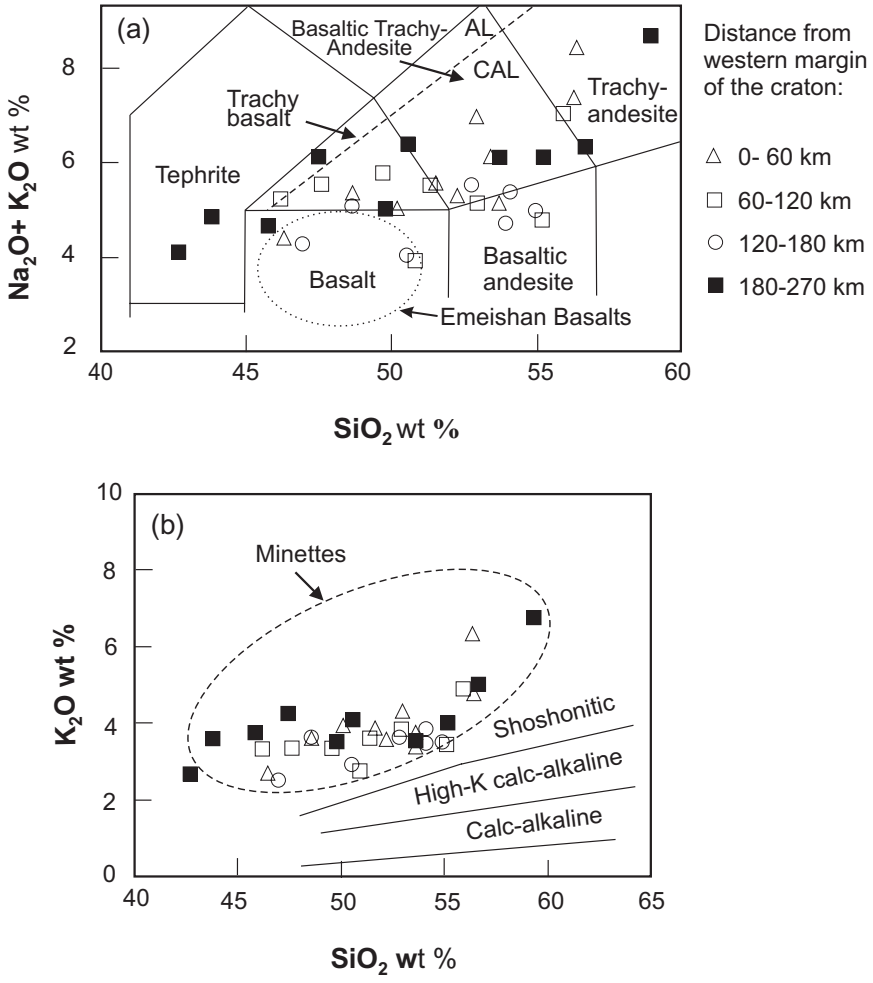

Fig. 2. (a) $K_2O + Na_2O$ vs SiO_2 diagram. The dashed line represents the boundary between AL (alkaline lamprophyres) and CAL (calc-alkaline lamprophyres) after Rock *et al.* (1991). Dotted line outlines the field of mantle plume-derived Emeishan basalts in the western part of the Yangtze craton (Xu *et al.*, 2001*a*). All values have been recalculated to 100 wt % on a volatile-free basis (see Table 3). Classification boundaries are from Le Bas *et al.* (1986) and Le Maitre *et al.* (1989). (b) K_2O vs SiO_2 diagram. Dashed line outlines the field of minettes (Rock *et al.*, 1991). The symbols are as in Fig. 2a. Data have been normalized to 100% volatile-free. Continuous lines shown are classification boundaries taken from Rickwood (1989).

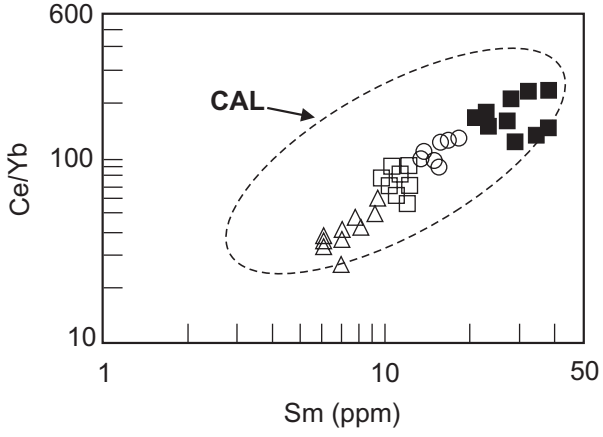

Fig. 3. Ce/Yb vs Sm (ppm) diagram. The dashed line outlines the field of CAL (calc-alkaline lamprophyres) after Rock *et al.* (1991). The symbols are as in Fig. 2a.

Xu *et al.*, 2001*a*), the WSYP magmatic rocks generally have lower contents of Fe_2O_3, Na_2O, CaO, Al_2O_3 and TiO_2 at a given MgO (>6%) content (Fig. 4a–e). The Zr–Nb diagram (Fig. 5) shows that the WSYP lavas are similar to Western Mexican minettes, which were generated in an active subduction-related tectonic setting (Luhr *et al.*, 1989; Carmichael *et al.*, 1996). The most silica-poor samples from the Yanyuan and Xichang volcanic fields have relatively high contents of compatible elements (e.g. MgO 7·5–14·5%, Cr 277–708 ppm, Sc 15–24 ppm, and Ni 90–585 ppm). The low contents of phenocrysts of these rocks, which possess about 1–4% olivine phenocrysts (Table 2), make it unlikely that these characteristics result from the accumulation of earlier crystallizing ferromagnesian minerals, such as olivine, clinopyroxene and Cr-spinel, although the sample with the highest Ni content (585 ppm) might have accumulated some olivine.

Primitive mantle-normalized incompatible element diagrams show the strongly enriched nature of the WSYP potassic rocks (Fig. 6). The normalized patterns range from several times primitive mantle for heavy REE (HREE), Ti, and Y, to several hundred times for large ion lithophile elements (LILE), such as Ba, Rb, U, K, Pb, and Sr. The trace element patterns are distinguished by negative Nb, Ta and Ti anomalies, despite the generally high contents of these elements (Table 3 and Fig. 6). All of the rocks have moderately to slightly positive Ba anomalies. Almost all of the samples show slightly positive Sr anomalies relative to Ce and P. Either positive or negative anomalies for P, Zr and Hf are exhibited in some samples. Rocks located in the northeastern part of the traverse (Fig. 1) show slightly negative K anomalies relative to La and U (Fig. 6c and d); however, most rocks in the southwestern part of the traverse (Fig. 1) have slightly positive K anomalies (Fig. 6a and b). Th, light REE (LREE) and some high field strength elements (HFSE; e.g. Zr and Hf) have relatively flat patterns compared with the strong enrichment in Rb, Ba, U, K, Pb and Sr (Fig. 6), resulting in overall high LILE/HFSE ratios of the WSYP igneous rocks.

The most striking characteristics of the WSYP rocks are their relatively high contents and considerable variations in the abundance of LILE and LREE (Table 3 and Fig. 7). For example, Ba abundances range from 1300 to 6600 ppm (Fig. 7), Rb from 120 to 290 ppm, Sr from 1000 to 3500 ppm, Ce from 60 to 540 ppm, and La from 30 to 260 ppm. In element–element variation diagrams, no correlation exists between incompatible trace element contents (e.g. Ba, Sr, Rb, La, Sm) and MgO, and

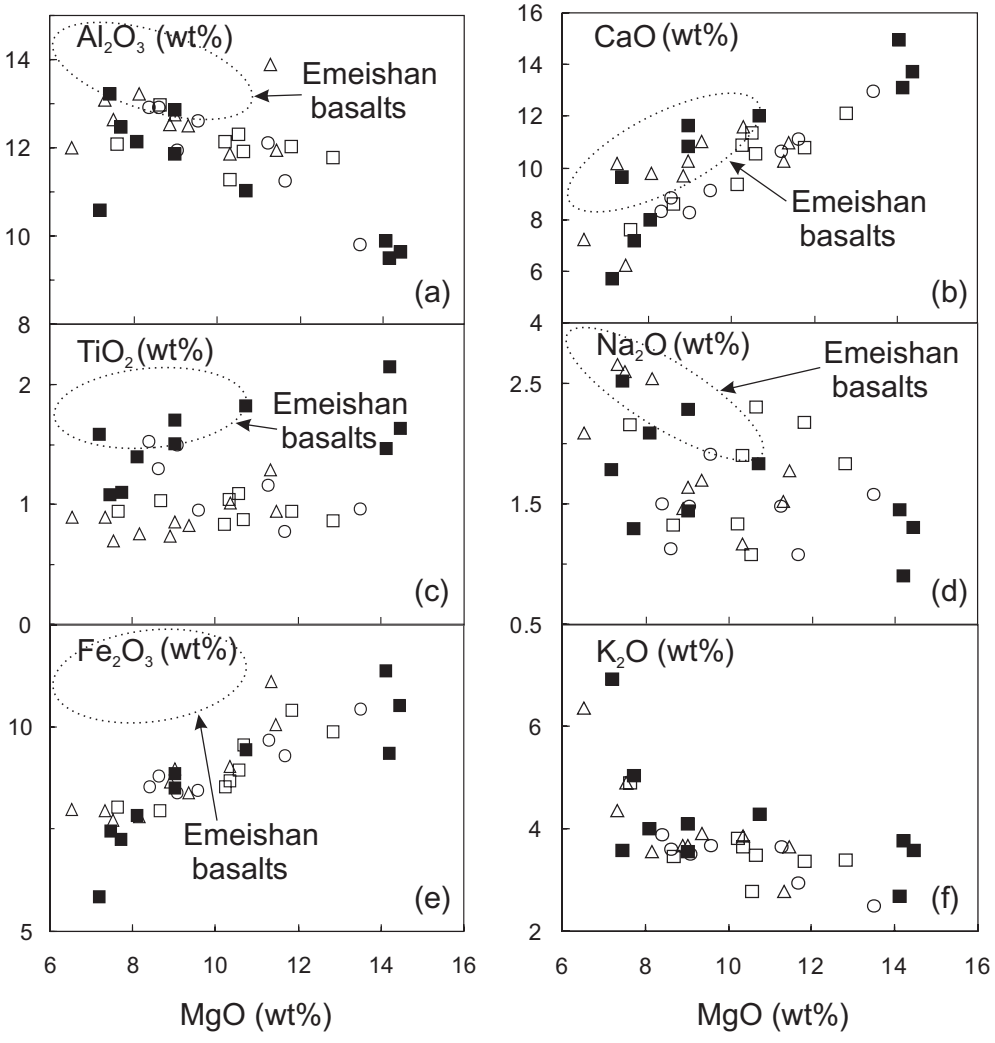

Fig. 4. Selected major and trace elements vs MgO (wt %) illustrating the broad compositional range of the WSYP samples. All the major element data have been recalculated to 100% on a volatile-free basis (see Table 3). The dotted line outlines the field of the Emeishan basalts in the western part of the Yangtze craton (Xu *et al.*, 2001*a*). The contents of K_2O, Ba, Sr and Rb in the Emeishan basalts are too low to show in this figure. (a) Al_2O_3; (b) CaO; (c) TiO_2; (d) Na_2O; (e) Fe_2O_3; (f) K_2O; (g) La; (h) Sm; (i) Ba; (j) Sr; (k) Rb; (l) Ni. The symbols are as in Fig. 2a.

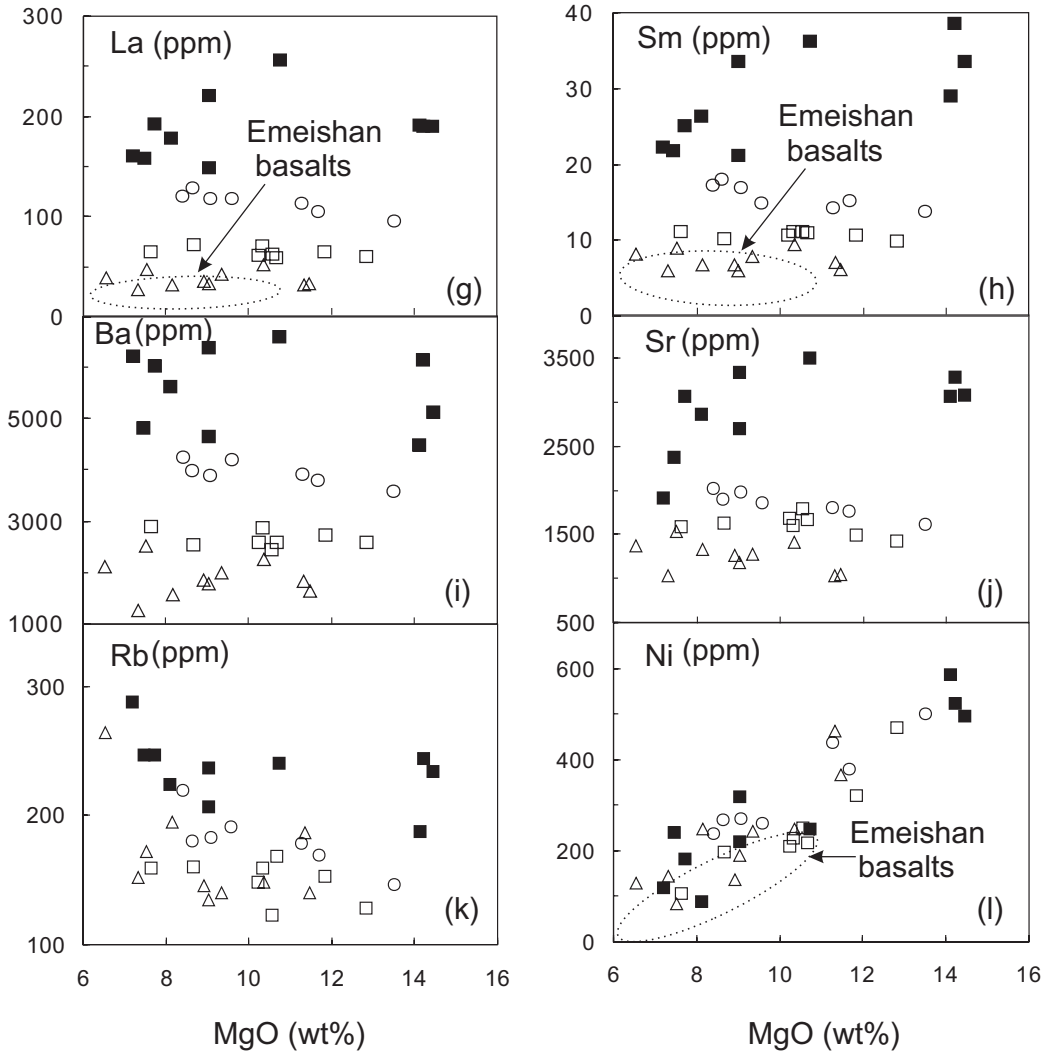

Fig. 4. Continued

the plots show considerable scatter (Fig. 4g–k). The contents of some incompatible trace elements (e.g. Ba, Th, Sr) increase significantly with distance from the western margin of Yangtze craton (Fig. 7). Variations in the ratios of incompatible elements (e.g. Ba/La, La/Yb, Sr/Ce, Ba/Rb) also show similar correlations (both positive and negative). MgO contents show relatively little variation with distance from the western margin of the Yangtze craton (Fig. 7). Because no systematic magma differentiation trends were observed with the distance from the western margin of the craton, combined with the relatively high MgO, Ni, and Cr contents of the WSYP rocks (Table 3 and Fig. 4), the compositional zonation probably reflects the characteristics of the mantle source region from which the WSYP magmas were derived and the degree of partial melting.

On the basis of discontinuities in incompatible trace element contents (e.g. Ba, Sr, Th, Pb), combined with variations in their ratios (e.g. Ba/La and Sr/Ce), the WSYP rocks may be broadly divided into three subgroups: (1) a subgroup with relatively high LILE/LREE ratios (e.g. Ba/La and Sr/Ce); (2) a subgroup with intermediate LILE/LREE ratios (e.g. Ba/La and Sr/Ce); (3) a subgroup with relatively low LILE/LREE ratios (e.g. Ba/La and Sr/Ce). These three subgroups are mainly related to the distance from the western margin of the Yangtze craton. The characteristics of each subgroup are summarized as follows.

Subgroup with relatively high LILE/LREE ratios

The samples with high Sr/Ce and Ba/La are located along the ASRR shear zone (Fig. 1), closest to the western margin of the Yangtze craton (Fig. 7); these include the Xiangyun, Liuhe, Lijiang and Beiya volcanic fields and

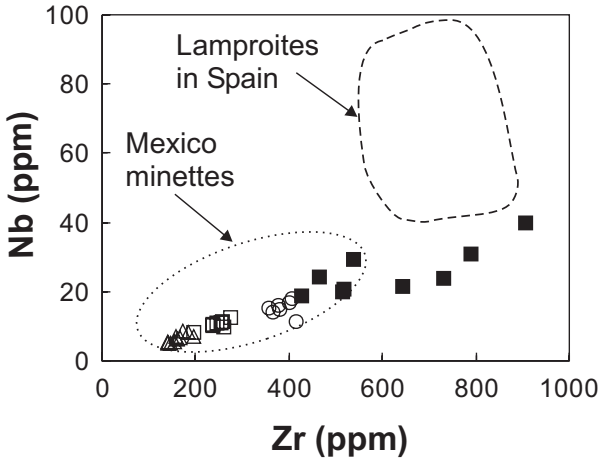

Fig. 5. Nb (ppm) vs Zr (ppm) contents of WSYP calc-alkaline lamprophyres compared with other potassic igneous rocks. The data for lamproites in Spain (dashed line) and Mexican minettes (dotted line) are from Venturelli *et al.* (1984), Luhr *et al.* (1989) and Rock *et al.* (1991). The symbols are as in Fig. 2a.

rocks from the Janchuan area (Figs 1 and 7). Their Sr/Ce and Ba/La ratios range from 12·8 to 19·3 and 43·0 to 57·1, respectively (Table 3 and Fig. 7), among the highest ratios found in the WSYP rocks. The rocks have positive Sr and positive or negative P anomalies in primitive mantle-normalized trace element diagrams, relatively low abundances of Ba, Sr, Pb, Th, U, LREE and Zr, and the lowest LREE/HREE and highest LILE/HFSE ratios among the WSYP rocks (Figs 6a and 8). They have similar incompatible element ratios (e.g. Ba/Th, Sr/Ce, Ce/Pb, La/Yb) to the active continental margin minettes of Western Mexico (Luhr *et al.*, 1989).

Subgroup with relatively low LILE/LREE ratios

The low Sr/Ce and Ba/La samples have slightly negative P and positive or negative Sr anomalies in primitive mantle-normalized trace element diagrams, and the lowest Sr/Ce (5·8–8·8) and Ba/La ratios (23·4–38·7) among the WSYP samples (Figs 6d and 7). These lamprophyres are located at the NE end of the traverse (Figs 1 and 7), far from the ASRR shear zone, and include the Yanyuan volcanic field and rocks from the Xichang area (Fig. 1). By contrast with the subgroup with relatively high LILE/LREE ratios, the absolute abundances of Ba, Th, U, Pb, LREE, Sr, and Zr are very high (Table 3 and Fig. 7). Likewise, they have the highest LREE/HREE (Fig. 7) and lowest LILE/HFSE ratios among the WSYP lamprophyres (Fig. 8).

Subgroup with intermediate LILE/LREE ratios

These rocks are transitional between the high LILE/LREE and low LILE/LREE subgroups. The lavas have intermediate Sr/Ce (7·5–14·2) and Ba/La ratios (31·0–44·6) (Figs 6b, c, and 7), and intermediate LILE abundances and moderate LILE/HFSE and LREE/HREE ratios (Figs 7 and 8). Spatially, they are distributed in the middle part of the traverse (Figs 1 and 7), predominantly in the Yao'an, Yongren and Ninglang volcanic fields (Fig. 1).

Sr–Nd–Pb isotope compositions

The WSYP samples display relative high values of $^{87}Sr/^{86}Sr_{(i)}$ (0·704848–0·709640), low $^{143}Nd/^{144}Nd_{(i)}$ (0·511987–0·512793), and high $^{207}Pb/^{204}Pb_{(i)}$ (15·42–15·65) and $^{208}Pb/^{204}Pb_{(i)}$ ratios (37·98–38·64) at a given $^{206}Pb/^{204}Pb_{(i)}$ ratio (17·68–18·53) (Tables 4 and 5). These isotope ratios display considerable variation among the three subgroups of the WSYP rocks. The Sr–Nd isotope compositions exhibit a strong negative correlation (Fig. 9a). The Sr–Nd–Pb isotopic compositions of Globally Subducted Sediment (GLOSS, Plank & Langmuir, 1998) and those of potassic rocks from the ASRR shear zone (Zhang *et al.*, 2000; Wang *et al.*, 2001) are shown for reference in Fig. 9. Depleted Mantle Nd model ages (T_{DM}; Table 4) were calculated based on the assumption of extraction of the WSYP lavas from an upper-mantle reservoir with present-day $^{143}Nd/^{144}Nd$ and $^{147}Sm/^{144}Nd$ of 0·51315 (Peucat *et al.*, 1988) and 0·225 (McCulloch *et al.*, 1983), respectively. The model ages of the WSYP samples range from 0·5 to 1·6 Ga (Table 4). In plots of $^{207}Pb/^{204}Pb_{(i)}$ vs $^{206}Pb/^{204}Pb_{(i)}$, and $^{208}Pb/^{204}Pb_{(i)}$ vs $^{206}Pb/^{204}Pb_{(i)}$ (Fig. 9c and d), the WSYP potassic rocks generally plot above the Northern Hemisphere Reference Line (NHRL; Hart, 1984). In all isotope projections, the fields of GLOSS, together with the isotope compositions of the potassic rocks along the ASRR shear zone (Zhang *et al.*, 2000; Wang *et al.*, 2001), overlap those of the high LILE/LREE ratio subgroup of the WSYP rocks.

DISCUSSION

The primary magmas and enrichment processes of the mantle source region

It has been suggested that primary magmas generated by equilibrium partial melting of mantle peridotite should have high Mg-numbers (around 70 or more), along with high Ni and Cr concentrations (Frey *et al.*, 1978). The high compatible element abundances (in particular, sample CH9723, which has >500 ppm Ni, >500 ppm Cr and an Mg-number of 78; Table 3) in most of the WSYP rocks, combined with the presence of mantle-derived xenoliths, suggest that they probably are candidates for near-primary melts of mantle peridotite. The predominance of olivine and clinopyroxene phenocrysts in the WSYP magmatic rocks indicates that the lower MgO

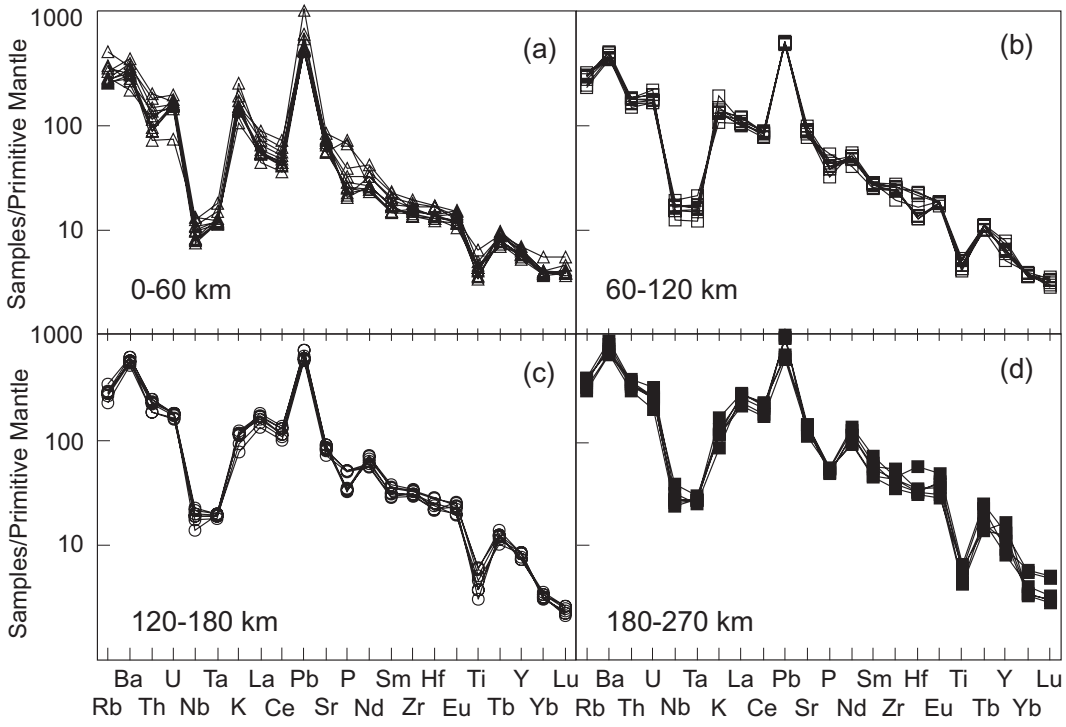

Fig. 6. Primitive mantle-normalized incompatible element diagrams calculated with normalization factors from Sun & McDonough (1989). The WSYP potassic samples can be subdivided into those that have high Ba/La and Sr/Ce ratios (a), those that have intermediate Ba/La and Sr/Ce (b, c), and those that have low Ba/La and Sr/Ce ratios (d). Distances from the craton margin are indicated. The symbols are as in Fig. 2a.

contents in some rocks may be explained by minor fractionation of these phases. Although most of the WSYP magmatic rocks are consistent with primitive magma compositions, some samples have the characteristics of moderately evolved magmas (relatively low MgO, Ni, Cr; Table 3). To estimate the WSYP melt segregation depths, primitive melt compositions with an assumed 15 wt % MgO were calculated using an extrapolation method by fitting least-squares linear regression lines to the composition arrays at different distances from the western margin of the Yangtze craton. The rationale for this calculation, following Scarrow & Cox (1995), Turner & Hawkesworth (1995) and Hoang & Flower (1998), is as follows. (1) Relatively low MgO, Ni and Cr contents in the evolved magmas probably were caused by combined fractionation and crustal assimilation (AFC) processes, but extrapolation along the observed data arrays back to 15 wt % MgO should minimize the effects of these processes. (2) The parent magmas are likely to be more magnesian than the most Mg-rich erupted lavas because of shallow-level fractionation processes. The most Mg-rich sample analysed from the WSYP has a bulk-rock MgO content of 14·45 wt % (Table 3); this sample has ~3% olivine phenocrysts based on petrographic observation (Table 2). The MgO content of the melt in equilibrium with the olivine phenocrysts would therefore be ~13 wt %, assuming that the olivine has ~40 wt % MgO. This suggests that the most primitive magmas in the WSYP probably possess at least 13 wt % MgO. Such liquids could be in equilibrium with mantle olivine ($Fo_{85–90}$) (Roeder & Emslie, 1970). (3) Experimental studies show that primary peridotite melts fall within the range 12–17 MgO wt % (Hirose & Kushiro, 1993; Hoang & Flower, 1998). The advantage of this method is that it provides a more robust basis for estimating primitive melt segregation depths by minimizing the effects of shallow-level fractionation processes.

Based on the data in Table 3, the slopes, intercepts and correlation coefficients from least-squares linear regression equations for the variation between MgO and SiO_2 for the various volcanic fields are given in Table 6. The contents of SiO_2 at an assumed 15 wt % MgO, referred to subsequently as Si_{15}, were calculated for each of the volcanic fields by extrapolation using these linear regression equations (Table 6). The relationship between Si_{15} and pressure of melting has been quantified by Hoang & Flower (1998) for both hydrous and anhydrous mantle melting conditions. Because of the presence of phlogopite phenocrysts in the WSYP rocks, we used the equation between Si_{15} and pressure for hydrous conditions (Hoang & Flower, 1998) to calculate melt segregation pressures for the volcanic fields according to the relation

$$P\,(\text{kbar}) = -1{\cdot}458\,(Si_{15}, \text{wt}\,\%) + 89{\cdot}49$$

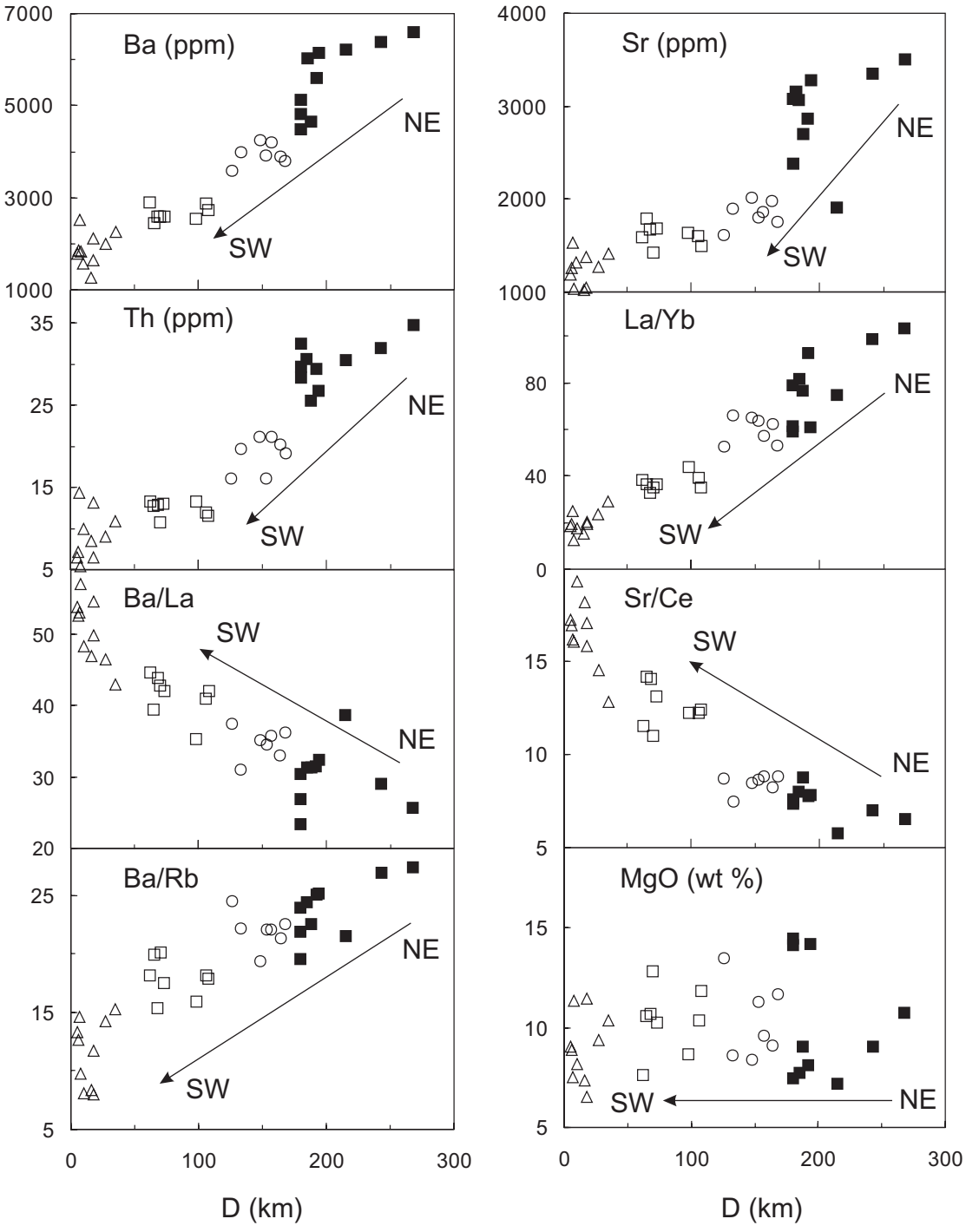

Fig. 7. Geochemical variation with increasing distance *D* (km) from the western margin of the Yangtze craton. The symbols are as in Fig. 2a. NE represents samples located in the NE end of the traverse (see Fig. 1), which is located in the interior of the Yangtze craton; SW represents samples located in the SW end of the traverse (see Fig. 1), which is located in the western margin of the Yangtze craton. Arrow shows the change in composition from NE to SW in the western part of the Yangtze craton.

where Si_{15} denotes the content of SiO_2 in primitive melts with an assumed 15 wt % MgO as shown in Table 6. *P* represents the melt segregation pressure of the primitive magmas generated under hydrous conditions (Table 6). On the basis of the calculations of melt segregation pressure, melt segregation depths in the various volcanic fields were estimated assuming 1 kbar ≈ 3·1 km depth (Table 6).

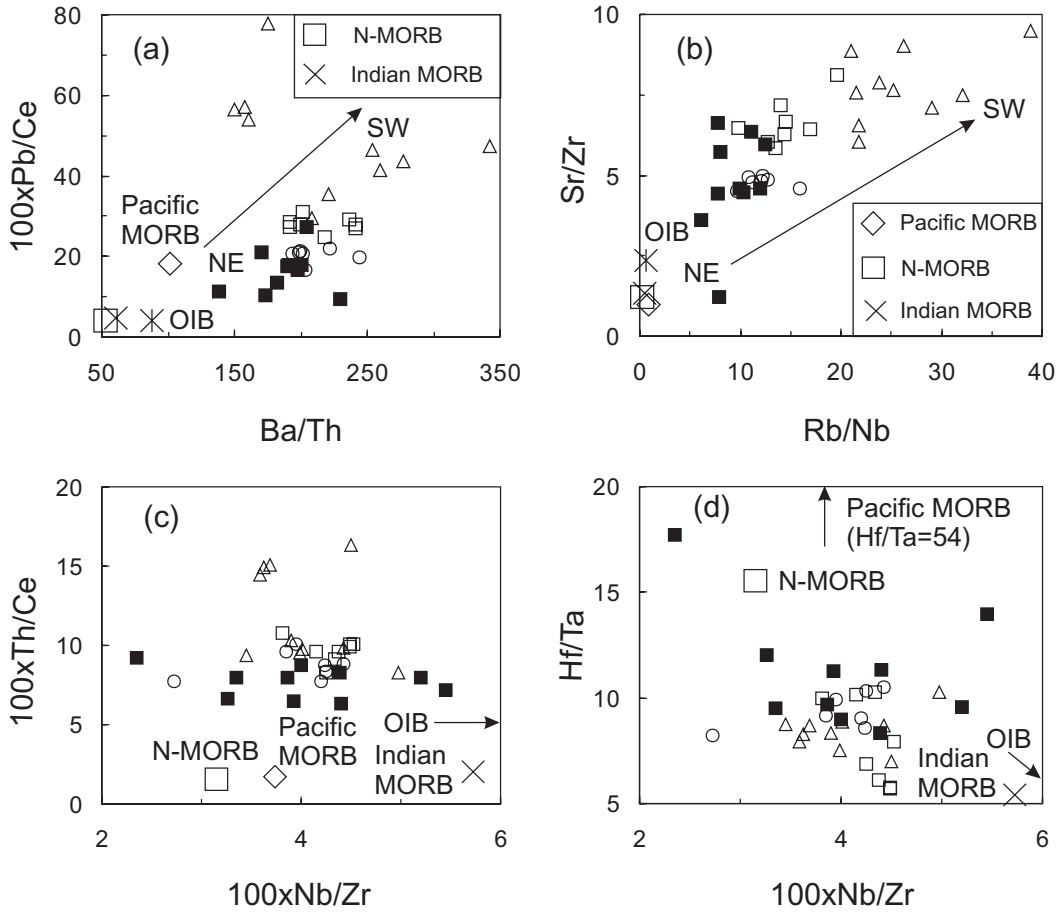

Fig. 8. (a) 100 × Pb/Ce vs Ba/Th diagram. (b) Sr/Zr vs Rb/Nb diagram. (c) 100 × Th/Ce vs 100 × Nb/Zr diagram. (d) Hf/Ta vs 100 × Nb/Zr diagram. The symbols are as in Fig. 2a. The meaning of NE, SW and the arrow is the same as in Fig. 7. The average composition of N-MORB and ocean island basalts (OIB) is from Sun & McDonough (1989); the composition of Indian and Pacific MORB is from the GERM website (http://www.earthref.org/GERM/) and Dosso *et al.* (1988). Atlantic MORB is not shown because of lack of data for Th, Pb, Hf, Ta and Nb in Atlantic MORB on the GERM website.

Calculated results (Table 6) suggest that the melt segregation depths increase from SW to NE with increasing distance from the western margin of the Yangtze craton (Fig. 10a); these depths range from 81 to 88 km. This is consistent with the presence of a northeastward deepening of the low-velocity zone from 70 km to 90 km beneath the western margin of the Yangtze craton on the basis of geophysical studies (Liu *et al.*, 1989; Zhong *et al.*, 2000). The calculated results imply that the WSYP magmas were derived from the spinel stability field. The presence of spinel-bearing mantle xenoliths in the Yanyuan and Xichang rocks (Liu, 1999) supports this inference.

Figure 4 suggests that the source region of the WSYP magmas is relatively refractory compared with that of the earlier mantle plume-related Emeishan basalts, which were also erupted within the western part of the Yangtze craton, because at a given MgO content the samples have overall lower abundances of components probably contributed from mantle clinopyroxene, such as Al_2O_3, Fe_2O_3, Na_2O, CaO and Sc, and slightly higher Cr/Sc ratios (not shown) compared with the Emeishan basalts (YBGMR, 1990; SBGMR, 1991; Xu *et al.*, 2001*a*). The very high abundances of incompatible elements, together with the high LREE/HREE and LILE/HFSE ratios (Figs 6 and 8), suggest that there was a strong enrichment of the source before the onset of partial melting that led to the formation of the potassic magmas, as the generation of such extreme trace element enrichment by partial melting of refractory mantle sources would require unrealistically small melting degrees on the basis of trace element modelling calculations. For example, if the concentration of the trace element Ba in the melt is 6600 ppm (Table 3), the degree of partial melting would be ~0·0035%, assuming a bulk D of 6×10^{-5} (http://www.earthref.org) and C_0 of 0·63 ppm [normal mid-ocean ridge basalt (N-MORB) mantle source; Sun & McDonough, 1989], based on a modal batch partial melting model (Wilson, 1989). The enrichment of the

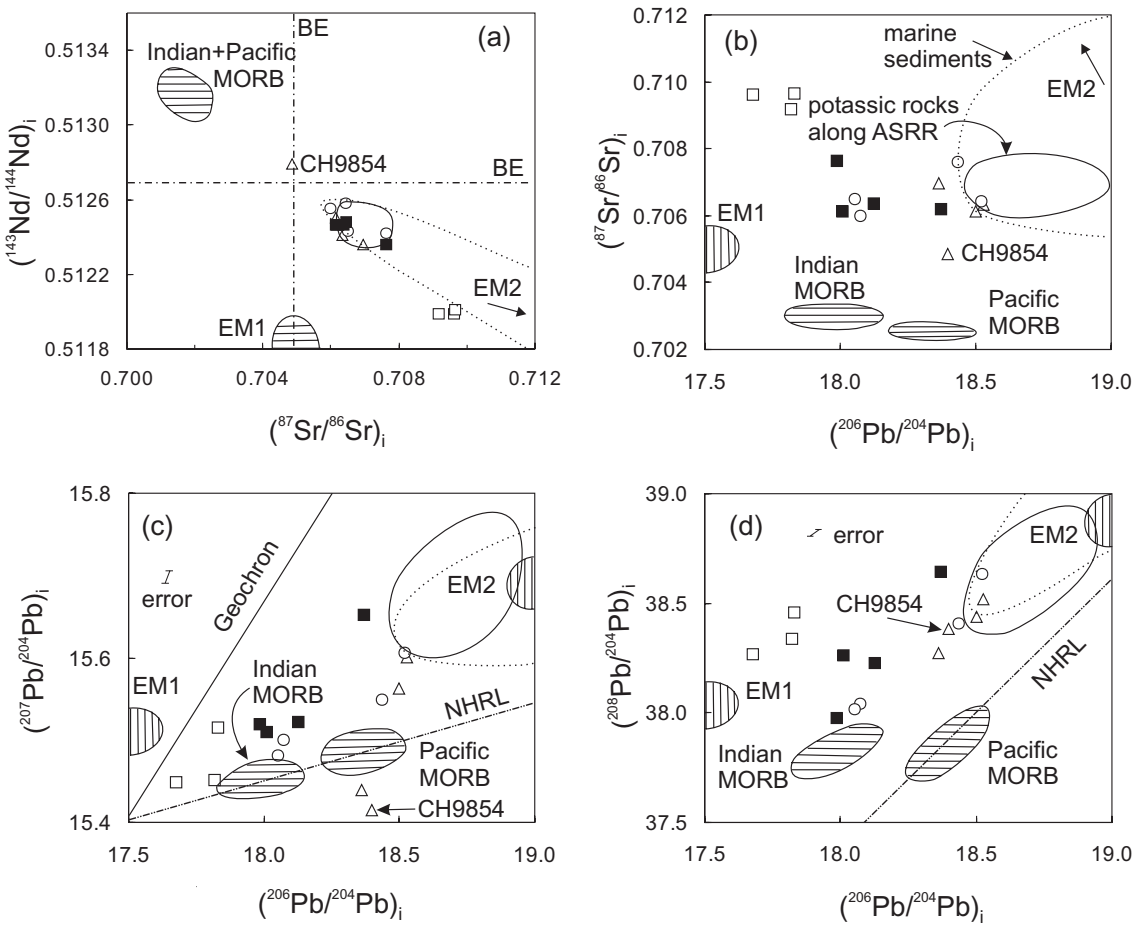

Fig. 9. (a) $(^{143}Nd/^{144}Nd)_i$ vs $(^{87}Sr/^{86}Sr)_i$. (b) $(^{87}Sr/^{86}Sr)_i$ vs $(^{206}Pb/^{204}Pb)_i$. (c) $(^{207}Pb/^{204}Pb)_i$ vs $(^{206}Pb/^{204}Pb)_i$. (d) $(^{208}Pb/^{204}Pb)_i$ vs $(^{206}Pb/^{204}Pb)_i$. The continuous line bounds the field of previously published isotope data for Cenozoic potassic lavas along the ASRR shear zone in each diagram (Zhang *et al.*, 2000; Wang *et al.*, 2001). The dotted line outlines the field of global marine sediments (Plank & Langmuir, 1998). The WSYP igneous rocks show a linear array broadly plotting between Indian MORB-source mantle and marine sediments, probably reflecting two-component mixing. The NHRL (Northern Hemisphere Reference Line; Hart, 1984), EM1 and EM2 (enriched mantle end-members; Zindler & Hart, 1986; Hofmann, 1997; Zou *et al.*, 2000) are shown for reference. Data for Pacific MORB are from Ferguson & Klein (1993). Data for Indian MORB are from Michard *et al.* (1986), Price *et al.* (1986) and Rehkämper & Hofmann (1997). BE, Bulk Silicate Earth. The symbols are as in Fig. 2a.

mantle source is also shown by increases in Th/U, U/Pb, and Rb/Sr and a decrease in Sm/Nd relative to depleted mantle values. Furthermore, the high $^{87}Sr/^{86}Sr$ and relatively low $^{143}Nd/^{144}Nd$ isotopic ratios (Table 4 and Fig. 9) of the WSYP samples, especially those that occur near the ASRR shear zone, require a mantle source region with a time-integrated history of enrichment in Rb and LREE.

The major element variation trends are likely to show the effects of both partial melting and crystal fractionation (Fig. 4). Some compatible trace element trends in Fig. 4 are probably related to fractionation (e.g. the positive correlation between Ni and MgO in Fig. 4l). However, the incompatible trace elements do not show the negative correlations with MgO (Fig. 4g–k) predicted by crystal fractionation models. The high and variable contents of incompatible trace elements probably reflect compositional variations in the source region combined with variable degrees of partial melting. This inference is clearly supported by the positive correlation between La/Yb and La (Fig. 10b), which indicates that the effects of partial melting and source composition were probably more important than fractional crystallization in producing the geochemical variations in the WSYP magmas.

Constraints on mineralogy and composition of the mantle source region

Phlogopite

The majority of the rocks investigated have relatively high K_2O contents and K_2O/Na_2O ratios (>1). For most samples, K_2O contents are relatively constant (3–4%) regardless of the SiO_2 content (Fig. 2b); this must suggest buffering by a potassium-rich residual mineral phase, most probably phlogopite and/or amphibole, in

Table 6: Si_{15} and melt segregation depth in the volcanic fields of the WSYP

Volcanic field	Slope	Intercept	Correlation coefficient	Si_{15} (wt %)	*P* (kbar)	*d* (km)	*D* (km)
Xiangyun	−1·50	65·87	0·83	43·42	26·19	81·18	13·40
Yao'an	−1·82	70·22	0·99	42·98	26·82	83·14	66·25
Panzhihua	−1·95	71·98	0·81	42·80	27·08	83·96	160·50
Yanyuan	−1·68	67·09	0·91	41·84	28·49	88·32	182·60
Xichang	−1·82	69·59	0·80	42·33	27·78	86·12	222·40

Si_{15} is SiO_2 content (wt %) corrected by extrapolating from least-squares linear regressions between SiO_2 and MgO back to 15 wt % MgO. Slope is obtained from least-squares linear regressions between SiO_2 and MgO from the volcanic field data in Table 3. *P* is the melt segregation pressure; *P* (kbar) = −1·458 (Si_{15}, wt %) + 89·49 (Hoang & Flower, 1998). *d* is the melt segregation depth, assuming 1 kbar ≈ 3·1 km. *D* is the average distance of the volcanic fields from the western margin of the Yangtze craton based on those in Table 3.

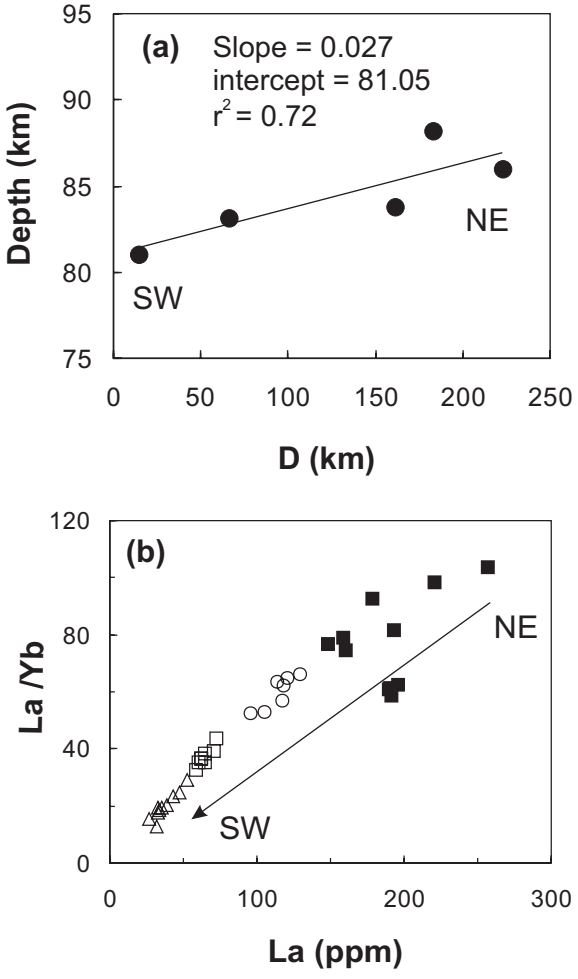

Fig. 10. (a) Melt segregation depth (km) of the WSYP rocks vs distance (*D*, km) from the western margin of the Yangtze craton. Data are from Table 6. The meaning of NE and SW is as in Fig. 7. (b) La/Yb vs La (ppm) diagram. The pronounced correlation between La/Yb and La shows that partial melting was the dominant control on the compositional variation of the WSYP rocks. The meaning of NE, SW and the arrow is as in Fig. 7. The symbols are as in Fig. 2a.

the mantle source region. Although K_2O enrichment in shoshonitic lamprophyres may be partly controlled by orthopyroxene-dominated fractionation (Meen, 1987), the lack of orthopyroxene phenocrysts and the relatively flat K_2O–MgO trend defined by the WSYP lavas (Fig. 4f) probably preclude fractionation-related K enrichment processes. Experimental studies (Edgar *et al.*, 1976; Mengel & Green, 1989) show that mafic melts with about 3·5% K_2O are saturated in phlogopite at high pressure. This saturation limit closely matches the K_2O abundances in most WSYP potassic lavas (Fig. 2b). The presence of phlogopite in the mantle source of the WSYP magmas is also supported by the presence of phlogopite-bearing peridotite xenoliths in the WSYP potassic rocks (Liu, 1999; Qian, 1999). Phlogopite in the source region is further supported by: (1) the relatively low mantle-normalized abundances of K compared with U and La in most lavas from the NE end of the traverse (Fig. 6c and d); (2) positive correlations between La/Rb and La (Fig. 11a), K/Nb and 1/Nb (Fig. 11b), Ba/La and 1/La (Fig. 11c), and Ba/Th and 1/Th (Fig. 11d) for the WSYP rocks, suggesting that the elements K, Rb, and Ba were more compatible than Nb, La, and Th during partial melting in the source region. Although these variation trends could be accounted for as a result of phlogopite fractionation, the relatively flat trends in K_2O content vs SiO_2 (Fig. 2b) and MgO content (Fig. 4f) are inconsistent with this process. Additionally, no correlation exists between K/Rb and Ba/K ratios and indices of differentiation such as MgO content for the WSYP lavas, which would be present if phlogopite fractionation was important. Thus, we conclude that phlogopite was not involved in low-pressure modification of magma compositions by fractional crystallization. Moreover, it has been shown that phlogopite has a much higher partition coefficient for Rb than Ba, whereas amphibole has a much higher partition coefficient for Ba than Rb (see Green, 1994, figs 5 and 7). The relative depletion of Rb in comparison

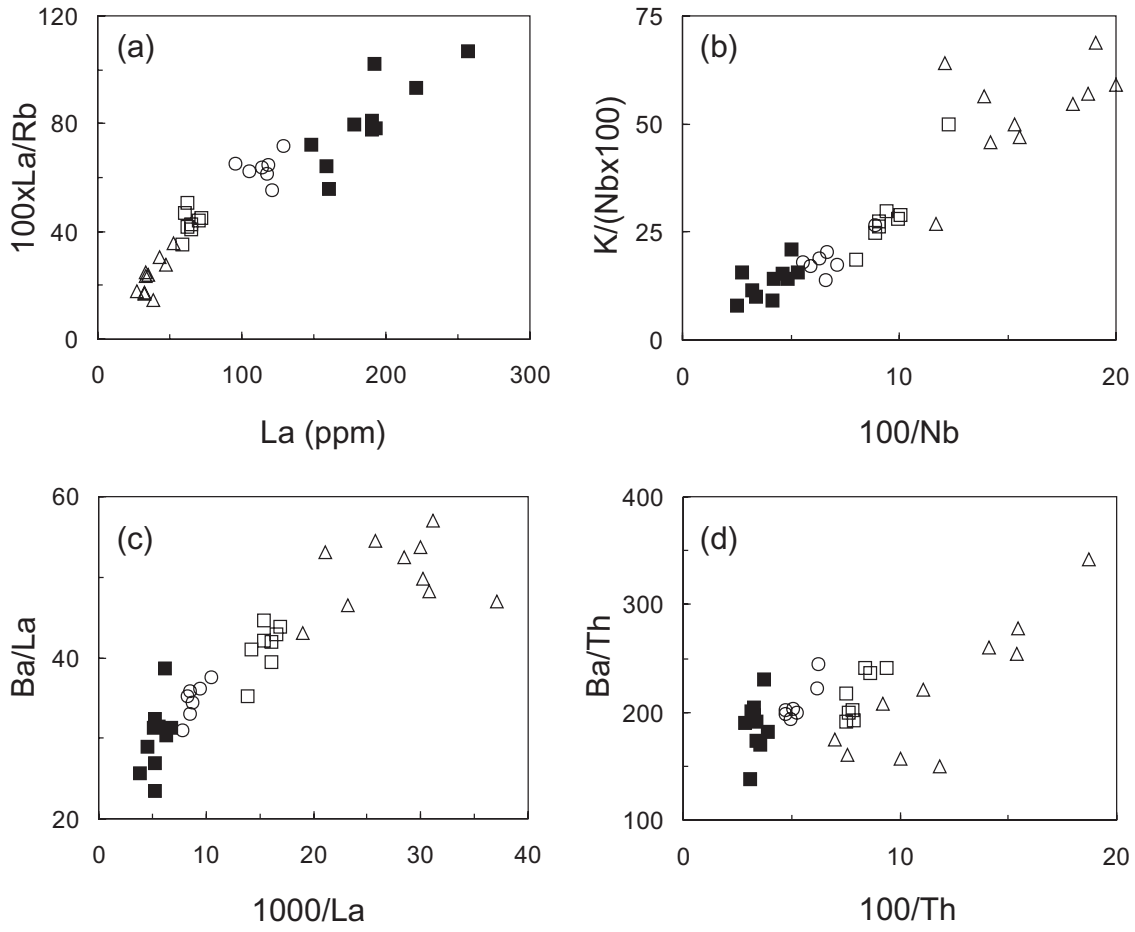

Fig. 11. (a) 100 × La/Rb vs La (ppm), (b) K/(Nb × 100) vs 100/Nb, (c) Ba/La vs 1000/La and (d) Ba/Th vs 100/Th, for the WSYP rocks. The symbols are as in Fig. 2a.

with Ba in the primitive mantle-normalized incompatible element patterns (Fig. 6) probably implies the presence of residual phlogopite during partial melting in the mantle source region rather than amphibole. The fact that the WSYP rocks have constant and relatively high Yb concentrations, and that almost all samples have Yb contents >1·8 ppm, does not support amphibole as residual mineral phase in the mantle source (Table 3). In addition, amphibole in the source region may also produce a small negative Sr anomaly (LaTourrette *et al.*, 1995); almost all of the samples show positive Sr anomalies in primitive mantle-normalized incompatible element diagrams (Fig. 6), again suggesting that there was no amphibole in the source region.

Spinel

The relatively high middle REE (MREE) and HREE abundances (Table 3) of the WSYP rocks (e.g. Yb contents, which are more than 10 times chondrite abundances) preclude garnet as a residual mineral in the mantle source region. Previous studies have shown that garnet is unstable below 2·8–3·1 GPa (depths less than about 85–95 km) (e.g. Robinson & Wood, 1998). Calculated pressures of melt segregation based on the Mg-15 normalized compositions of the samples range from 2·6 to 2·8 GPa (Table 6), suggesting that the source region is located within the spinel stablility field. Although La/Yb ratios are relatively high (Fig. 10b), Tb/Yb ratios are relatively low (Table 3), suggesting that HREE fractionation is weak, which does not support the presence of garnet in the source. Moreover, the lamprophyres in the WSYP contain spinel-bearing peridotite xenoliths (Lu & Qian, 1999; Wang *et al.*, 2001), which is consistent with the suggestion that the magmas originated within the spinel stability field.

Source region compositional features

The strongly negative Nb, Ta and Ti anomalies in the primitive mantle-normalized trace element patterns (Fig. 6) suggest that the WSYP lavas were not derived from N-MORB or ocean island balalt (OIB) source mantle. Despite their negative Ta and Nb anomalies,

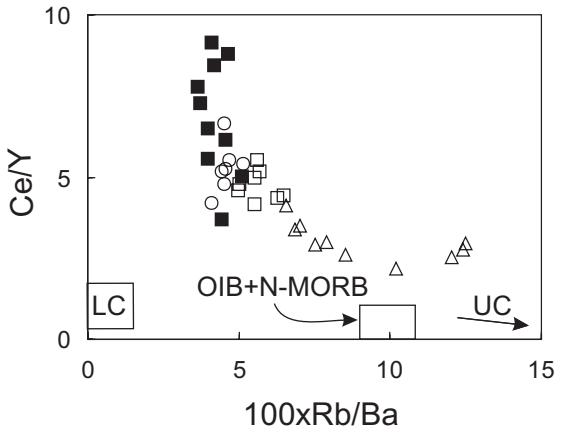

Fig. 12. Ce/Y vs 100 × Rb/Ba. The WSYP lavas are not located on mixing lines between oceanic basalts (OIB and N-MORB) and upper crust (UC) or lower crust (LC). Data sources: OIB and N-MORB from Sun & McDonough (1989); UC and LC from Taylor & McLennan (1985). The symbols are as in Fig. 2a.

the absolute contents of these elements are much higher than those typically observed in crustal rocks, and thus these features are unlikely to be attributed to significant crustal contamination. In addition, many aspects of the WSYP major and trace element characteristics, such as their high Mg values, and Ni and Cr abundances (Table 3 and Fig. 4), and the presence of mantle xenoliths, also discount the possibility of significant continental crustal contamination. There is no correlation of $^{87}Sr/^{86}Sr$ with MgO content, further precluding the possibility of crustal contamination. Likewise, the lack of a negative correlation of La, Sm, Ba, Sr or Rb with MgO (Fig. 4g–k) is also consistent with the inference of no crustal contamination. Moreover, the analysed samples do not plot on simple mixing lines between typical crustal compositions and asthenospheric magmas (Fig. 12), reducing the probability that the mantle source region of the WSYP lavas was asthenospheric mantle contaminated by crustal materials. The characteristically low Nb/La (Table 3), high $^{87}Sr/^{86}Sr$, high $^{206}Pb/^{204}Pb$, and low $^{143}Nd/^{144}Nd$ signatures (Table 4 and Fig. 9) confirm the inference based on the negative Nb–Ta–Ti anomalies (Fig. 6), that the mantle source region for the WSYP magmas was distinct from N-MORB or OIB source mantle. Hofmann (1997) has suggested that oceanic basalts (OIB and MORB) have high and relatively restricted Ce/Pb (about 25). However, the WSYP lavas are characterized by much lower Ce/Pb (1–11) ratios than mafic oceanic basalts. Residual phlogopite in the mantle source region could not cause considerable fractionation of Ce/Pb ratios in the magmas from those in the source because partition coefficients for Ce and Pb in phlogopite are 0·0007 and 0·019 (Williams *et al.*, 2004), respectively, both of which are far less than 1. If phlogopite in the source led to fractionation of Ce/Pb in the rocks, it should increase the Ce/Pb ratios in the magmas rather than decrease them. Thus, the low Ce/Pb values strongly suggest lithospheric mantle sources for the WSYP potassic rocks. On the basis of these combined major and trace element, and isotope data, we conclude that it is likely that the parental magmas were derived from enriched heterogeneous sub-continental lithospheric mantle.

Evidence for ancient subduction-related enrichment of the mantle source

The processes of partial melting of unmodified upper-mantle peridotite, subsequent crystal fractionation and significant crustal contamination cannot account for the strongly negative Nb, Ta and Ti anomalies and pronounced enrichment of incompatible elements seen in Fig. 6. Experimental data (Brenan *et al.*, 1995; Keppler, 1996) and geochemical studies (Gill, 1981; Pearce, 1982; Hawkesworth *et al.*, 1993, 1997; Turner, 2002; Turner *et al.*, 2003) suggest that island arc magmas are characterized by significant enrichment in LILE relative to HFSE and strongly negative Nb, Ta and Ti anomalies in primitive mantle-normalized incompatible element diagrams. However, the WSYP lavas are spatially remote from contemporaneous subduction zones. This makes coeval oceanic plate subduction an unlikely origin for these anomalies. The most plausible explanation for these observations is that the anomalies are the signatures of an enriched fluid and/or melt, which metasomatized the sub-continental lithospheric mantle beneath the western part of the Yangtze craton prior to the partial melting event that produced the WSYP potassic magmas. It is possible that such metasomatic components may be derived from an enrichment event that has no relationship to plate subduction and that the Nb–Ta–Ti anomalies are the result of the stability of residual titanate minerals (Haggerty, 1989; Foley & Wheller, 1990). However, this process could not account for the well-defined spatial compositional trends exhibited by the WSYP magmas because the metasomatic melts and/or fluids would probably be more randomly distributed within the upper mantle. We therefore suggest that the metasomatic components were derived from partial melting of a mantle wedge modified by fluids and/or melts derived from an earlier subduction zone (Rowell & Edgar, 1983; Venturelli *et al.*, 1984; Mitchell & Bergman, 1991).

Although apatite in the mantle source region (see below) may fractionate the U/Pb ratio, low U/Pb ratios are unlikely to have been produced by partial melting or crystal fractionation, because of the similar geochemical behaviour of U and Pb in magmatic processes (Foley & Wheller, 1990; Sheppard & Taylor, 1992) and subduction-derived fluids (Turner *et al.*, 1996, 1997; Turner, 2002). Thus, the variable and relatively low U/Pb ratios in the WSYP rocks, which are broadly consistent with

those of modern pelagic oceanic sediments (Sun, 1980; Thompson *et al.*, 1984; Sun & McDonough, 1989), probably suggest both the contribution of sedimentary components in the petrogenesis of the WSYP rocks and fractionation of the U/Pb ratio by residual apatite in the source. In addition, the normalized incompatible element patterns in the high LILE/LREE ratio subgroup (e.g. Xiangyun rocks, Janchuan lamprophyres) resemble those of arc magmas (Fig. 6a). Although the actual abundances of incompatible elements are much higher in the low LILE/LREE ratio subgroup (i.e. Yanyuan potassic rocks, Xichang rocks) than in typical subduction-related basalts, their normalized incompatible element patterns mimic inter-element ratios that are broadly similar to those of magmas associated with active subduction zones (Fig. 6d), indicating a likely petrogenetic relationship of the low LILE/LREE ratio subgroup with subduction processes. Likewise, their Pb isotopic compositions overlap with those of pelagic oceanic sediments (Sun, 1980; Plank & Langmuir, 1998), also probably suggesting a subduction-related origin (Fig. 9). Their occurrence at the margin of the Archaean Yangtze craton (Fig. 1) and the characteristics of relative depletion in Na and Al and enrichment in LILE (Figs 4a, d and 6) are consistent with derivation from a previously subduction-modified lithospheric mantle source as suggested by Mitchell & Bergman (1991). The source region enrichment suggested by the Sr–Nd–Pb isotopic compositions (Fig. 9) is also consistent with palaeo-subduction. The estimates of melt segregation depths in the various localities along the traverse (Fig. 1) are also consistent with the presence of an ancient subduction zone beneath the western part of Yangtze craton (Fig. 10a).

Factors responsible for the compositional zonation of the magmas away from the margin of the craton

The characteristics of compositional zonation of subduction-related igneous rocks across an island arc have been studied in many localities (Dickinson & Hatherton, 1975; Woodhead & Johnson, 1993; Ryan *et al.*, 1995; Hoogewerff *et al.*, 1997; Elburg *et al.*, 2002). The origin of this phenomenon is different in different island arcs. However, previous studies have shown that there are two factors responsible for the compositional zonation: source region geochemical composition and petrogenetic process (or source contribution to magma generation) (Hawkesworth *et al.*, 1993; Ryan *et al.*, 1995; Hochstaedter *et al.*, 2000; Walker *et al.*, 2000; Elburg *et al.*, 2002).

Source region composition

The supra-subduction zone mantle wedge, modified by slab-derived melts or fluids, is considered to be the source region for arc magmas (Pearce & Parkinson, 1993; Pearce & Peate, 1994). It has been shown that different degrees of source depletion are a controlling parameter in the compositional zonation of arc volcanic rocks (Hochstaedter *et al.*, 1996, 2000). The presence of refractory lithospheric mantle beneath the western margin of the Yangtze craton implies that the composition of the mantle source of the WSYP potassic magmas prior to modification by subduction-related components was probably close to MORB-source mantle rather than OIB source. The positive correlation between Nb and La (Fig. 13) suggests that Nb behaves completely incompatibly in the WSYP suite of rocks, despite the possible presence of residual phases such as rutile and titanite in the mantle source region (see below). Pearce & Parkinson (1993) proposed that a plot of the incompatible element Nb vs Yb may be used to determine the degree of partial melting and extent of depletion of the mantle source of subduction-related magmatic rocks (Fig. 14). Although the presence of residual rutile or titanite in the mantle source of the WSYP rocks makes it unwise to use Nb as an index of the degree of partial melting, we nevertheless consider the approach useful to determine the relative fertility of the mantle source. The WSYP samples plot close to the trend of partial melting of a fertile MORB mantle (FMM) source (the global convecting upper-mantle reservoir from which N-type MORB is derived; Pearce & Parkinson, 1993). This shows that the mantle source region beneath the western part of the craton, prior to the addition of subduction-derived fluids or melts, is likely to have been similar to the N-MORB source. Moreover, the trend of the WSYP lavas, which is nearly parallel to the FMM melting trend (Fig. 14), suggests that the fertility of the mantle source before the subduction-related component was introduced was

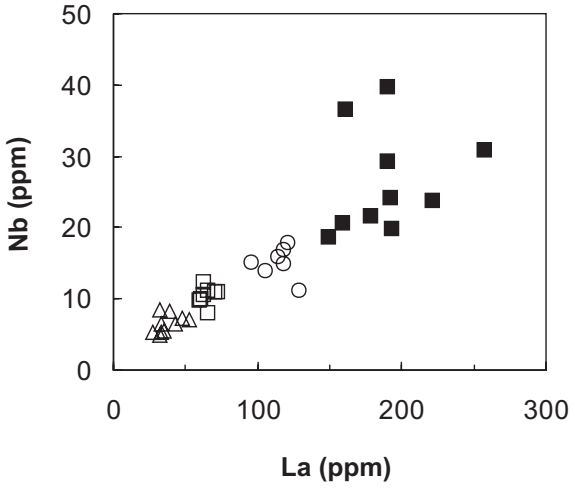

Fig. 13. Nb (ppm) vs La (ppm). Broadly positive correlation between Nb and La shows that Nb, which behaves like La, is an incompatible trace element in this suite of the rocks. The symbols are as in Fig. 2a.

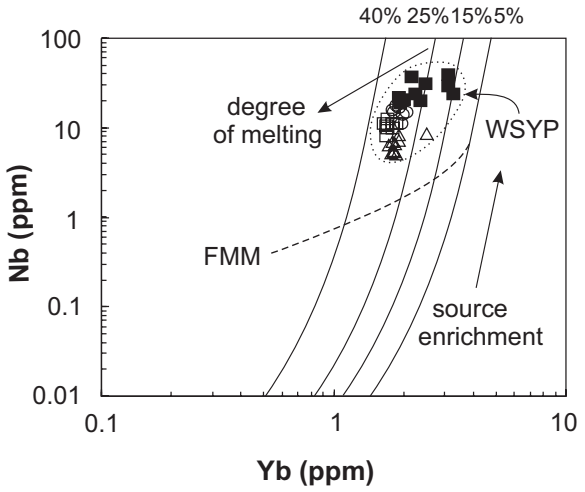

Fig. 14. Nb (ppm) vs Yb (ppm) diagram to describe source depletion trends and resolve partial melting trends in subduction-related volcanic rocks (Pearce & Parkinson, 1993). The WSYP magmas show a subparallel trend to FMM (fertile MORB mantle), probably indicating a similar fertility of the mantle source of the WSYP magmas from NE to SW along the traverse (Fig. 1). FMM is equivalent to the N-MORB source (Pearce & Parkinson, 1993). Continuous curves labelled with numbers in percent (i.e. 5%, 15%, 25%, 40%) represent degrees of mantle partial melting. Arrows labelled with degree of melting and source enrichment represent the mantle partial melting and source enrichment trends, respectively. The symbols are as in Fig. 2a.

similar from SW to NE along the traverse (Fig. 1), although slightly less enrichment of the mantle source is indicated for some rocks aligned with the ASRR shear zone relative to the other samples. Thus, a significant influence of variable extent of source depletion on the compositional zonation in the WSYP rocks may be ruled out.

Previous studies have shown that subduction-related metasomatic components can be broadly classified into two groups: (1) fluids, derived from dehydration of either altered oceanic crust (Tatsumi *et al.*, 1986; Hawkesworth *et al.*, 1993, 1997; Turner *et al.*, 1996, 1997; Turner, 2002) or subducted sediments (Ryan *et al.*, 1995; Class *et al.*, 2000; Elburg *et al.*, 2002); (2) partial melts of subducted sediment or the oceanic crust itself (Hawkesworth *et al.*, 1993, 1997; Vroon *et al.*, 1993; Elliott *et al.*, 1997; Elburg *et al.*, 2002). Important geochemical distinctions can be recognized between arc volcanic rocks in which the magma sources are modified by a subduction-derived fluid and those that are enriched by subducted sediment or partial melt (Hawkesworth *et al.*, 1997; Elburg *et al.*, 2002). It has been shown that some LILE (e.g. Rb, Ba, Sr, U and Pb) are mobile in an aqueous fluid because these elements are water-soluble; however, the REE and HFSE (e.g. Ce, Th, Nb, Zr and Ta) are less mobile or immobile in a fluid phase because they are relatively water-insoluble trace elements (Sheppard & Taylor, 1992; Turner *et al.*, 1996, 1997; Elburg *et al.*, 2002; Turner, 2002). This characteristic leads to high concentrations of some water-soluble LILE and other fluid-mobile elements (e.g. Rb, Ba, U and Pb), and very low contents of HFSE in the subduction-derived fluid, which could be introduced into the overlying mantle wedge. Thus, those volcanic rocks whose source was strongly metasomatized by a fluid component are likely to have higher Pb/Ce (>0·1; Elburg *et al.*, 2002), Ba/Th (>170; Hawkesworth *et al.*, 1997), Sr/Ce and Ba/La ratios than rocks whose source was enriched by partial melts of oceanic crust and subducted sediments (Sheppard & Taylor, 1992; Elburg *et al.*, 2002). In contrast, arc volcanics with a strong imprint of a subduction-related partial melt or subducted sediment in their source region have higher Th/Ce (>0·15; Hawkesworth *et al.*, 1997) and Nb/Zr (>0·05; Vroon *et al.*, 1993; Elburg *et al.*, 2002) ratios and lower Sr/Ce and Ba/La ratios (Sheppard & Taylor, 1992) than those related to fluid metasomatism of their mantle source. Both fluid- and melt- (or subducted sediment) induced metasomatism could account for the negative Nb–Ta–Ti anomalies of the studied lamprophyres.

The Pb/Ce ratios of almost all samples are >0·1, and the highest is 0·78 (Fig. 8a); only one sample has a Pb/Ce ratio <0·1 (Fig. 8a). The Ba/Th ratios of all WSYP rocks are >170 except for sample CH9716 (140) (Fig. 8a). Moreover, the WSYP samples have high Rb/Nb and Sr/Zr ratios (Fig. 8b); in addition, almost all rocks display low Th/Ce (<0·15) and low Nb/Zr (<0·05) ratios (Fig. 8c). All these characteristics suggest that the WSYP rocks were derived from a mantle source that had been strongly modified by a subduction-related fluid, rather than a subducted sediment or partial melt (Fig. 8). The distinctly high Pb/Ce and Ba/Th (Fig. 8a), and considerably low Th/Ce and Nb/Zr (Fig. 8c) ratios of the WSYP rocks appear to indicate that these rocks were derived from a part of the lithospheric mantle strongly modified by subduction-related fluids. In other words, the source materials consist of two components: depleted mantle and subduction-derived fluid. The overall linear arrays in Sr–Nd–Pb isotope space (Fig. 9) support a two-component mixing model. Moreover, there are systematic changes in incompatible trace element ratios in the WSYP samples with distance from the western margin of the Yangtze craton, which probably indicate changes in the amount of fluid added to the lithosphere. For example, the lavas in the high LILE/LREE ratio subgroup, the closest to the western boundary of the Yangtze craton (Fig. 1), have the highest ratios of fluid-mobile elements to less fluid-mobile (or fluid-immobile) elements (e.g. Ba/La, Sr/Ce, Pb/Ce, Ba/Nb, Rb/Nb, Sr/Zr and Ba/Th; Figs 7 and 8). This suggests that the lithospheric mantle beneath the western boundary of the Yangtze craton (SW end in the traverse; Fig. 1) underwent the strongest enrichment event prior to partial melting because large amounts of subduction-derived fluid were imported into the overlying lithospheric mantle. In contrast, the rocks in

the low LILE/LREE ratio subgroup, erupted at the NE end of the traverse (Figs 1 and 7), have the lowest ratios of fluid-mobile elements to less fluid-mobile (or fluid-immobile) elements (e.g. Ba/La, Sr/Ce, Pb/Ce, Ba/Nb, Rb/Nb, Sr/Zr and Ba/Th; Figs 7 and 8). This indicates that the lithospheric mantle beneath the more interior parts of the Yangtze craton (at the NE end in the traverse; Fig. 1) suffered the weakest enrichment event prior to partial melting because the smallest amount of subduction-derived fluid was introduced into the overlying lithospheric mantle. The intermediate LILE/LREE ratio subgroup, located between the high and low LILE/LREE subgroup, has intermediate ratios of fluid-mobile elements to less fluid-mobile (or fluid-immobile) elements (e.g. Ba/La, Sr/Ce, Pb/Ce, Ba/Nb, Rb/Nb, Sr/Zr and Ba/Th; Figs 7 and 8). This shows that the lithospheric mantle beneath the intermediate area of the traverse (Fig. 1) underwent moderate enrichment prior to partial melting because intermediate amounts of subduction-derived fluid were infiltrated into the overlying lithospheric mantle in this area. Thus, these systematic decreases in incompatible element ratios from the western margin to the interior of the Yangtze craton (Figs 7 and 8) probably reflect a steady decline in the amount of subduction-derived metasomatic fluid introduced into the overlying mantle wedge. In addition, the overlap between the high LILE/LREE ratio subgroup of the WSYP rocks and those of GLOSS in the Sr–Nd–Pb isotope diagrams (Fig. 9) supports the inference that there is an increase in the amount of the subduction-derived fluid from the low LILE/LREE subgroup (at the NE end of the traverse) to the high LILE/LREE subgroup (at the SW end of the traverse) (Fig. 1).

Two important features can be recognized in Fig. 8. (1) The ratios of fluid-mobile trace elements to fluid-less-mobile trace elements (e.g. Pb/Ce, Ba/Th, Rb/Nb; Fig. 8a and b) are obviously different from those of MORB and OIB (Dosso *et al.*, 1988; Sun & McDonough, 1989; GERM website: http://earthref.org/GERM/), whereas the fluid-immobile trace element ratios (e.g. Nb/Zr, Hf/Ta; Fig. 8c and d) are close to those of N-MORB and are significantly different from OIB. Recent studies have shown that the Indian MORB source is distinct from the Pacific and Atlantic MORB sources in terms of its trace element and isotope composition (Rehkämper & Hofmann, 1997; Peate *et al.*, 2001). The fluid-immobile trace element ratios of the WSYP lavas are similar to those of the Indian MORB source (GERM website: http://earthref.org/GERM/) (Fig. 8). This fact not only indicates that the metasomatic component originates from subduction-derived fluids, but also suggests that the elemental characteristics of the mantle wedge prior to modification by the subduction-derived fluids were close to Indian MORB-source mantle rather than OIB source. (2) The magmatic rocks located at the SW end of the traverse (Fig. 1), derived from a lithospheric mantle source strongly modified by subduction-related fluids (i.e. with relatively large amounts of fluid added), show considerably different trace element ratios from those of MORB. Those located at the NE end of the traverse, derived from a part of the lithospheric mantle relatively weakly modified by the subduction-related fluids (i.e. with relatively small amounts of fluid added), show similar trace element ratios to MORB (Fig. 8a and b). These characteristics suggest that the metasomatic component is derived from a subduction-related fluid rather than a melt.

The combination of Ba/Th and $^{87}Sr/^{86}Sr$ ratios has been effectively used as a fingerprint in further identifying the derivation of subduction-related fluids (Turner *et al.*, 1997). The WSYP lavas form a linear trend in a plot of Ba/Th vs $(^{87}Sr/^{86}Sr)_i$ (Fig. 15a), which probably suggests simple two-component mixing. One end-member has a composition similar to Indian MORB (Rehkämper & Hofmann, 1997) with low Ba/Th and low $^{87}Sr/^{86}Sr$ ratios. The other end-member component has similar $^{87}Sr/^{86}Sr$ ratios to, and higher Ba/Th than, marine sediments (Plank & Langmuir, 1998). This suggests that the second end-member is probably derived from marine sediments. The higher Ba/Th ratio of this end-member compared with that of marine sediments shows that the sediment contribution is not added by bulk mixing and/or partial melting of subducted sediments, because Ba and Th have broadly similar incompatibility and thus Ba/Th fractionation should be negligible during partial melting of the mantle wedge. Previous studies showed that a subduction-derived fluid, which may exhibit decoupling of the geochemical behaviour of Ba and Th, has higher Ba/Th ratios than bulk sediments and/or partial melts thereof because Ba is highly mobile and Th is immobile in an aqueous fluid (Turner *et al.*, 1996, 1997; Peate *et al.*, 2001). Thus, we infer that the second end-member is a fluid derived dominantly by dehydration of the subducted marine sediments.

Petrogenetic processes

The positive correlation between La/Yb and La suggests that partial melting is the dominant process in the petrogenesis of the WSYP magmas (Fig. 10b); crustal contamination and crystal fractionation probably also played a role (Fig. 4). La/Yb ratios show a decreasing trend from the interior to the western margin of the craton (Fig. 10b), which could reflect an increase in the degree of partial melting in the mantle source region from east to west. This observation is also supported by the observation that LILE and LREE abundances (Fig. 6), and LREE/HREE ratios (Figs 3 and 7) steadily decrease from the interior to the western margin of the craton. This is consistent with an increase in the thickness of the overlying

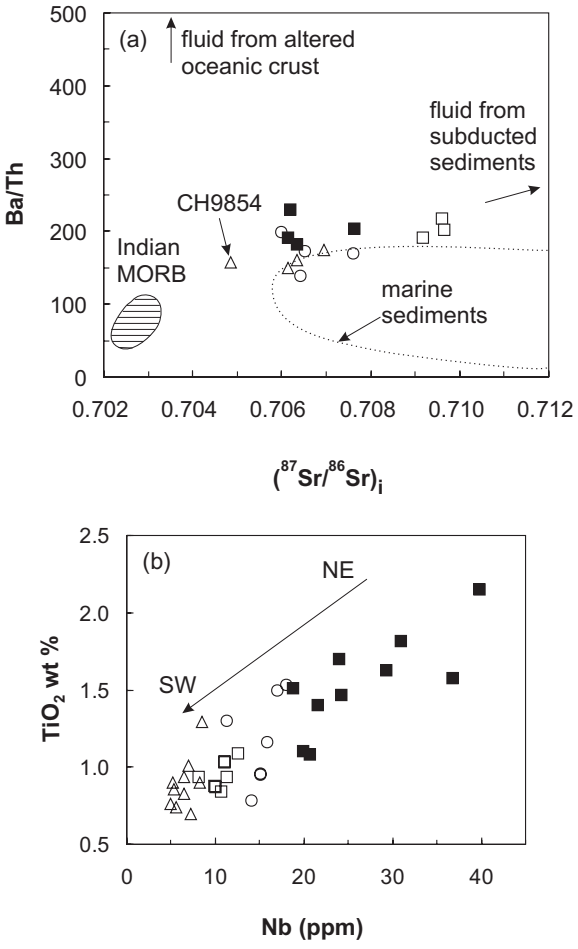

Fig. 15. (a) Ba/Th vs $(^{87}Sr/^{86}Sr)_i$ showing that the WSYP magmatic rocks are characterized by high $(^{87}Sr/^{86}Sr)_i$ and high Ba/Th. Overlapping of $^{87}Sr/^{86}Sr$ ratios between marine sediments and the WSYP lavas suggests the involvement of a fluid dominantly derived from subducted sediments in the metasomatism of the mantle source of the WSYP lavas (see text). The relatively high Ba/Th in the WSYP lavas compared with marine sediments suggests that Ba was strongly mobile relative to Th in the fluid. The WSYP lavas show a broadly linear array, probably suggesting a simple two end-member mixing. The WSYP samples are located between a fluid derived from dehydration of marine sediments and Indian MORB source mantle, suggesting that the two mixing end-members are Indian MORB mantle and fluid derived from dehydration of marine sediments (for more detailed discussion see text). The composition of the fluid derived from subducted altered oceanic crust is from Turner *et al.* (1997). Data for Indian MORB and marine sediments are from Rehkämper & Hofmann (1997) and Plank & Langmuir (1998), respectively. The symbols are as in Fig. 2a. (b) Variation of TiO_2 (wt %) vs Nb (ppm). The meaning of NE, SW and the arrow is as in Fig. 7. The symbols are as in Fig. 2a.

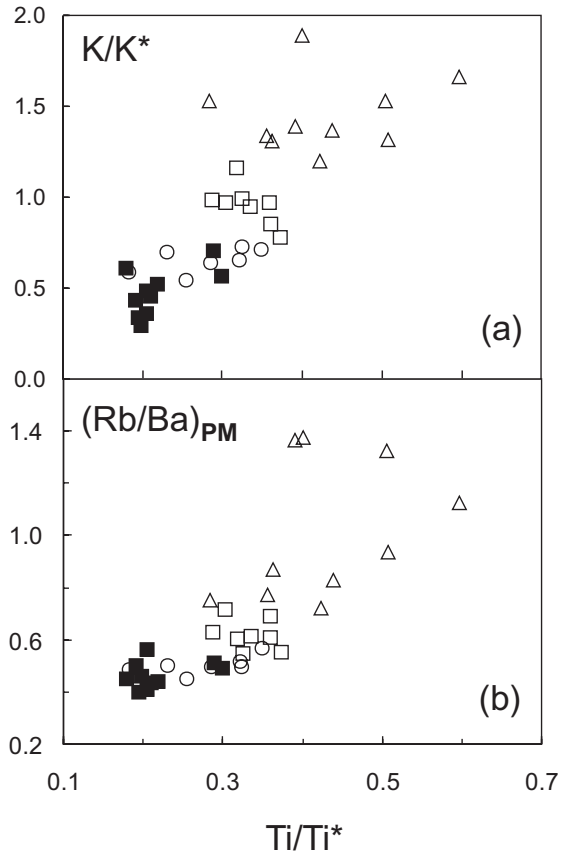

Fig. 16. (a) K/K* vs Ti/Ti*. (b) $(Rb/Ba)_{PM}$ vs Ti/Ti*. Positive correlations of K/K* (a) and $(Rb/Ba)_{PM}$ (b) with Ti/Ti* suggest that phlogopite in the mantle source region has an effect on the Ti budget in the rocks [for the meaning of K/K*, Ti/Ti* and $(Rb/Ba)_{PM}$ see text]. The symbols are as in Fig. 2a.

lithosphere from the western margin to the interior of the Yangtze craton (Liu, 1999; Zhong *et al.*, 2000).

Correlated variations between the trace elements Nb and Ti (Fig. 15b) suggest that Ti-rich residual mineral phases in the source region of the WSYP magmas may control the HFSE abundances. The relatively flat correlation of TiO_2 vs MgO for all samples (Fig. 4c) suggests that there might be residual Ti-bearing phases buffering TiO_2 contents. However, no correlations exist between Ti/Ti*, Nb/Nb*, Ta/Ta*, Nb/Ta and MgO in the studied samples (not shown), suggesting that there is no fractionation of Ti-bearing phases (Ti*, Nb* and Ta* are the expected concentrations of Ti, Nb and Ta respectively, assuming no anomaly of Ti, Ta, and Nb in the mantle-normalized incompatible element diagram shown in Fig. 6; Ti/Ti* refers to ratio of the concentration of the mantle-normalized element Ti in the rocks to that of Ti*, and similarly for Nb/Nb* and Ta/Ta*). Nevertheless, there are broad positive correlations between K/K* and $(Rb/Ba)_{PM}$ vs Ti/Ti* in the WSYP rocks (Fig. 16), suggesting the possibility that residual phlogopite in the mantle source region may also influence the Ti budget in the magmatic rocks (PM in the subscript represents the primitive mantle-normalized value). The residual Ti-bearing phases, together with phlogopite and apatite (see below), were probably the result of the lithospheric mantle beneath the western part of the Yangtze craton being modified and enriched by subduction-related fluids

(Foley & Wheller, 1990; Sheppard & Taylor, 1992; Elburg *et al.*, 2002). It has been shown that rutile and titanite have high partition coefficients for the elements Nb, Ta and Ti (Green, 1994; Foley *et al.*, 2000; Green *et al.*, 2000). They may retain these HFSE during progressive mantle partial melting and this leads to the strong depletion of these elements in the resultant magmas (Foley & Wheller, 1990; Sheppard & Taylor, 1992; Pearce & Parkinson, 1993; Pearce & Peate, 1994). The presence of strong negative Nb–Ta–Ti anomalies in the mantle-normalized trace element patterns of all of the samples studied here (Fig. 6) probably indicates that the mineral phases rutile (TiO_2) and/or titanite ($CaTiSiO_5$) were stable in the mantle source region during the generation of the WSYP magmas. Rutile has a higher partition coefficient for the element Nb (136) than Ta (16·6), and titanite shows a higher partition coefficient for the element Ta (142) than Nb (4·6) (http://www.earthref.org). The magmatic rocks located along the ASRR shear zone exhibit depletions in Nb that are stronger than those of Ta in the mantle-normalized trace element patterns (Fig. 6a), which probably suggests that rutile is the dominant residual mineral phase in the mantle source. However, almost all the samples located at the NE end of the traverse show greater depletions of Ta than Nb in the mantle-normalized trace element patterns (Fig. 6d), suggesting that in the NE titanite may be the dominant residual mineral phase in the mantle source. Almost of all rocks located in the middle part of the traverse show similar depletions of Ta and Nb (Fig. 6b and c), which might be well explained by near-equal proportions of titanite and rutile in the mantle source region. This is further confirmed by the correlation between $(Nb/Ta)_{PM}$ and La/Yb (Fig. 17f), which suggests a broadly decreasing trend in $(Nb/Ta)_{PM}$ ratios with decreasing La/Yb. In detail, most of the rocks in the northeastern part of the traverse have $(Nb/Ta)_{PM}$ ratios $>1{\cdot}0$, suggesting that titanite is more important than rutile in terms of retaining the HFSE in the mantle source region; however, almost all of the samples in the southwestern part of the traverse have $(Nb/Ta)_{PM}$ ratios $<1{\cdot}0$, which suggests that here rutile is more important than titanite in retaining the HFSE in the source because of the differences in partition coefficients for Nb and Ta in rutile and titanite. The inference is that the influence of residual rutile on Nb and Ta contents in the rocks becomes progressively stronger than that of titanite with increasing degree of partial melting. In other words, titanite retaining the HFSE in the source dominantly occurs during the earlier stages of partial melting, whereas rutile retaining the HFSE mostly occurs in the later stages of partial melting. Moreover, this may also explain the broadly segmented trends in Nb/Nb* and Ta/Ta* vs La/Yb (Fig. 17d and e). Inflections occur at La/Yb ratios of ~65. Increasing degrees of partial melting result in increasing Nb/Nb* and Ta/Ta* when La/Yb ratios are more than ~65; both ratios subsequently decrease when La/Yb ratios are less than ~65. The inflections could be interpreted to mark a change in proportions of rutile and titanite in the source. Titanite is inferred to preferentially enter the melt during the early stages of partial melting (corresponding to La/Yb more than ~65) which causes Nb/Nb* and Ta/Ta* to increase in the melt with increases in degree of partial melting (Fig. 17d and e). The slope of increasing Ta/Ta* (Fig. 17e) with decreasing La/Yb (for La/Yb $>$ ~65) is steeper than that of Nb/Nb* (Fig. 17d) probably because titanite has a higher partition coefficient for Ta than that for Nb. However, rutile appears to remain in the solid residue retaining the HFSE during higher degrees of partial melting (La/Yb less than ~65), which causes Nb/Nb* and Ta/Ta* to decrease in the melt with decreasing La/Yb (Fig. 17d and e). The decreasing slope of Ta/Ta* with decreasing La/Yb (for La/Yb $<$ ~65) (Fig. 17e) is flatter than that of Nb/Nb* (Fig. 17d) probably because rutile has a higher partition coefficient for Nb than for Ta. Unlike Nb/Nb* and Ta/Ta*, Ti/Ti* ratios show a progressively increasing trend with increasing degree of partial melting (Fig. 17c), which can be ascribed to progressively increasing amounts of phlogopite entering the melt. Sample CH9723 has the highest Ta/Ta* and Nb/Nb* among the WSYP rocks (Fig. 17d and e), which possibly indicates the highest proportion of titanite in the source entering the melt during partial melting.

No correlation exists between P/P* and Sr/Sr* ratios and indices of differentiation such as MgO content for the WSYP rocks, which would be present if apatite fractionation was important. Thus, apatite was not involved in fractional crystallization. Because there are negative anomalies of P and Sr in the mantle-normalized incompatible element diagrams (Fig. 6), together with similar variation trends in P/P* and Sr/Sr* with increasing degree of partial melting (Fig. 17g and h), these are likely to reflect the presence of apatite in the mantle source region. The transition from negative to positive anomalies of P and Sr in the mantle-normalized trace element patterns of the rocks from NE to SW along the traverse (Fig. 6) probably suggests that the abundance of residual apatite decreases in the source region from the interior to the western margin of the craton. This is consistent with the gradual increases in P/P* and Sr/Sr* in the rocks from NE to SW along the traverse with increasing degree of partial melting (Fig. 17g and h), suggesting that apatite in the source preferentially enters the melt during the partial melting process. Sample CH7F002 (Fig. 17g and h) has higher ratios of P/P* and lower ratios of Sr/Sr* than other rocks in the subgroup with relatively high LILE/LREE ratios. This suggests that the apatite in the source of the sample may have a relatively low Sr content.

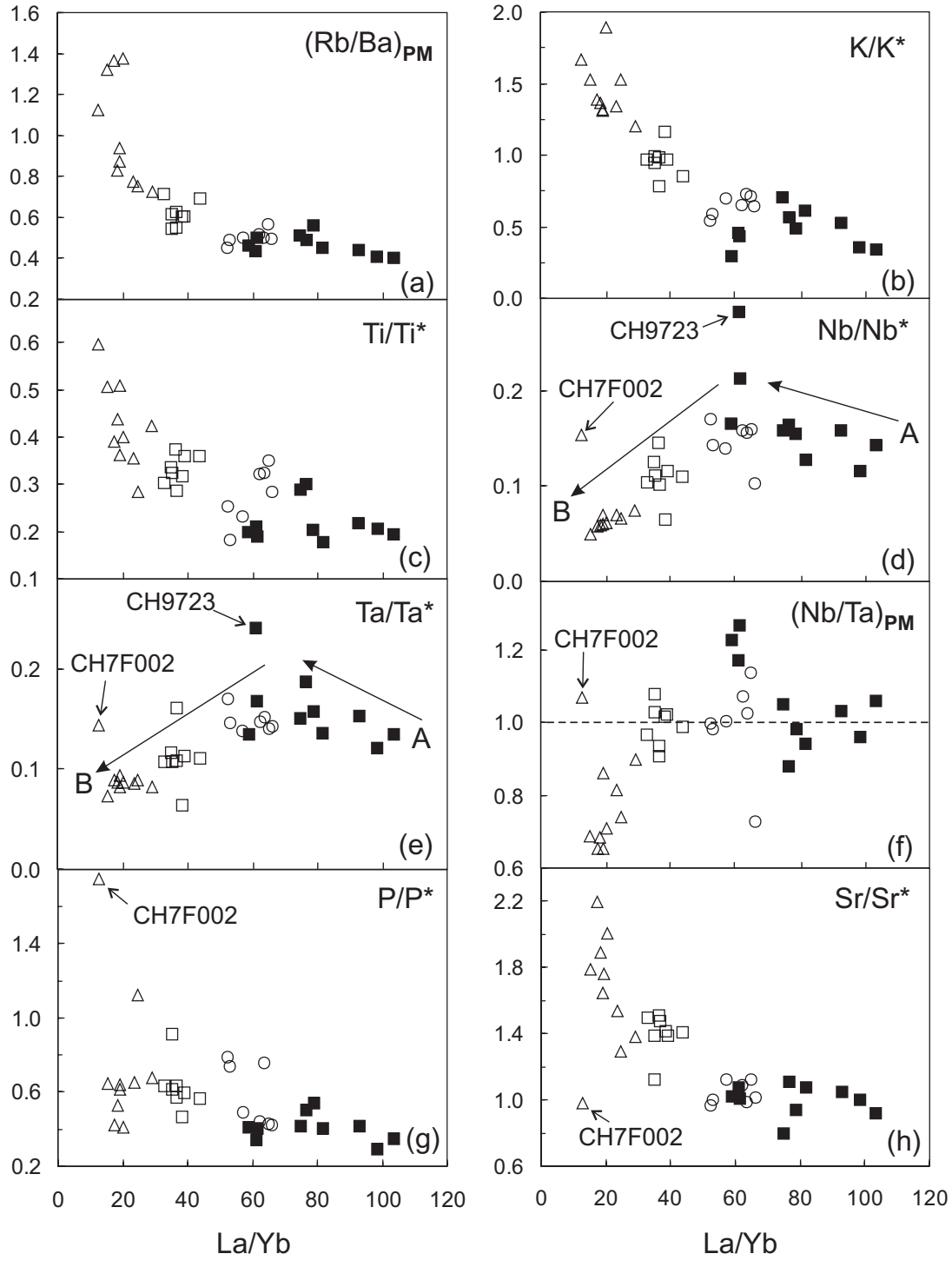

Fig. 17. (a) $(Rb/Ba)_{PM}$ vs La/Yb. (b) K/K* vs La/Yb. (c) Ti/Ti* vs La/Yb. (d) Nb/Nb* vs La/Yb. (e) Ta/Ta* vs La/Yb. (f) $(Nb/Ta)_{PM}$ vs La/Yb. (g) P/P* vs La/Yb. (h) Sr/Sr* vs La/Yb. Negative correlations of $(Rb/Ba)_{PM}$ (a) and K/K* (b) with La/Yb suggest that the content of phlogopite in the mantle source region gradually decreases with increasing degree of partial melting. Inflections in the variation trends of Nb/Nb* (d) and Ta/Ta* (e) against La/Yb, together with decreasing $(Nb/Ta)_{PM}$ with decrease of La/Yb (f), suggest that both titanite and rutile occur in the mantle source region. Broadly negative correlations of P/P* (g) and Sr/Sr* (h) against La/Yb indicate that the abundance of apatite in the source decreases with increase in the degree of the partial melting (for more detailed interpretation see text). The symbols are as in Fig. 2a. Arrows labelled 'A' denote the increasing trends of Nb/Nb* (d) and Ta/Ta* (e) with decreasing La/Yb. However, arrows labelled 'B' refer to the decreasing trends of Nb/Nb* (d) and Ta/Ta* (e) with decreasing La/Yb. Dashed line in (f) indicates the primitive mantle-normalized Nb/Ta ratio (i.e. 1·0).

It has been shown that fractionation of incompatible elements during partial melting could occur if mineral phases that retain them are residual in the source region at low degrees of melting (Wilson, 1989). The increase in Rb/Ba ratio, shown by the gradually flattening slope of the Rb–Ba segment, in the primitive mantle-normalized incompatible element patterns from the interior to the western margin of the craton (Fig. 6) could be attributed to a decrease in the extent to which Rb is retained by residual phlogopite in the mantle source. This indicates a decrease in the amount of residual phlogopite in the source from the interior to the western margin of the Yangtze craton, probably caused by an increase in the degree of partial melting. Additionally, increasing trends in K/K^* and $(Rb/Ba)_{PM}$ in the rocks with increasing degree of the partial melting (Fig. 17a and b) also suggest that phlogopite in the source preferentially enters the melt during mantle partial melting. In the next section the trace element compositions of the WSYP rocks are modelled to quantitatively evaluate the influence of the degree of mantle partial melting, and the amount of the subduction-derived fluid involved in the metasomatism of the lithosphere, on the observed compositional zonation with distance from the western boundary of the Yangtze craton.

Trace element modelling

As discussed above, the first-order controlling factors on the compositional zonation of the WSYP magmas are the degree of partial melting and the amount of subduction-derived fluid added to the mantle source. An increase in the amount of fluid added to the mantle wedge correlates with an increase in the degree of partial melting of the lithospheric mantle from the interior to the western margin of the Yangtze craton (Fig. 1). This increased fluid component would effectively reduce the initial melting temperature of the sub-continental lithospheric mantle. Based on these conclusions, we have developed a mixing and partial melting model for trace elements to simulate the generation of the WSYP magmas. To quantitatively reveal the relative roles of both the degree of partial melting and the amount of fluid involved, together with a minimization of the potential effects of fractional crystallization on the compositional zonation of the magmas, we selected the incompatible trace element ratios La/Yb and Ba/Nb as the simulated calculation parameters; these are thought to be indicative of partial melting degree and the amount of fluid, respectively (Barragan *et al.*, 1998). In addition, both La/Yb and Ba/Nb ratios are not significantly changed by small amounts of fractional crystallization of olivine and clinopyroxene, which probably occurred in the generation of the WSYP magmas. Our model assumes that the WSYP magmas were generated through two steps: (1) mixing of a depleted mantle component and subduction-derived fluid; (2) partial melting of the resultant enriched mantle (i.e. the mixed source material) and the generation of the WSYP melts. This model mimics the magma generation process based on an iterative calculation of two variables: the partial melting degree and the amount of added fluid. We used both modal and non-modal batch partial melting models and assumed MORB (i.e. N-MORB; Sun & McDonough, 1989) source mantle as the source material (for a detailed discussion of the appropriateness of using N-MORB-source instead of Indian MORB-source mantle, see Appendix B). MORB-source mantle is assumed to have 0·1 times N-MORB (Sun & McDonough, 1989) concentrations of trace elements, based on an assumption (Wilson, 1989) that MORB magmas are results of ~10% partial melting of N-MORB mantle source (i.e. Ba 0·63 ppm, La 0·25 ppm, Nb 0·23 ppm, Yb 0·31 ppm). Previous studies (e.g. Stolper & Newman, 1994; Stein *et al.*, 1997; Bizimis *et al.*, 2000; Tatsumi & Hanyu, 2003) showed that the concentrations of Ba, La, Nb and Yb in the subduction-derived fluid vary significantly. We select fluid (A) and fluid (B) to represent a subduction-derived fluid with higher contents of Ba, La, Nb and Yb and a fluid with lower contents of these elements, respectively. The concentrations of Ba, La, Nb and Yb in fluid (A) and fluid (B) are shown in Table 7. On the basis of the above data, the initial composition of the metasomatized mantle source with different proportions of fluid can be calculated and is given in Table 7. The resultant minerals and their proportions in the mantle source region after introduction of the fluid are olivine (60%), orthopyroxene (25%), clinopyroxene (8%), spinel (2%), phlogopite (2%), titanite (2%), rutile (0·5%) and apatite (0·5%). The partition coefficients for Ba, La, Nb and Yb in these mineral phases are based on those from the GERM website (http://earthref.org/GERM/); the data are included in Appendix B. The calculated results (Table 8) for the modal batch partial melting model calculated with the concentrations of Ba, La, Nb and Yb in fluid (A) suggest that the degree of mantle partial melting ranges from 1% to >40% and that the proportion of subduction-derived fluid added ranges from 0·1% to 2% from the interior (at the NE end of the traverse) to the western margin (at the SW end of the traverse) of the Yangtze craton (Fig. 18a). In detail, subgroups with low (at the NE end of the traverse), intermediate and high (at the SW end of the traverse) LILE/LREE ratios are indicative of 1–5%, 5–20% and 20–>40% of mantle partial melting, which corresponds to 0·1–0·4%, 0·3–1·0% and 1·0–2·0% subduction-derived fluid introduced into the mantle wedge, respectively. For the modal batch partial melting model calculated with the concentrations of Ba, La, Nb and Yb in fluid (B), the calculated results (Table 8) suggest that the degree of mantle partial melting ranges from 0·7% to >40% and that the proportion of subduction-derived

Table 7: Composition of metasomatized mantle source (Co: ppm)

	Ba	Nb	La	Yb
Proportion of fluid (A)				
0%	0·63	0·23	0·25	0·31
0·10%	3·39	0·23	0·35	0·30
0·30%	8·91	0·23	0·55	0·30
0·50%	14·44	0·23	0·74	0·30
0·70%	19·33	0·23	0·94	0·30
1%	28·24	0·23	1·24	0·30
2%	55·86	0·23	2·23	0·30
100%	2672[1]	0[1]	99[2]	0·3[3]
Proportion of fluid (B)				
0%	0·63	0·23	0·25	0·31
5%	3·20	0·22	0·32	0·29
10%	5·77	0·21	0·39	0·27
15%	8·34	0·20	0·45	0·26
20%	10·90	0·19	0·52	0·24
30%	16·04	0·16	0·66	0·21
40%	21·18	0·14	0·79	0·18
100%	52[4]	0[1]	1·6[3]	0[1,3]

Fluid (A) represents the subduction-derived fluid with higher contents of Ba, La, Nb and Yb. Fluid (B) represents the subduction-derived fluid with lower contents of Ba, La, Nb and Yb.
[1]Tatsumi & Hanyu (2003); Ba content for fluid derived from subducted sediment.
[2]Stolper & Newman (1994).
[3]Bizimis *et al*. (2000).
[4]Stein *et al*. (1997).

fluid added ranges from 5% to >40% from the interior (at the NE end of the traverse) to the western margin (at the SW end of the traverse) of the Yangtze craton (Fig. 18b). In detail, subgroups with low (at the NE end of the traverse), intermediate and high (at the SW end of the traverse) LILE/LREE ratios are indicative of 0·7–4%, 4–20% and 20–>40% of mantle partial melting, which corresponds to 5–15%, 12–30% and 30–>40% subduction-derived fluid introduced into the mantle wedge, respectively. This result confirms the inference from the primitive mantle-normalized trace element patterns (Fig. 6). However, the calculated results of the modal batch melting model indicate degrees of partial melting of >40%; these are rather high and seem inconsistent with the small volumes of the magmatism (Fig. 1) and high LILE concentrations of the studied rocks (Fig. 7). Additionally, the assumption of modal melting is clearly an oversimplification because minor phases such as phlogopite, spinel and clinopyroxene preferentially enter the melt with respect to olivine and orthopyroxene (Wilson, 1989). Moreover, the distinctive and systematic variation trends in trace element abundances and their ratios from NE to SW along the traverse (Figs 1 and 17) suggest that some minerals (e.g. phlogopite, apatite and titanite) may be preferentially consumed ahead of others (e.g. olivine, orthopyroxene, rutile) with increasing degree of partial melting. Thus the proportions of the different mineral phases in the mantle source region will vary during progressive mantle partial melting. Therefore a non-modal batch melting model was used to simulate the mantle partial melting process and to constrain changes in melt composition as some phases become preferentially exhausted in the residue as the degree of the partial melting increases. We assumed $P = 0{\cdot}01D_{\mathrm{Apatite}} + 0{\cdot}25D_{\mathrm{Clinopyroxene}} + 0{\cdot}3D_{\mathrm{Olivine}} + 0{\cdot}2D_{\mathrm{Orthopyroxene}} + 0{\cdot}08D_{\mathrm{Phlogopite}} + 0{\cdot}005D_{\mathrm{Rutile}} + 0{\cdot}055D_{\mathrm{Spinel}} + 0{\cdot}1D_{\mathrm{Titanite}}$ (see Appendix B), as phlogopite, apatite, spinel, clinopyroxene and titanite are considered to be completely consumed into the melt before rutile, olivine and orthopyroxene, based on above interpretations (Fig. 17). The calculated results of the non-modal batch melting model (Table 9) show that the variation trends in the degree of partial melting and amount of subduction-derived fluid added are similar to those of the modal batch melting model from the interior to the western margin of the craton (Fig. 18). However, the degree of partial melting and the amount of subduction-derived fluid added are smaller for each of the subgroups compared with the modal batch melting model. For non-modal batch melting (Table 9) calculated with the concentrations of Ba, La, Nb and Yb in fluid (A) the degree of partial melting ranges from 1% to 15% and the proportion of subduction-derived fluid added from ~0·1% to ~0·7% from the interior to the western margin of the Yangtze craton (Fig. 18c); using the concentrations of Ba, La, Nb and Yb in fluid (B) the degree of partial melting ranges from 0·6% to 15% and the proportion of subduction-derived fluid added from 5% to 25% from the interior to the western margin of the Yangtze craton (Fig. 18d). If fluid (A) had approximately 5 times greater Ba concentration (12 237 ppm) as proposed by Tatsumi & Hanyu (2003) (for fluid derived from subducted amphibolite plus 20% subducted sediment) then the maximum contribution of slab fluid would become vanishingly small (changing from 0·7% to 0·1%). This suggests that such a high Ba content for the slab fluid is not realistic.

For both modal and non-modal batch melting models, a decrease in the concentrations of Ba, La and Yb in the subduction-derived fluid added relative to those of fluid (A) and fluid (B) would not lead to significant changes in the degree of partial melting, but would result in a significant increase in the proportion of subduction-derived fluid added for each of the corresponding subgroups from the interior to the western margin of the Yangtze craton. This suggests that total amount of Ba, La, Nb and Yb in the subduction-derived fluid added should be relatively stable during generation of the magma for each of the subgroups. It should be noted

Table 8: Variation of La/Yb and Ba/Nb based on modal batch melting model

Fluid (A) content:	0%		0·1%		0·3%		0·5%		1%		2%	
	Ba/Nb	La/Yb	Ba/Nb	La/Yb	Ba/Nb	La/Yb	Ba/Nb	La/Yb	Ba/Nb	La/Yb	Ba/Nb	La/Yb
Degree of melting												
0·10%	25·43	82·28	137·02	114·78	360·88	179·78	585·63	244·79	1151·49	407·34	2300·54	732·50
1%	23·18	59·33	124·92	82·77	329·00	129·64	533·90	176·52	1049·78	293·74	2097·34	528·22
5%	16·71	26·08	90·05	36·38	237·17	56·98	384·88	77·59	756·77	129·11	1511·94	232·17
10%	12·47	15·00	67·19	20·92	176·96	32·77	287·17	44·62	564·65	74·25	1128·10	133·53
15%	10·00	10·33	53·88	14·42	141·91	22·58	230·30	30·75	452·82	51·16	904·67	92·00
20%	8·38	7·76	45·17	10·83	118·98	16·96	193·08	23·10	379·64	38·44	758·47	69·12
25%	7·24	6·14	39·03	8·56	102·80	13·41	166·83	18·26	328·03	30·38	655·37	54·63
30%	6·40	5·01	34·47	6·99	90·79	10·95	147·33	14·91	289·68	24·82	578·75	44·63
35%	5·74	4·19	30·95	5·85	81·50	9·16	132·26	12·47	260·06	20·75	519·57	37·31
40%	5·22	3·56	28·14	4·97	74·12	7·79	120·28	10·60	236·49	17·64	472·48	31·73

Fluid (B) content:	0%		5%		15%		30%		40%	
	Ba/Nb	La/Yb	Ba/Nb	La/Yb	Ba/Nb	La/Yb	Ba/Nb	La/Yb	Ba/Nb	La/Yb
Degree of melting										
0·10%	25·43	82·28	135·89	109·99	395·81	175·20	924·93	307·95	1424·65	433·32
1%	23·18	59·33	123·89	79·32	360·85	126·34	843·23	222·07	1298·82	312·48
5%	16·71	26·08	89·31	34·86	260·13	55·53	607·87	97·61	936·29	137·34
10%	12·47	15·00	66·64	20·05	194·09	31·94	453·55	56·14	698·60	78·99
15%	10·00	10·33	53·44	13·81	155·65	22·00	363·72	38·68	560·23	54·42
20%	8·38	7·76	44·80	10·38	130·50	16·53	304·94	29·06	469·70	40·89
25%	7·24	6·14	38·71	8·20	112·76	13·07	263·49	22·97	405·85	32·32
30%	6·40	5·01	34·19	6·70	99·57	10·67	232·68	18·76	358·40	26·40
35%	5·74	4·19	30·69	5·60	89·39	8·92	208·89	15·69	321·75	22·07
40%	5·22	3·56	27·91	4·76	81·29	7·59	189·96	13·34	292·59	18·77

that the modelling results depend on a number of assumptions; for example, the depleted mantle and fluid compositions, and the partition coefficients and proportions of residual mineral phases. However, our calculations show that the effect of reasonable variations in these parameters on the final results of the modelling is not significant. The overall variation trends of La/Yb vs Ba/Nb ratios are the same, depending on the change in the degree of partial melting and the amount of fluid added, when some initial parameters are changed (e.g. proportion of residual mineral phases).

Our estimates of the degrees of partial melting (0·6–15%) are broadly compatible with the conclusions of Pearce & Parkinson (1993) and Barragan *et al.* (1998), who proposed that the degree of partial melting in the source of arc volcanic rocks mostly falls within the range 2–15%. Some WSYP magmas from the NE end of the traverse (Fig. 1) appear to be produced by very low degrees of partial melting (<3%; Fig. 18c and d), which is reflected in the overall high incompatible element concentrations in these WSYP magmatic rocks (Figs 6 and 7). The proportions of sediment-derived fluid added to mantle wedge (~0·1–25%) beneath the western part of the Yangtze craton are also consistent with previous estimates for arc volcanics (Turner *et al.*, 1996, 1997; Barragan *et al.*, 1998; Turner, 2002).

Petrogenetic model

Characteristic zonations in the radiogenic isotope composition of subduction-related volcanic rocks have been revealed across a number of island arcs (e.g. Churikova

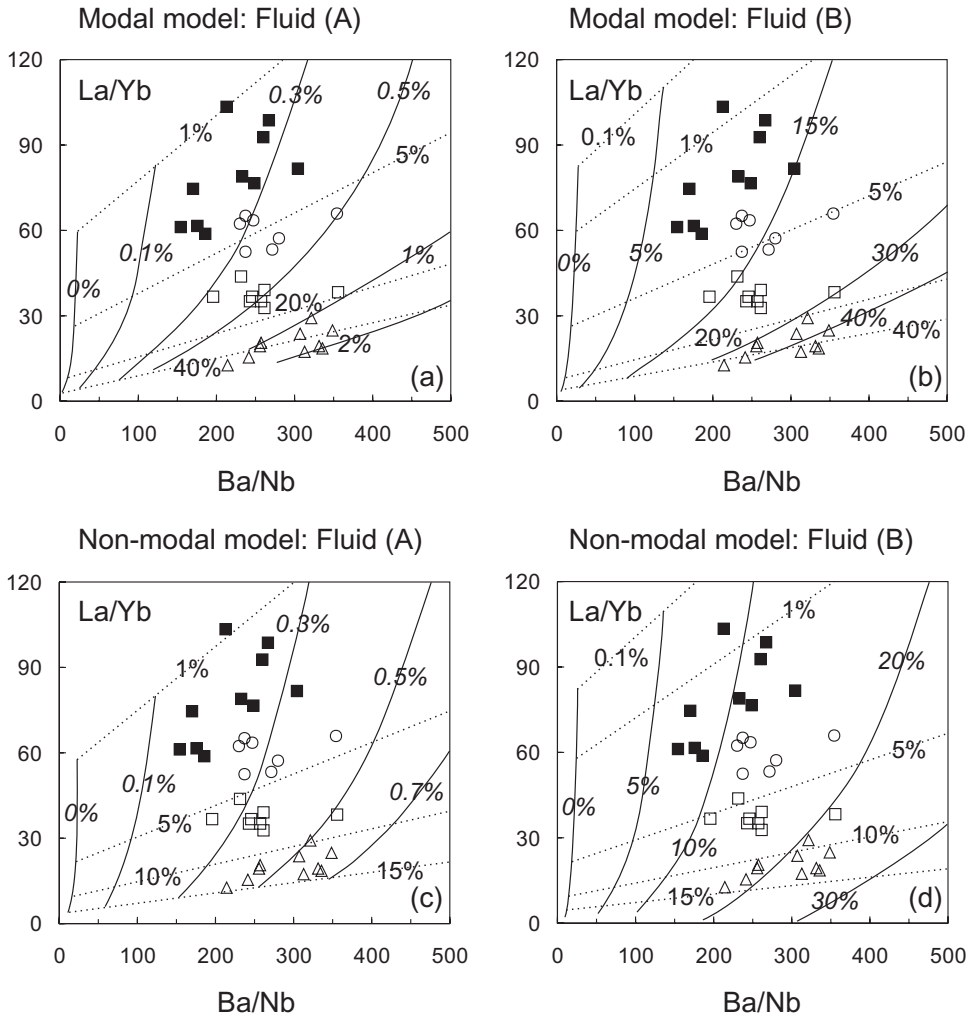

Fig. 18. Trace element modelling results illustrating the variation of La/Yb vs Ba/Nb. The numbers (%) along the dotted lines represent the degree of mantle partial melting. The numbers (%) along the continuous lines (in italics) are the proportion of the subduction-derived fluid in the mantle source region. The symbols are as in Fig. 2a. (a) Modal batch partial melting model calculated with the concentrations of Ba, La, Nb and Yb in fluid (A); (b) modal batch partial melting model calculated with the concentrations of Ba, La, Nb and Yb in fluid (B); (c) non-modal batch partial melting model calculated with the concentrations of Ba, La, Nb and Yb in fluid (A); (d) non-modal batch partial melting model calculated with the concentrations of Ba, La, Nb and Yb in fluid (B). We assumed depleted MORB-source mantle as the source material (see Appendix B), based on data from Sun & McDonough (1989). The concentrations of these trace elements for MORB-source mantle are 0·1 × MORB (Ba 0·63 ppm, La 0·25 ppm, Nb 0·23 ppm and Yb 0·31 ppm; for more detailed discussion see Appendix B). We select fluid (A) and fluid (B) to represent a subduction-derived fluid with higher contents of Ba, La, Nb and Yb and a fluid with lower contents of these elements, respectively. The concentrations of Ba, La, Nb and Yb in fluid (A) and fluid (B) are shown in Table 7. The mineral phases and their modal abundances in the mantle source region after introducing the subduction-derived fluid are olivine (60%), orthopyroxene (25%), clinopyroxene (8%), spinel (2%), phlogopite (2%), titanite (2%), rutile (0·5%) and apatite (0·5%). Partition coefficients for La, Yb, Ba and Nb in these mineral phases were taken from the GERM website (http://earthref.org/GERM/).

et al., 2001; Elburg *et al.*, 2002). The Sr–Nd–Pb isotope compositions of the WSYP rocks are clearly enriched, except for sample CH9854 (Fig. 9). This is interpreted to result from the input of fluids derived mainly from the dehydration of subducted sediments, with a more radiogenic Sr and less radiogenic Nd composition than the mantle wedge. The WSYP lavas display linear arrays in Sr–Nd and Pb–Pb isotope diagrams, and the Pb isotope compositions of the WSYP lavas lie between the source of Indian MORB and marine sediments (Fig. 9), probably reflecting two-component mixing in the mantle source region. However, no well-preserved compositional zonation of Sr–Nd–Pb isotopes can be recognized and the isotope ratios of most WSYP samples display overlapping characteristics from the western margin to the interior of the Yangtze craton (Fig. 9). Thus, the isotope geochemistry appears to be decoupled from the trace element zonation from NE to SW along the traverse (Figs 1 and 7). This decoupled characteristic may be a consequence of multiple fluid enrichment events occurring in the

Table 9: Variation of La/Yb and Ba/Nb based on non-modal batch melting model

Fluid (A) content:	0%		0·1%		0·3%		0·5%		0·7%	
	Ba/Nb	La/Yb	Ba/Nb	La/Yb	Ba/Nb	La/Yb	Ba/Nb	La/Yb	Ba/Nb	La/Yb
Degree of melting										
0·10%	25·49	82·07	133·73	114·50	350·86	179·34	568·87	244·19	787·75	309·05
1%	23·74	57·67	124·53	80·44	326·72	126·00	529·72	171·57	733·54	217·13
5%	18·14	21·67	95·14	30·24	249·62	47·36	404·72	64·49	560·44	81·61
10%	13·95	9·52	73·17	13·28	191·96	20·80	311·23	28·32	430·99	35·84
15%	11·29	4·37	59·21	6·10	155·34	9·56	251·86	13·02	348·77	16·47
20%	9·45	1·53	49·56	2·14	130·03	3·35	210·82	4·57	291·93	5·78
Fluid (B) content:	0%		5%		10%		20%		30%	
	Ba/Nb	La/Yb	Ba/Nb	La/Yb	Ba/Nb	La/Yb	Ba/Nb	La/Yb	Ba/Nb	La/Yb
Degree of melting										
0·10%	25·49	82·07	136·25	109·72	259·31	140·44	551·58	213·39	927·36	307·19
1%	23·74	57·67	126·87	77·09	241·47	98·67	513·62	149·93	863·54	215·83
5%	18·14	21·67	96·93	28·98	184·49	37·09	392·42	56·35	659·76	81·13
10%	13·95	9·52	74·54	12·72	141·87	16·29	301·78	24·75	507·37	35·62
15%	11·29	4·37	60·32	5·85	114·81	7·49	244·21	11·37	410·59	16·37
20%	9·45	1·53	50·49	2·05	96·10	2·63	204·41	3·99	343·67	5·74

lithospheric mantle beneath the western part of the Yangtze craton. The enrichment of Sr–Nd–Pb isotope ratios reflects a time-integrated process; conversely, the enrichment of the incompatible trace elements may indicate a relatively recent enrichment process.

Geological observations suggest that oceanic plate subduction beneath the western margin of the Yangtze craton is likely to have been the dominant process that resulted in the enrichment of the mantle lithosphere (Xu *et al.*, 1995; Wang *et al.*, 2000). Previous studies have shown that the western margin of the Yangtze craton has undergone two periods of ocean plate subduction, which occurred in the late Proterozoic and Palaeozoic (YBGMR, 1990; Xu *et al.*, 1995; Wang *et al.*, 2000). The enrichment in Sr–Nd–Pb isotopic composition (Fig. 9a) probably reflects the Proterozoic subduction, whereas the trace element enrichment (Fig. 6) displays the overprint of two earlier periods of oceanic subduction, probably mainly dominated by the Palaeozoic subduction process. If this inference is right, then the lack of any isotope compositional zonation and overlap of the Sr–Nd–Pb isotope ratios from the western margin to the interior of the Yangtze craton suggest that the effects of Proterozoic subduction have been disturbed by the subsequent Palaeozoic subduction. Compared with the Palaeozoic subduction, the metasomatized mantle that resulted from the Proterozoic subduction had a considerably longer time period for the generation of radiogenic daughter enrichment (e.g. ^{87}Sr, ^{143}Nd, ^{207}Pb, ^{208}Pb) and resulted in relatively radiogenic Sr, Pb isotope ratios and unradiogenic Nd isotope ratios. We propose that the Proterozoic subduction provided the dominant Sr–Nd–Pb isotope enrichment of the mantle lithosphere.

Nd isotope model age (T_{DM}) calculations for the WSYP potassic rocks can provide constraints on the timing of the subduction-related mantle enrichment events; Proterozoic model ages (almost all samples within the range 0·7–1·6 Ga; Table 4) probably indicate that the metasomatism of the sub-continental lithospheric mantle of the western margin of the Yangtze craton predominantly occurred in Proterozoic times rather than during the Palaeozoic. The well-preserved compositional zonations in incompatible trace element ratios (Figs 7 and 8), however, suggest that the incompatible trace element fingerprint of the Palaeozoic subduction-related metasomatism may have overwhelmed that of the Proterozoic subduction.

Three samples (WH79, WH76 and WH91) have high $^{87}Sr/^{86}Sr$ and low $^{143}Nd/^{144}Nd$ (Fig. 9). This feature could be regarded as indicative of crustal contamination.

However, the high Nd and Sr contents of the three samples (Table 3) mean that their isotopic compositions are very difficult to modify by contamination with crustal rocks. Moreover, these samples have Mg numbers ranging from 0·69 to 0·73, which also makes crustal contamination unlikely. Additionally, the low Pb isotope ratios (Fig. 9) of the three samples are not consistent with crustal contamination. We propose that the considerable differences in Sr–Nd–Pb isotope ratios probably reflect variations in the relative concentrations of elements transported by the fluid (Taylor & Nesbitt, 1998). The parental magmas of these three samples with $^{87}Sr/^{86}Sr$ >0·709 were generated from a mantle source modified by subduction-derived fluids, which introduced higher concentrations of Rb than in the source of the other samples, possibly indicating a strong fluid enrichment event. Sample CH9854 has a slightly depleted Nd–Sr isotopic composition relative to Bulk Silicate Earth that appears to indicate that it is derived from an asthenospheric mantle source; however, its low Nb content (5 ppm, Table 3) makes this inference unlikely. It has been shown that the fluid formed by dehydration of altered oceanic crust has relatively low Sr and high Nd isotope ratios and thus shows a depleted Nd–Sr isotopic composition (Hawkesworth *et al.*, 1993; Turner *et al.*, 1997; Turner, 2002). A possible explanation for the apparent Nd–Sr isotopic depletion of sample CH9854 is that its mantle source was mainly modified by altered oceanic crust-derived fluid. Geological observations show that these samples (WH79, WH76, WH91 and CH9854), which have distinct Sr–Nd–Pb isotope characteristics, are located to the south of the traverse by around 150 km and 200 km, rather than along the traverse (Fig. 1). The difference in their Sr–Nd–Pb isotope compositions (Fig. 9) from those of other samples located along the traverse (Fig. 1) probably suggests compositional variation of the fluids added along the palaeo-subduction zone.

The relative uniformity of Sr–Nd–Pb isotopic compositions from NE to SW along the traverse suggests that the composition of the fluid released from the Proterozoic subduction zone was relatively homogeneous, although a few samples (WH79, WH76, WH91 and CH9854) have distinctive isotope ratios. This may reflect relatively weak compositional zonation in the Proterozoic. Our conclusion shows that, like arc volcanic rocks, post-collisional potassic rocks can also display compositional zonation across the palaeo-subduction zone, and that the overprinting of two phases of oceanic crustal subduction can result in a well-preserved compositional zonation of trace elements perpendicular to the trend of the subduction zone.

The systematic compositional zonation in the WSYP rocks from SW to NE (Figs 7 and 8) requires a subduction- and metasomatism-related petrogenetic model (Fig. 19). Ocean plate subduction beneath the western margin of the Yangtze craton, prior to WSYP magma generation, occurred in both Proterozoic and Palaeozoic times (YBGMR, 1990; Xu *et al.*, 1995; Wang *et al.*, 2000). The metasomatic fluids were generated as a result of dehydration of subducted sediments. Typically, these low volume, volatile-rich fluids freeze during ascent to form metasomatic layers or veins within the mantle wedge above the fossil subduction zone (Haggerty, 1989; McKenzie, 1989). We envision that the mantle lithosphere beneath the western part of the Yangtze craton in the Proterozoic was affected by an extensive network of fluid-derived metasomatic veins. These compositional features of the subduction-modified lithospheric mantle beneath the western part of the Yangtze craton may have been overprinted and disturbed by Palaeo-Tethyan ocean subduction in Palaeozoic times. The compositional zonation of trace elements across the Palaeozoic subduction zone can be reconstructed because of the Palaeo-Tethyan ocean subduction underneath the western part of the Yangtze craton (Fig. 19a). The collision of India and Asia (inset in Fig. 1) at about 55–50 Ma marked a significant change in the tectonic regime of SE Tibet. One of the important consequences was the formation of the ASRR shear zone in SE Tibet (Fig. 1), which may have caused extensional or transtensional movements on pre-existing fault systems. Another consequence was the formation of normal faults (Wang *et al.*, 1998; Duan, 1999; Tan & Zhu, 1999) and pull-apart basins (He *et al.*, 1996; Tan, 1999) at the western margin of the Yangtze craton. The onset of magmatic activity along the ASRR shear zone, starting in the Eocene, could have been associated with a progressive rise in heat flow and isotherms within the upper mantle (Fig. 19b), which have been attributed to the uprise of a Cenozoic asthenospheric mantle diapir on the basis of geophysical studies (Liu *et al.*, 1989; Zhong, 1998; Duan, 1999; Liu, 1999; Tan & Zhu, 1999; Zhong *et al.*, 2000). Eruptions of late Cenozoic alkaline basalts intercalated in upper Tertiary sandstone in the western Yangtze craton support this conclusion (YBGMR, 1990; SBGMR, 1991; Liu, 1999). As a result of extension and heat flow from the asthenosphere, the previously enriched mantle wedge (i.e. phlogopite peridotite veins; fluid-bearing domains within the mantle lithosphere) beneath the western part of the Yangtze craton would have preferentially undergone decompressional melting, triggering the formation of the WSYP potassic magmas (Fig. 19b). The correlations between the trace element compositions, degrees of partial melting and the thickness of the overlying lithosphere argue for a decompression melting hypothesis in the generation of the WSYP lavas. The broadly coeval ages of the potassium-rich rocks in the WSYP and the left-lateral strike-slip motions along the ASRR shear zone support this interpretation.

The time interval between the Palaeozoic subduction event and formation of the potassic lavas in the Tertiary

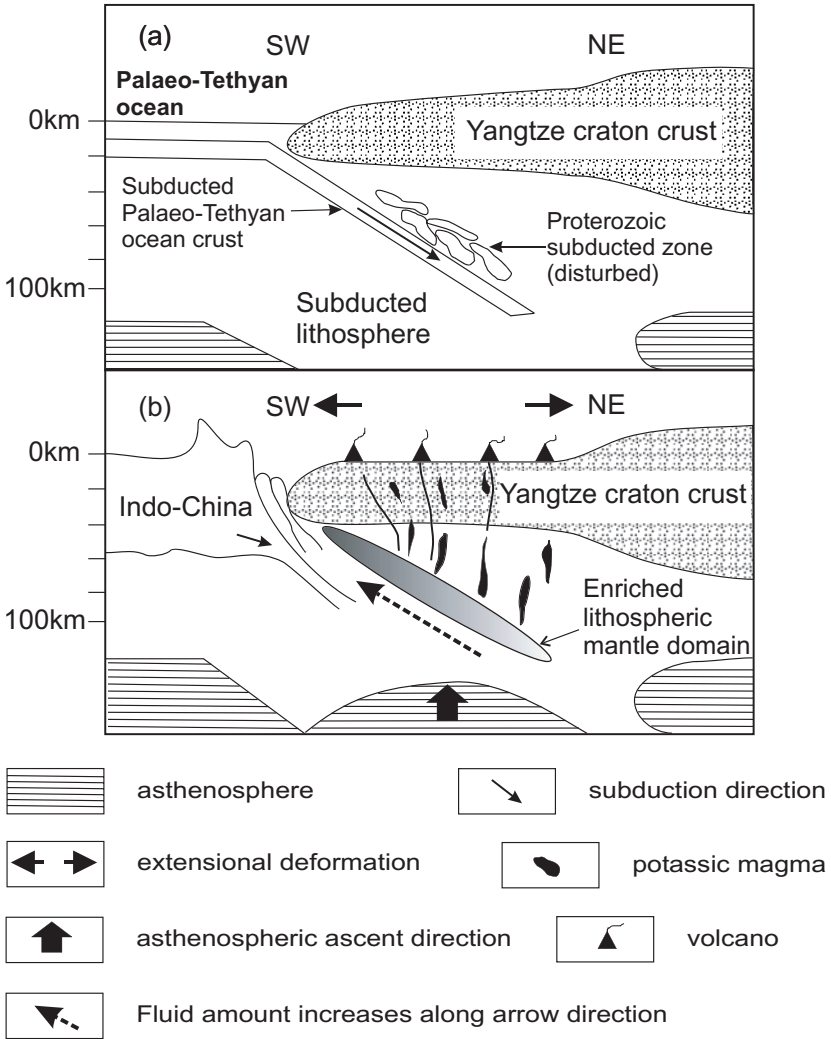

Fig. 19. Schematic representation of the model for potassic magma genesis in the WSYP. Each panel is drawn parallel to the studied traverse from present-day SW on the left to NE on the right. (a) Late Devonian Palaeo-Tethyan ocean crust subducted beneath the western part of the Yangtze craton (Wang *et al.*, 2000) and disturbed mantle modified above a Proterozoic subduction zone previously located underneath the Yangtze craton. (b) Reconstructed pattern of compositional zonation that resulted from Palaeo-Tethyan ocean crust subduction. Metasomatized lithospheric mantle has undergone decompressional partial melting resulting in the generation of the WSYP magmas, owing to the Tertiary reactivation of deep faults along the ASRR shear zone.

is around 320 Ma. Considerable differences in major and trace element contents (Fig. 4) between the Permo-Triassic Emeishan flood basalts and the WSYP rocks suggest that partial melting did not occur in the lithospheric mantle beneath the study area during the eruption of the Emeishan flood basalts. This implies that the ascent of the mantle plume thought to have generated the Emeishan flood basalts did not result in any significant interaction with the sub-continental lithospheric mantle beneath the study area. This is possibly because the mantle plume centre (or head) was to the east of the study area (Chung *et al.*, 1998*a*). The presence of the Emeishan flood basalts in the study area (Fig. 1) could merely be a consequence of westward movement of the lava flows from the mantle plume centre because of the low viscosity of the basaltic magmas. The differences in compositions between the Emeishan flood basalts and WSYP rocks probably indicate differences in the depths (or mantle source regions) of magma generation. The Emeishan basalts are interpreted to result from a mantle plume, which probably originated from a sub-lithospheric OIB-like mantle source (Xu *et al.*, 2001*a*).

The 'frozen-in' enriched domains within the sub-continental lithospheric mantle were thus well preserved for a relatively long period of geological time, presumably

suggesting that the 40–24 Ma tectonic events (including formation of the ASRR shear zone) in the western margin of the Yangtze craton were extremely strong. Although the ASRR shear zone had a significant influence on the physical processes of plate movement in SE Tibet, it has left little imprint on the chemistry of the associated magmas in the investigated area. Moreover, several studies (Chen *et al.*, 1995; Zhang & Zhong, 1996; Zhong, 1998; Tan, 1999; Zhong *et al.*, 2000) show that the western part of the Yangtze craton underwent clockwise rotation accompanied by plate-scale lateral extrusion and left-lateral strike-slip motion along the ASRR shear zone. Extensional or transtensional tectonic motions also generated conduits for magma ascent, as evidenced by the numerous dykes in the WSYP.

CONCLUSIONS

Based on the interpretation of geochemical data for Paleogene calc-alkaline lamprophyric rocks in the WSYP, we present a petrogenetic model to explain the spatial variation of compositions along a SW–NE traverse. This model advocates an important role for metasomatic components derived from Proterozoic and Palaeozoic subduction zones in the enrichment of the mantle source of the magmas. The lateral zonation of magmatic rock compositions perpendicular to the western boundary of the Yangtze craton from SW to NE is interpreted to reflect variations in both the degree of mantle partial melting and the amount of subduction-derived fluid introduced into the overlying mantle wedge beneath the western margin of the Yangtze craton. The potassic lavas extend away from the ASRR shear zone for about 270 km, which we interpret as evidence that the effects of the palaeo-subducted slab reached beneath the Xichang area at the far NE end of the traverse (Fig. 1). The source region of the potassic lavas is situated within the sub-continental lithospheric mantle, which is relatively depleted compared with the source of the Permo-Triassic Emeishan flood basalts. The left-lateral strike-slip motions of the ASRR shear zone and reactivation of pre-existing, trans-lithospheric fault systems triggered melting and provided conduits for magma ascent, facilitating formation of potassic magmas beneath the WSYP, in SE Tibet. This study shows that, like arc volcanic rocks, post-collision potassic rocks can display compositional zonation across the palaeo-subduction zone, and that overprinting of two periods of oceanic crustal subduction can result in a well-preserved compositional zonation of trace elements perpendicular to the trend of the trench. This is complementary to previous observations of zonations in the composition of arc volcanic rocks.

ACKNOWLEDGEMENTS

We are deeply grateful to Professor Marjorie Wilson for helpful discussions on the manuscript, and careful and enthusiastic improvement of the English, from which the first author benefited considerably. Z.F.G. thanks J. T. Han for his constructive comments. Three referees (Helen Williams, Marlina Elburg and Yoshi Tatsumi) are thanked for their constructive comments that improved the manuscript. Z. J. Fan is appreciated for his friendly help and guide in the fieldwork. Further logistic help was provided during field campaigns in 1997, 1998, 2000 and 2001 by Sichuan and Yunnan Bureaux of Geology and Mineral Resources of China. Z.F.G. acknowledges the Chinese Academy of Sciences, Ministry of Scientific and Technology of China (MSTC) and Ministry of the Flemish Community in Belgium (MFCB) for supporting his long visit to Katholieke Universiteit of Leuven in Belgium. This study was supported by a co-operative project of MSTC and MFCB during 1997–2002 and also funded by the Natural Science Foundation of China (NSFC: 40372045) and Chinese Academy of Sciences Key Project (KZCX2-SW-133). Z.F.G.'s stay in the UK was funded by a joint project supported by the Royal Society of the UK and the Natural Science Foundation of China (2003–2005).

SUPPLEMENTARY DATA

Supplementary data for this paper are available at *Journal of Petrology* online.

REFERENCES

Baksi, A. K., Archibald, D. A. & Farrar, E. (1996). Intercalibration of $^{40}Ar/^{39}Ar$ dating standards. *Chemical Geology* **129**, 307–324.

Barragan, R., Geist, D., Hall, M., Larson, P. & Kurz, M. (1998). Subduction controls on the compositions of lavas from the Ecuadorian Andes. *Earth and Planetary Science Letters* **154**, 153–166.

Bizimis, M., Salters, V. J. M. & Bonatti, E. (2000). Trace and REE content of clinopyroxenes from supra-subduction zone peridotites: implications for melting and enrichment processes in island arcs. *Chemical Geology* **165**, 67–85.

Boven, A., Pasteels, P., Punzalan, L. E., Liu, J., Luo, X., Zhang, W., Guo, Z. & Hertogen, J. (2002). $^{40}Ar/^{39}Ar$ geochronological constraints on the age and evolution of the Permo-Triassic Emeishan volcanic province, southwest China. *Journal of Asian Earth Sciences* **20**, 157–175.

Brenan, J. M., Shaw, H. F., Ryerson, F. J. & Phinney, D. L. (1995). Mineral–aqueous fluid partitioning of trace elements at 900°C and 2·0 GPa: constraints on the trace element chemistry of mantle and deep crustal fluids. *Geochimica et Cosmochimica Acta* **59**, 3331–3350.

Carmichael, I. S. E., Lange, R. A. & Luhr, J. F. (1996). Quaternary minettes and associated volcanic rocks of Mascota, western Mexico: a consequence of plate extension above a subduction modified mantle wedge. *Contributions to Mineralogy and Petrology* **124**, 302–333.

Chen, H. H., Dobson, J. & Heller, F. (1995). Paleomagnetic evidence for clockwise rotation of the Simao region since Cretaceous: a

consequence of India–Asia collision. *Earth and Planetary Science Letters* **134**, 203–217.

Chen, Y., Luo, Z. & Liu, C. (2001). New recognition of Kangding–Mianning metamorphic granitic complexes from Sichuan, western Yangtze craton: evidence from Nd isotopic composition. *Earth Science-Journal of China University of Geosciences* **26**, 279–285 (in Chinese with English abstract).

Chung, S.-L. & Jahn, B.M. (1995). Plume–lithosphere interaction in generation of the Emeishan flood basalts at the Permian–Triassic boundary. *Geology* **23**, 889–892.

Chung, S.-L., Jahn, B. M., Wu, G. Y., Lo, C. H. & Cong, B. L. (1998*a*). The Emeishan flood basalt in SW China: a mantle plume initiation model and its connection with continental break-up and mass extinction at the Permian–Triassic boundary. In: Flower, M. F. J., Chung, S.-L., Lo, C.-H. & Lee, T.-Y. (eds) *Mantle Dynamics and Plate Interactions in East Asia. Geodynamics Series, American Geophysical Union* **27**, 47–58.

Chung, S.-L., Lo, C.-H., Lee, T.-Y., Zhang, Y. Q., Xie, Y. W., Li, X. H., Wang, K.-L. & Wang, P.-L. (1998*b*). Diachronous uplift of the Tibetan plateau starting 40 Myr ago. *Nature* **394**, 769–773.

Churikova, T., Dorendorf, F. & Worner, G. (2001). Sources and fluids in the mantle wedge below Kamchatka, evidence from across-arc geochemical variation. *Journal of Petrology* **42**, 1567–1593.

Class, C., Miller, D. M., Goldstein, S. L. & Langmuir, C. H. (2000). Distinguishing melt and fluid subduction components in Umnak volcanics: Aleutian arc. *Geochemistry, Geophysics, Geosystems* **1**, 1999GC000010.

Cong, B. L. (1988). *Formation and Evolution of the Panxi Paleorift*. Beijing: Science Press, 427 pp. (in Chinese with English abstract).

Deng, W. M., Huang, X. & Zhong, D. L. (1998*a*). Alkaline-rich porphyric rocks in the northern part of Jinshajiang zone, west Yunnan and its relations with intraplate deformation. *Sciences in China* (*Series D*) **28**, 111–117 (in Chinese with English abstract).

Deng, W. M., Huang, X. & Zhong, D. L. (1998*b*). Petrological characteristics and genesis of Cenozoic alkaline-rich porphyry in west Yunnan, China. *Scientia Geologica Sinica* **33**, 412–425 (in Chinese with English abstract).

DePaolo, D. J. (1988). *Neodymium Isotope Geochemistry: an Introduction*. New York: Springer, 230 pp.

Dickinson, W. R. & Hatherton, T. (1975). Potash–depth (K–*h*) relations in continental margin and intra oceanic arc. *Geology* **3**, 53–56.

Dosso, L., Bougault, H., Beuzart, P., Calvez, J. Y. & Joron, J. L. (1988). The geochemical structure of the South-East Indian Ridge. *Earth and Planetary Science Letters* **88**, 47–59.

Duan, J. Z. (1999). The characteristics of the Cenozoic strike-slip (transform) convergent structure in the three-river area of west Yunnan. *Yunnan Geology* **18**, 99–111 (in Chinese with English abstract).

Edgar, A. D., Green, D. H. & Hibberson, W. O. (1976). Experimental petrology of highly potassic magmas. *Journal of Petrology* **17**, 339–356.

Elburg, M. A., Bergen, M. V., Hoogewerff, J., Foden, J., Vroon, P., Zulkarnain, I. & Nasution, A. (2002). Geochemical trends across an arc–continent collision zone: magma sources and slab–wedge transfer processes below the Pantar Strait volcanoes, Indonesia. *Geochimica et Cosmochimica Acta* **66**, 2771–2789.

Elliott, T., Planck, T., Zindler, A., White, W. & Bourdon, B. (1997). Element transport from slab to volcanic front at the Mariana arc. *Journal of Geophysical Research* **102**, 14991–15019.

Fan, W. M., Guo, F., Wang, Y. J. & Ge, L. (2003). Late Mesozoic calc-alkaline volcanism of post-orogenic extension in the northern Da Hinggan Mountains, northeastern China. *Journal of Volcanology and Geothermal Research* **121**, 115–135.

Feng, B., Lu, M., Wen, Q., Zhang, Z., Yang, T., Jiang, X. & Peng, Q. (1990). *The Pre-Cambrian Geological Setting and Deposits in Kangdian Area of the Western Yangtze Craton*. Beijing: Geological Publishing House, 202 pp. (in Chinese with English abstract).

Feng, Q., Ye, M. & Zhang, Z. (1997). Early Carboniferous radiolarians from western Yunnan. *Acta Micropalaeontologica Sinica* **14**, 79–92 (in Chinese with English abstract).

Ferguson, E. M. & Klein, E. M. (1993). Fresh basalts from the Pacific–Antarctic Ridge extend the Pacific geochemical province. *Nature* **366**, 330–333.

Flower, M., Tamaki, K. & Hoang, H. (1998). Mantle extrusion: a model for dispersed volcanism and DUPAL-like asthenosphere in east Asia and the western Pacific. In: Flower, M. F. J., Chung, S.-L., Lo, C.-H. & Lee, T.-Y. (eds) *Mantle Dynamics and Plate Interactions in East Asia. Geodynamics Series, American Geophysical Union* **27**, 67–88.

Foley, S. F. & Wheller, G. E. (1990). Parallels in the origin of the geochemical signatures of island arc volcanics and continental potassic igneous rocks: the role of residual titanates. *Chemical Geology* **85**, 1–18.

Foley, S. F., Venturelli, G., Green, D. H. & Toscani, L. (1987). The ultrapotassic rocks: characteristics, classification and constraints for petrogenetic models. *Earth-Science Reviews* **24**, 81–134.

Foley, S. F., Barth, M. G. & Jenner, G. A. (2000). Rutile/melt partition coefficients for trace elements and an assessment of the influence of rutile on the trace element characteristics of subduction zone magmas. *Geochimica et Cosmochimica Acta* **64**, 933–938.

Frey, F. A., Green, D. H. & Roy, S. D. (1978). Integrated models of basalt petrogenesis: a study of quartz tholeiites to olivine melilitites from South Eastern Australia utilizing geochemical and experimental petrological data. *Journal of Petrology* **19**, 463–513.

Gao, S., Ling, W., Qiu, Y., Lian, Z., Hartmann, G. & Simon, K. (1999). Contrasting geochemical and Sm–Nd isotopic compositions of Archean metasediments from the Kongling high-grade terrain of the Yangtze craton: evidence for cratonic evolution and redistribution of REE during crustal anatexis. *Geochimica et Cosmochimica Acta* **63**, 2071–2088.

GERM (Geochemical Earth Reference Model) home page. http://www.earthref.org.

Gill, J. B. (1981). *Orogenic Andesites and Plate Tectonics*. Berlin: Springer, 390 pp.

Goldstein, S. L., O'Nions, R. K. & Hamilton, P. J. (1984). A Sm–Nd study of atmospheric dusts and particulates from major river system. *Earth and Planetary Science Letters* **70**, 221–236.

Govindaraju, K. (1994). Compilation of working values and sample description for 383 geostandards. *Geostandards Newsletter* **18**(special issue), 1–158.

Green, T. H. (1994). Experimental studies of trace-element partitioning applicable to igneous petrogenesis—Sedona 16 years later. *Chemical Geology* **117**, 1–36.

Green, T. H., Blundy, J. D., Adam, J. & Yaxley, G. M. (2000). SIMS determination of trace element partition coefficients between garnet, clinopyroxene and hydrous basaltic liquids at 2–7·5 GPa and 1080–1200°C. *Lithos* **53**, 165–187.

Haggerty, S. E. (1989). Upper mantle opaque mineral stratigraphy and the genesis of metasomatites and alkali-rich melts. In: Danchin, R. V. (ed.) *Proceedings of the Fourth International Kimberlite Conference, Perth. Vol. 2, Section 4. Geological Society of Australia, Special Publication* **14**, 687–699.

Hart, S. R. (1984). A large-scale isotope anomaly in the southern hemisphere mantle. *Nature* **309**, 753–757.

Hawkesworth, C. J., Gallagher, K., Hergt, J. M. & McDermott, F. (1993). Mantle and slab contributions in arc magmas. *Annual Review of Earth and Planetary Sciences* **21**, 175–204.

Hawkesworth, C. J., Turner, S. P., McDermott, F., Peate, D. W. & van Calsteren, P. (1997). U–Th isotopes in arc magmas: implications for element transfer from the subducted crust. *Science* **276**, 551–555.

He, J. & Chen, G. (1988). *The Kangding Gray Gneisses*. Chongqing City: Chongqing Press, 174 pp. (in Chinese with English abstract).

He, K. Z., Zhao, C. H., He, H. S. & Shai, K. Y. (1996). *Intracontinental Rift and Orogeny in Western Yunnan*. Wuhan City: China University of Geosciences Press, 138 pp. (in Chinese with English abstract).

Hertogen, J., Vanlerberghe, L. & Namegabe, M. R. (1985). Geochemical evolution of the Nyiragongo volcano (Virunga, western Africa Rift, Zaire). *Bulletin of Geological Society of Finland* **57**, T. G. Sahama Commemorative Issue, 21–35.

Hirose, K. & Kushiro, I. (1993). Partial melting of dry peridotites at high pressures: determination of compositions of melts segregated from peridotite using aggregates of diamond. *Earth and Planetary Science Letters* **114**, 477–489.

Hoang, N. & Flower, M. (1998). Petrogenesis of Cenozoic basalts from Vietnam: implication for origin of a 'diffuse igneous province'. *Journal of Petrology* **39**, 369–395.

Hochstaedter, A. G., Kepezhinskas, P., Defant, M., Drummond, M. & Koloskov, A. (1996). Insights into the volcanic arc mantle wedge from magnesian lavas from the Kamchatka arc. *Journal of Geophysical Research* **101**, 697–712.

Hochstaedter, A. G., Gill, J. B., Taylor, B., Ishizuka, O., Yuasa, M. & Morita, S. (2000). Across-arc geochemical trends in the Izu–Bonin arc: constraints on source composition and mantle melting. *Journal of Geophysical Research* **105**, 495–512.

Hofmann, A. W. (1997). Mantle geochemistry: the message from oceanic volcanism. *Nature* **385**, 219–229.

Hoogewerff, J. A., Van Bergen, M. J., Vroon, P. Z., Hertogen, J., Wordel, R., Sneyers, A., Nasution, A., Varekamp, J. C., Moens, H. L. E. & Mouchel, D. (1997). U-series, Sr–Nd–Pb isotope and trace-element systematics across an active island arc–continent collision zone: implications for element transfer at the slab–wedge interface. *Geochimica et Cosmochimica Acta* **61**, 1057–1072.

Huang, Z. L., Wang, L. K. & Zhu, C. M. (1997). Petrologic study of lamprophyres in gold deposit, Laowangzai, Yunnan. *Scientia Geologica Sinica* **32**, 74–87 (in Chinese with English abstract).

Ishikawa, T. & Nakamura, E. (1994). Origin of the slab component in arc lavas from across-arc variation of B and Pb isotopes. *Nature* **370**, 205–208.

Jacobsen, S. B. & Wasserburg, G. J. (1980). Sm–Nd isotopic evolution of chondrites. *Earth and Planetary Science Letters* **50**, 139–155.

Jin, X. & Zhu, H. (2000). Determination of 43 trace elements in rock samples by double focusing high resolution inductively coupled plasma-mass spectrometry. *Chinese Journal of Analytical Chemistry* **28**, 563–567 (in Chinese with English abstract).

Keppler, H. (1996). Constraints from partitioning experiments on the composition of subduction zone fluids. *Nature* **380**, 237–240.

LaTourrette, T., Hervig, R. L. & Holloway, J. R. (1995). Trace element partitioning between amphibole, phlogopite, and basanite melt. *Earth and Planetary Science Letters* **135**, 13–30.

Le Bas, M. J., Le Maitre, R. W., Streckeisen, A. & Zanettin, B. (1986). A chemical classification of volcanic rocks based on the total alkali–silica diagram. *Journal of Petrology* **27**, 745–750.

Leeman, W. P., Smith, D. R., Hildreth, W., Palacz, Z. & Rogers, N. (1990). Compositional diversity of Late Cenozoic basalts in a transect across the southern Washington Cascades: implication for subduction zone magmatism. *Journal of Geophysical Research* **95**, 19561–19582.

Leloup, P. H., Lacassin, R., Tapponnier, P., Scharer, U., Zhong, D., Liu, X., Zhang, L., Ji, S. & Trinh, P. T. (1995). The Ailao Shan–Red River shear zone (Yunnan, China), Tertiary transform boundary of Indochina. *Tectonophysics* **251**, 3–84.

Le Maitre, R. W., Bateman, P., Dudek, A., Keller, J., Lameyre, J., Le Bas, M. J., Sabine, P. A., Schmid, R., Sorensen, H., Streckeisen, A., Woolley, A. R. & Zanettin, B. (1989). *A Classification of Igneous Rocks and a Glossary of Terms*. Oxford: Blackwell.

Liu, B., Feng, Q. & Fang, N. (1991). Tectonic evolution of the Palaeotethys in Changning–Menglian belt and adjacent regions, western Yunnan. *Journal of China University of Geosciences* **2**, 529–538 (in Chinese with English abstract).

Liu, B., Feng, Q., Fang, N., Jia, J. & He, F. (1993). Tectonic evolution of Palaeo-Tethys poly-island ocean in Changning–Menglian and Lancangjiang belts, southwestern Yunnan, China. *Earth Science* **18**, 529–538 (in Chinese with English abstract).

Liu, J. H., Liu, F. T. & Wu, H. (1989). The three-dimensional velocity images of the crust and upper mantle in south and north belts of China. *Journal of Geophysics* **32**, 143–152 (in Chinese with English abstract).

Liu, J. Q. (1999). *Volcanoes in China*. Beijing: Science Press, 219 pp. (in Chinese).

Liu, J. Q. (2000). Take another vision to the uplift of the Qing-Zhang (Tibetan) plateau based on Cenozoic volcanism. *Earth Science Frontiers* **7**, 370–371.

Lu, B. X. & Qian, X. G. (1999). A petrolographic study on the hypogenic enclave in Cenozoic alkalic volcanics and alkali-rich porphyry of west Yunnan. *Yunnan Geology* **18**, 127–143 (in Chinese with English abstract).

Lugmair, G. W. & Marti, K. (1978). Lunar initial $^{143}Nd/^{144}Nd$: differential evolution of the lunar crust and mantle. *Earth and Planetary Science Letters* **39**, 349–357.

Luhr, J. F., Allan, J. F., Carmichael, I. S. E., Nelson, S. A. & Hasenaka, T. (1989). Primitive calc-alkaline and alkaline rock types from the western Mexican volcanic belt. *Journal of Geophysical Research* **94**, 4515–4530.

McCulloch, M. T. & Black, L. P. (1984). Sm–Nd isotope systematics of Enderby Land granulites and evidence for the redistribution of Sm and Nd during metamorphism. *Earth and Planetary Science Letters* **71**, 46–58.

McCulloch, M. T., Jaques, A. L., Nelson, D. R. & Lewis, J. D. (1983). Nd and Sr isotopes in kimberlites and lamproites from western Australia: an enriched mantle origin. *Nature* **302**, 400–403.

McKenzie, D. P. (1989). Some remarks on the movement of small melt fractions in the mantle. *Earth and Planetary Science Letters* **95**, 53–72.

Meen, J. K. (1987). Formation of shoshonites from calc-alkaline basalt magmas: geochemical and experimental constraints from the type locality. *Contributions to Mineralogy and Petrology* **97**, 333–351.

Mengel, K. & Green, D. H. (1989). Stability of amphibole and phlogopite in metasomatised peridotite under water-saturated and water-undersaturated conditions. In: *Kimberlites and Related Rocks, Vol. 1. Geological Society of Australia, Special Publication* **14**, 571–581.

Michard, A., Montigny, R. & Schlich, R. (1986). Geochemistry of the mantle beneath the Rodriguez Triple Junction and the South-East Indian Ridge. *Earth and Planetary Science Letters* **78**, 104–114.

Mitchell, R. H. & Bergman, S. C. (1991). *Petrology of Lamproites*. New York: Plenum, 447 pp.

Mo, X., Lu, F. & Deng, J. (1991). Volcanism in Sanjiang Tethyan orogenic belt: new facts and concepts. *Journal of China University Geosciences* **2**, 58–74 (in Chinese with English abstract).

Mo, X., Lu, F., Cheng, S., Zhu, Q., Hou, Z., Yang, K., Deng, J., Liu, X. & He, C. (1993). *Sanjiang Tethyan Volcanism and Related*

Mineralization. Beijing: Geological Publishing House, 267 pp. (in Chinese with English abstract).

Mulder, M. D., Hertogen, J., Deutsch, S. & Andre, L. (1986). The role of crustal contamination in the potassic suite of the Karisimbi volcano (Virunga, African Rift Valley). *Chemical Geology* **57**, 117–136.

Munker, C. (2000). The isotope and trace element budget of the Cambrian Devil River Arc System, New Zealand: identification of four source components. *Journal of Petrology* **41**, 759–788.

Pearce, J. A. (1982). Trace element characteristics of lavas from destructive plate boundaries. In: Thorpe, R. S. (ed.) *Andesites*. New York: Wiley, pp. 525–548.

Pearce, J. A. & Parkinson, I. J. (1993). Trace element models for mantle melting: application to volcanic arc petrogenesis. In: Prichard, H. M., Alabaster, T., Harris, N. B. W. & Neary, C. R. (eds) *Magmatic Processes and Plate Tectonics. Geological Society, London, Special Publications* **76**, 373–403.

Pearce, J. A. & Peate, D. W. (1994). Tectonic implications of the composition of volcanic arc magmas. *Annual Review of Earth and Planetary Sciences* **123**, 251–285.

Peate, D. W., Kokfelt, T. F., Hawkesworth, C. J., van Calsteren, P. W., Hergt, J. M. & Pearce, J. A. (2001). U-series isotope data on Lau Basin glasses: the role of subduction-related fluids during melt generation in back-arc basins. *Journal of Petrology* **42**, 1449–1470.

Peucat, J. J., Vidal, P., Bernard-Griffiths, J. & Condie, K. C. (1988). Sr, Nd and Pb isotopic systematics in the Archaean low- to high-grade transition zone of southern India: syn-accretion vs post-accretion granulites. *Journal of Geology* **97**, 537–550.

Plank, T. & Langmuir, C. H. (1998). The chemical composition of subducting sediment and its consequences for the crust and mantle. *Chemical Geology* **145**, 325–394.

Price, R. C., Kennedy, A. K., Riggs-Sneeringer, M. & Frey, F. A. (1986). Geochemistry of basalts from the Indian Ocean Triple Junction: implication for the generation and evolution of Indian Ocean Ridge basalts. *Earth and Planetary Science Letters* **78**, 379–396.

Qian, X. G. (1999). A preliminary discussion about the petrology and genesis of Cenozoic volcanic rocks in Janchuan–Madeng and Heqing–Dianan areas, west Yunnan. *Yunnan Geology* **18**, 413–424 (in Chinese with English abstract).

Qiu, Y., Gao, S., McNaughton, N. J., Groves, D. I. & Ling, W. (2000). First evidence of >3·2 Ga continental crust in the Yangtze Craton of South China and its implications for Archean crustal evolution and Phanerozoic tectonics. *Geology* **28**, 11–14.

Rehkämper, M. & Hofmann, A. W. (1997). Recycled ocean crust and sediment in Indian Ocean MORB. *Earth and Planetary Science Letters* **147**, 93–106.

Richard, P., Shimizu, N. & Allègre, C. J. (1976). $^{143}Nd/^{144}Nd$, a natural tracer: an application to ocean basalts. *Earth and Planetary Science Letters* **31**, 269–278.

Rickwood, P. C. (1989). Boundary lines within petrologic diagrams which use oxides of major and minor elements. *Lithos* **22**, 247–263.

Robinson, J. A. C. & Wood, B. J. (1998). The depth of the spinel to garnet transition at the peridotite solidus. *Earth and Planetary Science Letters* **164**, 277–284.

Rock, N. M. S. (1984). Nature and origin of calc-alkaline lamprophyres: minettes, vogesites, kersantites and spessartites. *Transactions of Royal Society of Edinburgh (Earth Sciences)* **74**, 193–227.

Rock, N. M. S., Bowes, D. R. & Wright, A. E. (1991). *Lamprophyres*. Glasgow: Blackie, 285 pp.

Roeder, P. L. & Emslie, R. F. (1970). Olivine–liquid equilibria. *Contributions to Mineralogy and Petrology* **29**, 275–289.

Rowell, W. F. & Edgar, A. D. (1983). Cenozoic potassium-rich mafic volcanism in the western U.S.A.: its relationship to deep subduction. *Journal of Geology* **91**, 338–341.

Ryan, J. G., Morris, J., Tera, F., Leeman, W. P. & Tsvetskov, A. (1995). Cross-arc geochemical variations in the Kurile arc as a function of slab depth. *Science* **270**, 625–627.

SBGMR (Sichuan Bureau of Geology and Mineral Resources) (1991). *Regional Geology of Sichuan Province*. Beijing: Geological Publishing House, 730 pp. (in Chinese with English abstract).

Scarrow, J. H. & Cox, K. G. (1995). Basalts generated by decompressive adiabatic melting of a mantle plume: a case study from the Isle of Skye, NW Scotland. *Journal of Petrology* **36**, 3–22.

Scharer, U., Xu, R. H. & Allègre, C. J. (1994). U–Pb geochronology of Gangdese (Transhimalaya) plutonism in the Lhasa–Xigaze region, Tibet. *Earth and Planetary Science Letters* **69**, 311–320.

Sheppard, S. & Taylor, W. R. (1992). Barium- and LREE-rich, olivine–mica-lamprophyres with affinities to lamproites, Mt. Bundey, Northern Territory, Australia. *Lithos* **28**, 303–325.

Steiger, R. H. & Jäger, E. (1977). Subcommission on geochronology: convention on the use of decay constants in geo- and cosmochronology. *Earth and Planetary Science Letters* **36**, 359–362.

Stein, M., Navon, O. & Kessel, R. (1997). Chromatographic metasomatism of the Arabian–Nubian lithosphere. *Earth and Planetary Science Letters* **152**, 75–91.

Stolper, E. & Newman, S. (1994). The role of water in the petrogenesis of Mariana trough magmas. *Earth and Planetary Science Letters* **121**, 293–325.

Sun, S.-S. (1980). Lead isotopic study of young volcanics from mid-ocean ridges, ocean islands and island arcs. *Philosophical Transactions of the Royal Society of London, Series A* **297**, 409–445.

Sun, S.-S. & McDonough, W. F. (1989). Chemical and isotopic systematics of ocean basalts: implications for mantle composition and processes. In: Saunders, A. D. & Norry, M. J. (eds) *Magmatism in the Ocean Basins. Geological Society, London, Special Publications* **42**, 313–345.

Tan, X. H. (1999). Characteristics and formation mechanism of Cenozoic structural basins in the three-river area of west Yunnan. *Yunnan Geology* **18**, 112–121 (in Chinese with English abstract).

Tan, X. H. & Zhu, Z. (1999). The movement features of Cenozoic Chenghai fault, Yunnan province. *Yunnan Geology* **2**, 21–24 (in Chinese with English abstract).

Tapponnier, P., Lacassin, R., Leloup, P. H., Scharer, U., Zhong, D. L., Wu, H. W., Liu, X. H., Ji, S. C., Zhang, L. S. & Zhong, J. Y. (1990). The Ailao Shan/Red River metamorphic belt: Tertiary left-lateral shear between Indochina and South China. *Nature* **343**, 431–437.

Tatsumi, Y. & Hanyu, T. (2003). Geochemical modeling of dehydration and partial melting of subducting lithosphere: towards a comprehensive understanding of high-Mg andesite formation in the Setouchi volcanic belt, SW Japan. *Geochemistry, Geophysics, Geosystems* **4**, 2003GC000530.

Tatsumi, Y., Hamilton, D. L. & Nesbitt, R. W. (1986). Chemical characteristics of fluid phase released from a subducted lithosphere and origin of arc magmas: evidence from high-pressure experiments and natural rocks. *Journal of Volcanology and Geothermal Research* **29**, 293–309.

Taylor, S. R. & McLennan, S. M. (1985). *The Continental Crust: its Composition and Evolution*. Oxford: Blackwell Scientific, pp. 1–99.

Taylor, R. N. & Nesbitt, R. W. (1998). Isotopic characteristics of subduction fluids in an intra-oceanic setting, Izu–Bonin arc, Japan. *Earth and Planetary Science Letters* **164**, 79–98.

Thompson, R. N., Morrison, M. A., Hendry, G. L. & Parry, S. J. (1984). An assessment of the relative roles of crust and mantle in

magma genesis: an elemental approach. *Philosophical Transactions of the Royal Society of London, Series A* **310**, 549–590.

Turner, S. & Hawkesworth, C. (1995). The nature of the sub-continental mantle: constraints from the major-element composition of continental flood basalts. *Chemical Geology* **120**, 295–314.

Turner, S., Hawkesworth, C., van Calsteren, P., Heath, E., Macdonald, R. & Black, S. (1996). U-series isotopes and destructive plate margin magma genesis in the Lesser Antilles. *Earth and Planetary Science Letters* **142**, 191–207.

Turner, S., Hawkesworth, C., Rogers, N., Bartlett, J., Worthington, T., Hergt, J., Pearce, J. & Smith, I. (1997). ^{238}U–^{230}Th disequilibrium, magma petrogenesis, and flux rates beneath the depleted Tonga–Kermadec island arc. *Geochimica et Cosmochimica Acta* **61**, 4855–4884.

Turner, S., Bourdon, B. & Gill, J. (2003). Insight into magma genesis at convergent margins from U-series isotopes. In: Bourdon, B., Henderson, G. M., Lundstrom, C. C. & Turner, S. P. (eds) *Uranium-Series Geochemistry. Reviews in Mineralogy and Geochemistry, Mineralogical Society of America* **52**, 255–310.

Turner, S. P. (2002). On the time-scales of magmatism at island-arc volcanoes. *Philosophical Transactions of the Royal Society of London, Mathematical, Physical and Engineering Sciences*, **360**, 2853–2871.

Venturelli, G., Capedri, S., Battistini, G. D., Crawford, A., Kogarko, L. N. & Celestini, S. (1984). The ultrapotassic rocks from southeastern Spain. *Lithos* **17**, 37–54.

Vroon, P. Z., Van Bergen, M. J., White, W. M. & Varekamp, J. C. (1993). Sr–Nd–Pb isotope systematics of the Banda Arc, Indonesia: combined subduction and assimilation of continental material. *Journal of Geophysical Research* **98**, 22349–22366.

Walker, J. A., Patino, L. C., Cameron, B. I. & Carr, M. J. (2000). Petrogenetic insights provided by compositional transects across the Central American arc: southeastern Guatamala and Honduras. *Journal of Geophysical Research* **105**(B8), 18949–18963.

Wang, E., Burchfiel, B. C., Royden, L. H., Chen, L. Z., Chen, J. S., Li, W. X. & Chen, Z. L. (1998). *Late Cenozoic Xianshuihe–Xiaojiang, Red River, and Dali Fault Systems of Southwestern Sichuan and Central Yunnan, China. Geological Society of America, Special Paper* **327**, 108 pp.

Wang, J.-H., Yin, A., Harrison, T. M., Grove, M., Zhang, Y.-Q. & Xie, G.-H. (2001). A tectonic model for Cenozoic igneous activities in the eastern Indo-Asian collision zone. *Earth and Planetary Science Letters* **188**, 123–133.

Wang, S., Hu, S., Zhang, R., Zhai, M. & Cong, B. (1987). A study on history of heat events of Dukou complex in the Mianning area, Sichuan province, SW China. In: Zhang, Y. & Liu, B. (eds) *Panxi Rift in China, Vol. 2*. Beijing: Geological Publishing House, pp. 61–65 (in Chinese with English abstract).

Wang, X. F., Metcalfe, I., Jian, P., He, L. Q. & Wang, C. S. (2000). The Jinshajiang–Ailaoshan Suture Zone, China: tectonostratigraphy, age and evolution. *Journal of Asian Earth Sciences* **18**, 675–690.

Williams, H. M., Turner, S. P., Pearce, J. A., Kelley, S. P. & Harris, N. B. W. (2004). Nature of the source region for post-collisional, potassic magmatism in southern and northern Tibet from geochemical variations and inverse trace element modelling. *Journal of Petrology* **45**, 555–607.

Wilson, M. (1989). *Igneous Petrogenesis: a Global Tectonic Approach*. London: Unwin Hyman, 466 pp.

Woodhead, J. D. & Johnson, R. W. (1993). Isotopic and trace-element profiles across the New Britain island arc, Papua New Guinea. *Contributions to Mineralogy and Petrology* **113**, 479–491.

Wu, G. Y. & Cong, B. L. (1988). Precambrian basement of the Panxi region. In: Cong, B. L. (ed.) *Formation and Evolution of the Panxi Paleorift*. Beijing: Science Press, pp. 1–30 (in Chinese with English abstract).

Wu, G. Y. & Zhang, W. (1990). A preliminary study of petrochemistry of Kangding granitic complexes. *Mineralogy and Petrology* **10**, 23–30 (in Chinese with English abstract).

Wu, H. (1993). Discovery of Early Carboniferous deep-sea sediments from Jinsha Belt, NW Yunnan. *Scientia Geologica Sinica* **28**, 395–397 (in English).

Xie, Y. W. & Zhang, Y. Q. (1995). Petrochemistry of the Cenozoic magmatic rocks in the eastern Erhai, Yunnan Province. *Acta Petrologica Sinica* **11**, 423–433 (in Chinese with English abstract).

Xie, Y. W., Zhang, Y. Q., Chung, S.-L. & Li, X. H. (1999). Trace element characteristics of the Cenozoic high-K-alkaline magmatic rock series in the eastern Erhai, Yunnan Province. *Acta Petrologica Sinica* **15**, 75–82 (in Chinese with English abstract).

Xu, D., Chen, Y., Zhang, Y., Li, W., Zhao, B. & Luo, T. (1995). The study of the age and origin of the Kangding granitic complex, western Yangtze craton, China. *Geological Review* **41**, 101–111 (in Chinese with English abstract).

Xu, Y., Chung, S.-L., Jahn, B. M. & Wu, G. (2001*a*). Petrological and geochemical constraints on the petrogenesis of Permian–Triassic Emeishan flood basalts in southwestern China. *Lithos* **58**, 145–168.

Xu, Y., Menzies, M. A., Thirlwall, M. F. & Xie, G. (2001*b*). Exotic lithosphere mantle beneath the western Yangtze Craton; petrogenetic links to Tibet using highly magnesian ultrapotassic rocks. *Geology* **29**, 863–866.

Yang, K. H. (1998). A plate reconstruction of the eastern Tethyan orogen in southwestern China. In: Flower, M. F. J., Chung, S.-L., Lo, C.-H. & Lee, T.-Y. (eds) *Mantle Dynamics and Plate Interactions in East Asia. Geodynamics Series, American Geophysical Union* **27**, 269–287.

YBGMR (Yunnan Bureau of Geology and Mineral Resources). (1990). *Regional Geology of Yunnan Province*. Beijing: Geological Publishing House, 728 pp. (in Chinese with English abstract).

Zhai, M. G. & Yang, R. Y. (1986). Early Precambrian gneiss basement in the Panxi area, southwest China. *Acta Petrologica Sinica* **2**, 22–37 (in Chinese with English abstract).

Zhang, H. F., Sun, M., Zhou, X. H., Fan, W. M., Zhai, M. G. & Yin, J. F. (2002). Mesozoic lithosphere destruction beneath the North China Craton: evidence from major-, trace-element and Sr–Nd–Pb isotope studies of Fangcheng basalts. *Contributions to Mineralogy and Petrology* **144**, 241–253.

Zhang, L.-S. & Scharer, U. (1999). Age and origin of magmatism along the Cenozoic Red River shear belt, China. *Contributions to Mineralogy and Petrology* **134**, 67–85.

Zhang, L. S. & Zhong, D. L. (1996). The Red River strike-slip shear zone and Cenozoic tectonics of east Asia continent. *Scientia Geologica Sinica* **31**, 327–341 (in Chinese with English abstract).

Zhang, Y. Q. & Xie, Y. W. (1997). Geochronology of alkali-rich intrusions and Nd, Sr isotopic characteristics in Ailiao Shan–Jinsha River. *Sciences in China (Series D)* **27**, 289–293 (in Chinese with English abstract).

Zhang, Y. Q., Xie, Y. W., Li, X. H., Qiu, H. N., Zhao, Z. H., Liang, H. Y. & Chung, S. L. (2000). The isotopic characteristics of shoshonitic associations in western Tibet: petrogenesis and tectonic significance. *Sciences in China (Series D)* **30**, 493–498 (in Chinese with English abstract).

Zhong, D. L. (1998). *Paleotethyan Orogenic Belts in Yunnan and Western Sichuan*. Beijing: Science Press, 231 pp. (in Chinese with English abstract).

Zhong, D. L., Ding, L., Liu, F. T., Liu, J. H., Zhang, J. J., Ji, J. Q. & Chen, H. (2000). The multi-direction layer and frame structure of rock layers in orogenic belt and its control on Cenozoic magmatic activities—an example from Sanjiang and its neighboring area. *Sciences in China (Series D)* **30**, 1–8 (in Chinese with English abstract).

Zhu, B. Q., Zhang, Y. Q. & Xie, Y. W. (1992). Nd, Sr and Pb isotopic characteristics of Cenozoic ultra-potassic volcanic rocks from eastern

Erhai, Yunnan and their implications for subcontinental-mantle evolution in southwestern China. *Geochimica* **3**, 201–212 (in Chinese with English abstract).

Zindler, A. & Hart, S. R. (1986). Chemical geodynamics. *Annual Review of Earth and Planetary Sciences* **14**, 493–571.

Zou, H. B., Zindler, A., Xu, X. S. & Qi, Q. (2000). Major, trace element, and Nd, Sr and Pb isotope studies of Cenozoic basalts in SE China: mantle sources, regional variations and tectonic significance. *Chemical Geology* **171**, 33–47.

APPENDIX A: COMPARISON OF MAJOR AND TRACE ELEMENT ANALYSES BETWEEN BELGIUM AND CHINA

Sample no.:	CH9722 Belgium	CH9722 China	CH9723 Belgium	CH9723 China	CH7F007 Belgium	CH7F007 China	CH9716 Belgium	CH9716 China	CH9786 Belgium
SiO_2	49·8	48·92	45·72	45·28	59·39	59·91	42·69	42·86	52·93
TiO_2	1·51	1·48	2·15	2·11	1·58	1·59	1·47	1·46	0·9
Al_2O_3	12·85	13·22	9·5	10·08	10·57	10·38	9·88	10·01	13·08
Fe_2O_3	8·84	9·16	9·34	9·74	5·85	5·77	11·36	11·62	7·95
MnO	0·11	0·11	0·17	0·17	0·12	0·1	0·18	0·18	0·13
MgO	9·03	8·97	14·21	13·92	7·2	7·24	14·12	14·13	7·33
CaO	11·62	11·55	13·1	12·96	5·72	5·77	14·94	14·69	10·17
Na_2O	1·44	1·64	0·9	0·84	1·78	1·81	1·45	1·29	2·66
K_2O	3·56	3·66	3·76	3·77	6·92	6·44	2·68	2·64	4·36
P_2O_5	1·24	1·22	1·15	1·13	0·87	0·99	1·23	1·12	0·49
Rb	2189	206	528	244	288	301	66·2	187	152
Ba	4645	4608	6143	6025	6213	6174	4482	4512	1267
Sr	2701	2675	3283	3197	1909	1956	3705	3074	1026
Y	83·1	85·0	75·6	77·7	37·6	39·1	48·0	48·2	22·3
Zr	426	416	905	931	1558	1520	464	478	145
Nb	18·7	18·5	39·8	40·2	36·7	36·5	24·2	24·4	5·25
Pb	41·2	42·2	39·2	41·4	90·7	91·6	45·4	45·4	31·9
Th	25·5	26·6	26·7	27·6	30·4	30·8	32·4	31·5	8·45
Sc	16·9	16·7	19·7	20·4	15·2	15·3	24·1	24·1	16·1
Cr	379	367	593	584	277	268	708	692	388
Co	37·0	36·5	46·5	46·2	26·5	27·2	50·5	51·4	31·4
La	148·6	143·6	189·9	186·5	160·7	155·1	191·8	196·5	27
Ce	307·7	304·3	421·4	423·8	330·6	320·5	405·4	410·6	56·5
Nd	131·3	129·5	206·5	200·2	136·9	135·9	175·1	178·6	28·1
Sm	21·2	21·3	38·5	38·2	22·2	22·1	29·1	29·2	5·96
Eu	5·24	5·26	10·15	10·21	5·87	5·88	7·37	7·19	1·61
Tb	1·65	1·63	3·68	3·65	1·68	1·64	2·65	2·66	0·74
Yb	1·94	1·95	3·11	3·14	2·15	2·09	3·26	3·27	1·76
Lu	0·27	0·26	0·41	0·44	0·25	0·26	0·44	0·44	0·29
Hf	10·2	10·2	22·1	21·9	35·6	35·9	10·8	11·9	3·65
Ta	1·22	1·23	1·95	1·94	2·01	2	1·13	1·1	0·44
U	4·21	4·41	5·68	5·77	8·79	8·97	6·72	6·78	3·15

Sample no.:	CH9786 China	CH7F002 Belgium	CH7F002 China	CH9854 Belgium	CH9854 China	CH9783 Belgium	CH9783 China	CH9803 Belgium	CH9803 China
SiO_2	52·67	46·34	45·87	53·65	53·92	56·35	56·69	56·33	56·61
TiO_2	0·89	1·29	1·24	0·76	0·77	0·9	0·92	0·7	0·71
Al_2O_3	13·04	13·88	14·03	13·22	12·71	12·01	11·91	12·64	12·37
Fe_2O_3	8·1	11·09	11·12	7·79	7·75	7·99	8·08	7·71	7·42
MnO	0·12	0·14	0·14	0·12	0·12	0·11	0·1	0·1	0·09
MgO	7·3	11·34	11·61	8·16	8·21	6·54	6·59	7·53	7·54
CaO	10·11	10·25	10·37	9·81	9·91	7·22	6·94	6·22	6·54

APPENDIX: CONTINUED

Sample no.:	CH9786 China	CH7F002 Belgium	CH7F002 China	CH9854 Belgium	CH9854 China	CH9783 Belgium	CH9783 China	CH9803 Belgium	CH9803 China
Na_2O	2·67	1·52	1·53	2·54	2·59	2·09	2·1	2·6	2·56
K_2O	4·64	2·77	2·72	3·55	3·54	6·37	6·24	4·89	4·94
P_2O_5	0·46	1·38	1·37	0·4	0·48	0·42	0·43	1·28	1·22
Rb	152	48·2	187	194	196	264	272	172	176
Ba	1302	3429	1830	1565	1495	2117	2047	2512	2537
Sr	1017	1034	1038	1325	1330	1374	1367	1536	1544
Y	22·2	29·4	30·8	24·8	25·0	27·2	27·5	28·0	28·9
Zr	149	172	174	139	142	183	188	195	200
Nb	5·13	8·55	8·57	5·00	5·14	8·25	8·19	7·2	7·22
Pb	32·1	30·6	31·1	39·2	41·6	43·6	45·3	74·0	76·1
Th	8·15	5·35	5·34	9·95	10·2	13·2	13·3	14·4	14·3
Sc	16·1	29·5	30·1	22·5	22·6	17·6	18·0	16·2	16·3
Cr	389	594	604	414	403	291	300	574	584
Co	32·1	45·3	45·7	26·5	26·4	23·2	23·2	39·2	38·7
La	26·8	32·1	32·7	32·4	32·5	38·8	39·0	47·3	47·5
Ce	56·4	64·6	65·0	68·8	68·2	80·9	79·1	95·2	92·2
Nd	28·6	31·7	32·1	32·1	32·7	39·3	40·2	43·5	44·3
Sm	6·07	7·07	7·31	6·77	6·97	8·2	8·28	8·99	9·13
Eu	1·67	1·95	1·98	1·78	1·75	2·07	2·04	2·33	2·31
Tb	0·77	0·9	0·94	0·79	0·81	0·91	0·94	0·96	0·97
Yb	1·75	2·53	2·54	1·86	1·88	1·91	1·92	1·91	1·94
Lu	0·27	0·38	0·39	0·26	0·25	0·32	0·33	0·28	0·29
Hf	3·66	4·72	4·75	3·48	3·51	4·69	4·71	4·86	4·88
Ta	0·45	0·46	0·46	0·44	0·45	0·67	0·66	0·56	0·57
U	3·21	1·34	1·38	2·57	2·6	3·51	3·53	3·02	3·06

Major element data are normalized to 100% on a volatile-free basis. For data from Belgium, major elements (Si, Ti, Al, Fe, Mg, Ca and P) were determined by atomic absorption spectrometry (AAS), whereas Na, K and Mn were determined by atomic emission spectrometry (AES). The analytical precisions of both AAS and AES were $\leq$2%. Trace elements Rb, Sr, Nb, Y, Pb and Zr were analysed on pressed-powder discs by X-ray fluorescence (XRF) spectroscopy using a Kevex 0700 system. Other trace element concentrations (Sc, Cr, Co, Ba, REE, Hf, Ta, Th and U) were determined by instrumental neutron activation analysis (INAA). The analytical precisions of the XRF and INAA data are $\leq$5% (also see text). Analytical procedures follow those of Hertogen *et al*. (1985) and Mulder *et al*. (1986). For data from China, whole-rock major element oxides were analysed with a Phillips PW1400 sequential X-ray fluorescence spectrometer. Fused glass discs were used and the analytical precision was better than 2% relative. Trace element contents were analysed by inductively coupled plasma mass spectrometry (ICP-MS). The discrepancy, based on repeated analyses of samples and standards, is $\leq$5%. The detailed analytical procedures follow those of Jin & Zhu (2000) and Zhang *et al*. (2002). The Rb concentrations of samples CH9716, CH9722, CH9723 and CH7F002 and the Ba content of sample CH7F002 are outside analytical error. It is possible that the rocks that were sent to Belgium from Beijing (China) for analysis were too small, leading to unrepresentative analyses of Rb and Ba.

APPENDIX B: TRACE ELEMENT DATA MODELLING

Table B1: Modal proportions of minerals in the source and partition coefficients used in modelling

Mineral	Modal (%)	Ba	Nb	La	Yb
Apatite	0·5	0·05	0·1	3·7	8·1
Clinopyroxene	8	0·0006	0·0027	0·031	0·265
Olivine	60	0·00000545	0·00405	0·0004	0·2685
Orthopyroxene	25	0·0000062	0·003	0·00045	0·097
Phlogopite	2	3·48	0·0853	0·0322	0·0484
Rutile	0·5	0·0137	136	0·0055	0·0093
Spinel	2	—	0·085	0·01	0·01
Titanite	2	0·6	4·6	—	104
*D**		0·08	0·78	0·02	2·33

*Bulk partition coefficient.
—, no data are available.
Data source: GERM (Geochemical Earth Reference Model) home page, http://www.earthref.org/.

Some comments on the selection of partition coefficients

(1) All partition coefficients were determined by microbeam techniques for phenocryst and matrix in equilibrium, except for those of La (olivine) and Yb (spinel), which were determined by calculation.

(2) The composition of the magmatic rocks from which the coexisting phenocryst–matrix partition coefficients were determined is similar to lamprophyres, potassic rocks and alkali-basalts.

(3) The selected values of partition coefficients were most consistent with (or close to) mantle wedge melting conditions (Pearce & Parkinson, 1993), i.e. temperatures of 1200–1300°C, pressures of 1–30 kbar, and oxygen fugacities of QFM ± 1 (where QFM is the quartz–fayalite–magnetite buffer).

Composition of the subduction-derived fluid

Determination of a realistic composition for the subduction-derived fluid is not easy because of a lack of data for crystal–fluid partition coefficients and the complexity of the composition of the fluid (Munker, 2000). At present, available data for subduction-related fluid compositions come mainly from experimental studies (e.g. Stolper & Newman, 1994; Keppler, 1996). Because the estimated concentrations of Ba, La, Nb and Yb in subduction-derived fluids vary significantly (Stolper & Newman, 1994; Stein *et al.*, 1997; Bizimis *et al.*, 2000; Tatsumi & Hanyu, 2003), we select fluid (A) and fluid (B) to represent a subduction-derived fluid with higher contents of Ba, La, Nb and Yb and a fluid having lower contents of those elements, respectively. The concentrations of Ba, La, Nb and Yb in fluid (A) and fluid (B) are shown in Table 7.

Composition of the MORB-source mantle

The composition of the mantle wedge, prior to the addition of fluid, beneath the western part of the Yangtze craton is similar to Indian MORB-source mantle based on trace element and Sr–Nd–Pb isotope compositions (Figs 8 and 9). However, the concentrations of Ba (4·9–12·4 ppm), La (1·9–4·1 ppm), and Yb (2·3–3·4 ppm) in Indian MORB are variable (Rehkämper & Hofmann, 1997). We therefore used 0·1 times the average trace element concentrations in N-MORB (Sun & McDonough, 1989) to represent the mantle source composition (Ba 0·63 ppm, La 0·25 ppm, Nb 0·23 ppm and Yb 0·31 ppm) on the basis of an assumption that MORB is a consequence of ~10% partial melting of the mantle source (Wilson, 1989).

Modal proportion of mineral phases in the mantle source region

The model assumes that the WSYP magmas were generated by a two-stage process: (1) mixing of a depleted mantle component (similar to the MORB source) and a subduction-derived fluid; (2) partial melting of the resultant enriched mantle and the generation of the WSYP melts. Following Wilson (1989), a modal mineral composition, which is composed of olivine (60%), orthopyroxene (25%), clinopyroxene (8%) and spinel (2%), was used because the mantle source region beneath the western part of the craton is in the spinel stability field. The remaining part of the mineral assemblage resulted from metasomatism of the mantle wedge by the subduction-derived fluid. This is made up of phlogopite (2%), titanite (2%), rutile (0·5%) and apatite

(0·5%) on the basis of our interpretations of the primitive mantle-normalized trace element characteristics of the most primitive mafic magmas and variation trends of trace element ratios (Figs 6 and 17; for detailed description also see text).

Mantle partial melting model

For the case of modal batch partial melting, the modelling was carried out using the equation (Wilson, 1989)

$$C_L/C_o = 1/(F + D - FD). \quad (A1)$$

For non-modal batch partial melting, the following equation was used (Wilson, 1989):

$$C_L/C_o = 1/(F + D - FP). \quad (A2)$$

In (1) and (2) C_L is the concentration of a trace element in the melt, and C_o is the content of a trace element in the metasomatized mantle source, which is modelled as a mixture of a depleted mantle component (m, similar to MORB source) and a subduction-derived fluid (f):

$$C_o = X_f C_f + (1 - X_f) C_m. \quad (A3)$$

X_f is the proportion of the subduction-derived fluid in the mantle source, C_f is the concentration of a trace element in the subduction-derived fluid, C_m is the concentration of a trace element in the depleted mantle source, D is the bulk distribution coefficient. $D = \Sigma X_i D_i$, where X_i is the weight fraction of phase i in the mineral assemblage and D_i is its crystal–liquid partition coefficient. $P = \Sigma P_i \times D_i$, where P_i is the proportion of phase i entering the melt. On the basis of the interpretation of the relative proportions of the mineral phases entering the melt during non-modal batch partial melting (see main text), we assumed $P = 0{\cdot}01D_{Apatite} + 0{\cdot}25D_{Clinopyroxene} + 0{\cdot}3D_{Olivine} + 0{\cdot}2D_{Orthopyroxene} + 0{\cdot}08D_{Phlogopite} + 0{\cdot}005D_{Rutile} + 0{\cdot}055D_{Spinel} + 0{\cdot}1D_{Titanite}$. F is the degree of partial melting.